# Toward an experiment of matter-wave interferometry based on strontium

Paul Robert

THÈSE PRÉSENTÉE

POUR OBTENIR LE GRADE DE

# DOCTEUR
# DE L'UNIVERSITÉ DE BORDEAUX

ECOLE DOCTORALE SCIENCES PHYSIQUES ET DE L'INGÉNIEUR

LASERS, MATIÈRE ET NANOSCIENCES

Par **Paul ROBERT**

## Mise en place d'une expérience d'interférométrie atomique basée sur le strontium.

Sous la direction de : **Andrea BERTOLDI**

4 October, 2023

Membres du jury :

| | | |
|---|---|---|
| M. Nicola POLI | University of Florence | Rapporteur |
| M. Denis BOIRON | Université Paris-Saclay | Rapporteur |
| M. Brahim LOUNIS | Université de Bordeaux | Président |
| M. Naceur GAALOUL | Leibniz University of Hannover | Examinateur |
| M. Andrea BERTOLDI | Université de Bordeaux | Directeur |

Membre invité :

| | | |
|---|---|---|
| M. Franck CORREIA | Direction Générale de l'Armement | Invité |

# Acknowledgement

J'estime le diplôme de docteur comme l'un des plus beaux au monde. C'est pourquoi je remercie Andrea Bertoldi et Philippe Bouyer pour l'opportunité qu'ils m'ont donnée de devenir docteur. De même, je remercie le jury de thèse : Nicola Poli et Denis Boiron, qui ont accepté de me faire l'honneur d'être mes rapporteurs de thèse, ainsi que Brahim Lounis et Naceur Gaaloul, qui ont accepté d'être examinateurs et avec qui j'ai eu des échanges passionnants durant ma thèse.

J'ai eu la chance de ne pas vivre ma thèse seul, grâce à Chen-Hao Feng, qui non seulement m'a aidé à approfondir mon sujet de thèse, mais m'a aussi soutenu dans les moments difficiles, même après son départ. Tout comme j'ai été soutenu par les différents membres de l'équipe d'atomes froids du LP2N : merci à Luisa pour le temps qu'elle a passé à écouter mes problèmes et à jouer de la musique avec moi, à Clément, Vincent, Baptiste, Jean-Baptiste, Cyrille et Geovan pour leur compagnie. Merci beaucoup à Quentin et Célia, qui vont finir leur thèse en même temps que moi. J'ai une pensée toute particulière pour le temps passé ensemble en conférence. Merci à la communauté de FOMO, qui s'est révélée pleine de personnes intéressantes et inspirantes. Un immense merci à Dylan Sabulsky, qui a dépensé du temps et du café sans compter pour faire de moi un chercheur accompli.

Je remercie aussi Benjamin Canuel pour ses conseils précieux afin d'améliorer ma soutenance de thèse. Merci aussi à Simon Bernon, qui a été pour moi non seulement un professeur d'exception, mais qui m'a aussi donné la chance d'enseigner aux étudiants de master et qui m'a accompagné dans cette expérience. À ce titre, je remercie aussi Nicolas Dubreuil, Jean Augereau et Bertrand Simon pour nos discussions, autant sur la physique que sur l'enseignement et sur le métier de chercheur. Un grand merci aussi à Philippe Lalanne, qui m'a fait suffisamment confiance pour me confier plus de responsabilités que ce que j'espérais. Je remercie aussi l'administration du LP2N, l'atelier mécanique et électrique qui ont été là pour moi quand j'en avais besoin.

Si je voulais profondément faire une thèse en arrivant au LP2N, ça n'a pas toujours été une évidence. Un profond merci à mes professeurs de prépa et à Damien Bigourd, qui ont travaillé avec moi et sans qui je ne serais certainement jamais arrivé jusqu'ici. Enfin, je remercie mes amis d'enfance : Corentin, Florent et Raphaël, qui m'ont soutenu depuis le Viêt Nam et que je m'empresse de rejoindre après la soutenance.

# Contents

# Introduction

"*Research is to see what everybody else has seen, and to think what nobody else has thought.*"

Albert Szent-Györgyi

From the ancient philosophical debates about the indivisibility of matter to the contemporary marvels of quantum mechanics, the atom has remained a cornerstone of scientific inquiry. While the existence of atoms was conclusively established during Einstein's "annus mirabilis" of 1905 [1], it was not until the discovery of the laser in 1960 [2] and its subsequent advancements that the manipulation of atoms appeared as a viable experimental technique.

The emergence of laser cooling techniques during the late 1980s [3] marked a significant turning point that paved the path for atom optics. Building upon these groundbreaking methods, the year 1991 witnessed the inception of a new and swiftly advancing realm of study: atom interferometry [4, 5, 6].

The utilization of matter waves in place of electromagnetic waves has introduced the prospect of designing interferometers with sensitivity to novel forms of interaction. Over the past three decades, atom interferometry has demonstrated remarkable success in conducting measurements across diverse domains with precision comparable to or surpassing traditional devices.

The development of cold atom physics extends beyond the advancement of atomic interferometers, encompassing the creation of various systems. Notably, the realization of atomic boson condensation into Bose-Einstein Condensates (BEC) [7, 8], as well as the development of atomic optical clocks [9].

The significance of the number of atoms involved in these experiments cannot be over-

stated, as it exerts a profound influence on the sensitivity, precision, and reliability of the observations conducted. A higher atom number not only enhances the signal strength, rendering it more amenable to detection and analysis, but also affords researchers the advantage of statistical averaging, thereby mitigating the effects of stochastic fluctuations and elevating the overall measurement accuracy. Furthermore, in the context of atomic interferometry, an increased atom number plays a pivotal role in yielding distinct and well-defined interference patterns.

Cold atom experiments have also embraced the pursuit of compactness. The advantages of reduced size extend beyond lowering power consumption, enhancing energy efficiency and sustainability. Compact apparatus holds the additional benefit of enabling the creation of portable and field-deployable systems, thereby extending the domain of cold atom research beyond conventional laboratory confines. This newfound portability opens up avenues for experimentation in diverse environments, including space-based platforms and remote field studies, thus broadening the scope of scientific exploration.

As a demonstrator for gravitational wave (GW) detection, the Matter-Wave Laser Interferometric Gravitational Antenna (MIGA) experiment stands out [10]. It employs an ensemble of atomic interferometers, optically interconnected within a long optical cavity. Each individual atom interferometer utilizes $^{87}$Rb atoms through a two-photon process, requiring the implementation of two orthogonal baselines to effectively mitigate technical noise originating from laser systems. This PhD project is a part of a prototype initiative established at the LP2N laboratory (Laboratoire Photonique, Numérique et Nanosciences, Talence, France) that aims at employing $^{88}$Sr atoms in the pursuit of an enhanced iteration of MIGA featuring a single baseline.

# Thesis organization

The thesis is divided in three axes.

A presentation of the principle of atomic interferometry is provided in **Chapter 1**, along with an exploration of why alkaline-earth-like atoms are intriguing candidates for future experiments. The specific case of strontium, encompassing its history, inherent properties, and cooling techniques, is detailed in **Chapter 2**.

The experimental section of the thesis commences in **Chapter 3**, where the apparatus, laser systems, and electronic setups utilized in the project are outlined. A description of the novel Zeeman Slower, a pivotal component of this thesis, is presented in **Chapter 4**.

An outlook on an atomic interferometer employing $^{88}$Sr within an optical cavity is expounded upon in **Chapter 5**.

# Chapter 1

# Atomic Single-Photon Interferometry

Cold atoms serve as the foundational components for a diverse array of modern experiments. This journey was initiated by the pioneering work of Lebedev, Nichols, and Hull in 1901, who demonstrated the radiation pressure exerted by light on atoms, and by Frisch in 1933, who observed the deviation of individual sodium particles influenced by a sodium lamp [11, 12]. Subsequently, advancements in laser technology ushered in a new era of atomic cloud manipulation. Noteworthy milestones include the development of the first Zeeman Slower in 1982 by Phillips [13], and the creation of a magneto-optical trap by Chu in 1985 [14]. These innovations paved the way for the manipulation of cold atomic clouds, leading to the ability to observe atomic interferences.

Section 1.1 elucidates the fundamental principle of atomic interferometry, accompanied by an exploration of its historical context. In Section 1.2, a selection of applications harnessed through this technique is delineated. Venturing further into the intricacies, Section 1.3 delves into the specifics of two-photon interferometry, along with an exposition of a method tailored for gravitational wave observation employing this approach. The merits of single photon interferometry and the choice of an appropriate atomic candidate for such experiments are expounded upon in Section 1.4.

## Contents



Over the past three decades, a remarkable array of techniques has emerged for observing atomic interferences, involving various types of atoms in diverse scenarios. These methodologies form the foundation of sensors specifically designed for gravity measurements, encompassing tasks ranging from mapping geophysical phenomena to exploring the intricate interplay between relativity and quantum gravity.

## 1.1 Fundamental principle of atomic interferometry

Interferometry relies on the principle of phase coherence, which underlies all of its various implementations. When a wave is split into two or more paths, each path acquires a phase shift due to interactions with its environment. The resulting phase shifts can be measured by interfering the paths and observing the interference pattern. The precision of this measurement is fundamentally limited by the coherence time, and therefore coherence length, of the wave.

Atomic interferometry is a specific type of interferometry that leverages the wave-like properties of atoms, referred to as matter-waves, to generate the interference pattern. In this context, the coherence time is determined by the degree of isolation of the wave function from external perturbations. In contrast to optical interferometry, where matter such as beam splitters or mirrors is used to manipulate light, atom interferometry employs light to manipulate atomic wave functions.

### 1.1.1 Theoretical foundations of atomic interferometry

Consider a two-level quantum system with $|g\rangle$ as the ground state and $|e\rangle$ as the excited state. The wave packet of the system is manipulated using $\pi$ and $\frac{\pi}{2}$ pulses [15], which correspond respectively to half and a quarter of a Rabi cycle. When the system is subjected to a $\pi$ pulse, an atom in the ground state is promoted to the excited state, and vice versa.

$$|f;n\rangle \rightarrow |e;n-1\rangle \text{ and } |e;n\rangle \rightarrow |f;n+1\rangle \tag{1.1}$$

Similarly, a $\frac{\pi}{2}$ pulse splits the wave packet in two distinct components: one remaining undisturbed and one interacting with the interrogating photon

$$|f;n\rangle \rightarrow \frac{1}{\sqrt{2}}(|f;n\rangle + |e;n-1\rangle) \text{ and } |e;n\rangle \rightarrow \frac{1}{\sqrt{2}}(|e;n\rangle + |f;n+1\rangle) \tag{1.2}$$

Due to the significant difference between the number of atoms interacting with the laser field compared to the number of photons in this same field, it is assumed that the laser field is undisturbed.

Implemented in a Mach-Zehnder [16] interferometer, the wave packet undergoes a $\frac{\pi}{2}$

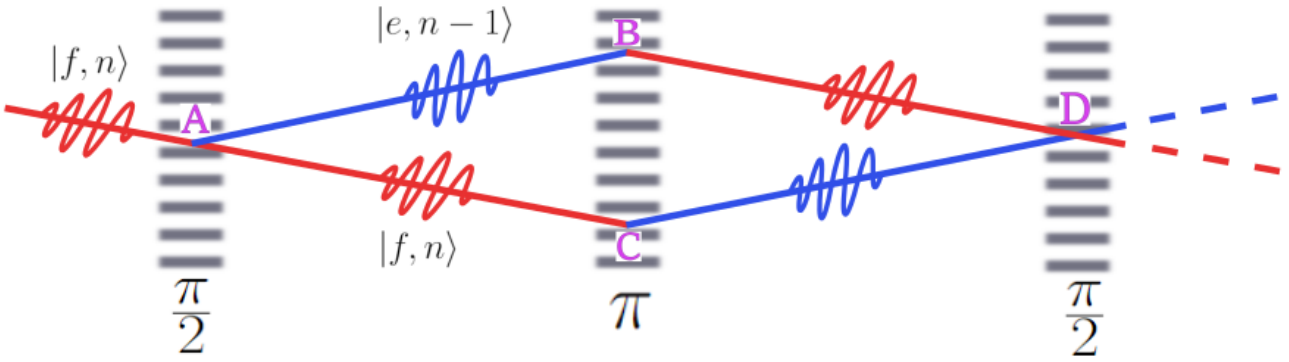


Figure 1.1: Mach-Zehnder atomic interferometer involving a wave packet undergoing the $\frac{\pi}{2}$, $\pi$ and $\frac{\pi}{2}$ sequence. The fundamental (excited) state and its trajectory are denoted in red (blue).

pulse to split the wave packet, then a $\pi$ pulse that redirect the two atomic paths such that they can overlap and finally a last $\frac{\pi}{2}$ pulse to combine the trajectories and obtain the interference signal.

The two paths A $\rightarrow$ B $\rightarrow$ D and A $\rightarrow$ C $\rightarrow$ D are interfering after the second $\frac{\pi}{2}$ pulse and the phase difference between those two wave functions is determined by observing the population distribution via fluorescence measurements.

For a gravity sensor, the phase difference is given by $\Delta\Phi = -k_{\text{eff}} g (2T)^2$, where $k_{\text{eff}}$ is the effective wave vector difference between the two paths, $g$ the acceleration due to gravity, and $T$ the time interval between the two $\frac{\pi}{2}$ pulses [17]. Similarly, for a rotation sensor, the phase difference is given by $\Delta\Phi = 2\Omega k_{\text{eff}} v T^2$, where $\Omega$ is the rotation rate and $v$ the atomic velocity [18].

### 1.1.2 History and evolution in the matter wave community

The concept of using atoms to probe fundamental physics was initially proposed by Einstein in his theory of general relativity, which predicts that gravity affects the motion of atoms. However, the theoretical foundation of atom interferometry can be traced back to the wave-particle duality of matter, first proposed by Louis de Broglie in 1924. According to de Broglie, every particle exhibits both wave-like and particle-like properties, and the wavelength associated with a particle is

Figure 1.2: Louis Victor de Broglie, 1929.

$$\lambda_{\text{dB}} = \frac{h}{p} \tag{1.3}$$

which is now called the de Broglie wavelength. Here, $h$ is the Planck constant and $p$ the momentum of the particle. The first experimental verification of the wave-particle duality was achieved in 1927 by Clinton Davisson and Lester Germer, who demonstrated that electrons exhibit interference patterns that are characteristic of waves [19].

The first observation of wave packet splitting from an atom was reported in 1930 [20]. However, the development of atom interferometry as an experimental technique took off in the 1960s with the emergence of laser technology. It was not until 1991 that Mark Kasevich and Steven Chu demonstrated the first atomic interferometer using laser-cooled sodium atoms interacting via Raman transition [4].

Since then, atom interferometry has undergone a rapid evolution thanks to advances in laser technology and the use of ultra-cold atoms prepared in magneto-optical traps (MOT). Slowed down to a few nK, these atoms can be manipulated with high precision enabling the construction of highly sensitive gravimeters and accelerometers, used for applications in geophysics, navigation, and inertial sensing [18, 21].

These developments have enabled researchers to perform a wide range of precision measurements in fundamental physics, including tests of general relativity, the measurement of fundamental constants, and the detection of gravitational waves.

## 1.2 Application of atomic interferometry in fundamental research

### 1.2.1 Atomic interferometry applied for constant measurement

Considering the high sensitivity of atomic interferometry to gravitational fields compare to optical interferometry and its potentially long coherence time, this technique allows for fine measurement of fundamental constants.

**Measurement of the universal gravitational constant**

The universal gravitational constant, denoted by the symbol G and introduced by Sir Isaac Newton, is a fundamental constant of nature that appears in the mathematical formula describing the gravitational force between two masses. The value of G was first measured by Henry Cavendish in 1798, using a torsion balance experiment [22].

In many atomic interferometry experiments, two clouds of ultra-cold Cs [23] or Rb [24] atoms are typically prepared and either launched upwards or dropped in free fall. Each atomic cloud is divided into two paths, and after a controlled time of flight, they are recombined with a phase mismatch, leading to an interference pattern that reflects the acceleration experienced by each cloud. This readout enables the measurement of the difference in gravitational acceleration between the two clouds. This difference in acceleration is known as the gravity gradient and the device as a gravity-gradiometer. It can be used to measure a variety of physical quantities, including the local gravity field, the curvature of spacetime, and especially the gravitational constant G.

Currently, the CODATA value for the fundamental gravity constant stands at $6.67430 \times 10^{-11} \mathrm{m^3 kg^{-1} s^{-2}}$, carrying a relative uncertainty of $2.2 \times 10^{-5}$ [25, 26]. The most precise measurement achieved using an atomic interferometer gives a value of $6.67191 \times 10^{-11} \mathrm{m^3 kg^{-1} s^{-2}}$, with a relative uncertainty of $1.50 \times 10^{-4}$ [27]. Despite the exceptional precision achieved in these measurements, there still exists a notable discrepancy between the values obtained by different experiments, primarily due to the feebleness of the gravitational interaction and the inherent difficulty in fully shielding it from other influences.

**Measurement of the fine structure constant**

The fine structure constant $\alpha$ is a dimensionless physical constant that characterizes the strength of the electromagnetic interaction between light and charged particles. Its precise determination allows for a test of the Standard Model (SM) and may constraints the possible candidates for dark matter. It is defined as

$$\alpha = \frac{e^2}{4\pi\epsilon_0\hbar c}$$

where $\epsilon_0$ is the vacuum permittivity, $e$ is the elementary charge, $\hbar$ is the reduced Planck constant, and $c$ is the speed of light in vacuum. Its value is approximately $\frac{1}{137}$.

While the most accurate measurement of the fine structure constant involves quantum Hall effect in the framework of quantum electrodynamics (QED), in 2020, the team lead by Pierre Cladé and Saïda Guellati-Khélifa from the LKB measured it with an accuracy of 81 parts per trillion using atomic interferometry. [28]. In this experiment, Bloch oscillations are used to coherently transfer photons to the Rb atoms and the recoil velocity created by this interaction is measured using an atomic interferometer. Measuring the recoil velocity gives the ratio $\frac{\hbar}{m}$, which is proportional to $\alpha^2$.

### 1.2.2 Atomic interferometry in space

Atomic interferometry has significantly advanced precision measurements in fundamental physics and metrology. Nevertheless, interferometers based on Earth encounter challenges arising from Newtonian noise and seismic noise, necessitating the exploration of space-based alternatives. Space-based interferometers also offer the advantage of extended interrogation times, enabling free fall of both the laboratory and atomic clouds [29].

Several space-based atomic interferometry experiments have been proposed, for example by the European Space Agency (ESA) as part of the Atomic Clock Ensemble in Space (ACES) mission [30], the Cold Atom Laboratory (CAL) on board of the International Space Station (ISS) [31] or the CARIOQA project [32].

Space-based experiments have demonstrated their capacity for fundamental research, even in recent times. The 14th September of 2022, the MICROSCOPE mission [33] published its final result about the weak equivalence principal (WEP) measurement with unprecedented

accuracy. Theorized by Einstein in 1907, the WEP states that all objects in free fall undergo the same acceleration, independent of their composition or structure. MICROSCOPE used different test masses composed of titanium and platinum alloys probed with ultrasensitive differential electrostatic accelerometers. Any difference in the acceleration between the test masses would be a violation of the WEP; the MICROSCOPE mission measured no discrepancy with an accuracy of $\eta = 10^{-15}$ in terms of the Eötvös ratio.

### 1.2.3 Dark Matter

The term "dark matter" (DM) refers to matter that does not emit, absorb, or reflect light, making it invisible to electromagnetic observation. Despite its invisibility, its presence can be inferred from its gravitational effects on visible matter. DM constitutes the majority of the universe's mass, with visible matter accounting for a mere 30% of the total mass necessary to account for gravitational effects [34].

The first evidence of DM came from the observation of the rotation curves of galaxies. According to Newtonian gravity, the velocity of stars in a galaxy should decrease as they move away from the center due to the decreasing gravitational force. However, observations showed that the velocity of stars remained constant or even increased with increasing distance from the center. This indicated the presence of additional mass in the galaxy that could not be accounted for by visible matter [35].

Further evidence for dark matter came from the study of the cosmic microwave background radiation. Small temperature fluctuations have been observed, which are thought to be the result of fluctuations in the density of matter in the early universe. These fluctuations can be modeled and compared to observations to determine the amount of matter in the universe [36].

The quest to understand the composition of DM and its potential interaction with visible matter has spurred the development of various theories. The Atomic Experiment for Dark Matter and Gravity Exploration AEDGE [37] proposes a space based experiment that employs cold atoms to investigate one of them: Ultra-light bosonic fields. However, the experiment's potential goes beyond dark matter detection, as it could serve as a highly sensitive gravity

sensor that can detect gravitational waves.

### 1.2.4 Gravitational waves

According to Einstein theory of relativity, energy and space-time curvature are dependant

$$R_{\mu\nu} - \frac{1}{2}Rg_{\mu\nu} + \Lambda g_{\mu\nu} = \frac{8\pi G}{c^4}T_{\mu\nu} \tag{1.4}$$

Gravitational waves (GW) are ripples in the fabric of spacetime caused by the acceleration of massive objects [38]. These waves propagate at the speed of light and have a characteristic strain, or amplitude, that decreases with distance.

The first detection was made by the Laser Interferometer Gravitational-Wave Observatory (LIGO) in 2015, and since then, several other detections have been made by LIGO and the Virgo detector. [39].

The study of GW has opened up a new field of astrophysics, known as GW astronomy. This field is rapidly expanding, with new detectors built and planned around the world, among which is the Laser Interferometer Space Antenna (LISA) mission. Based on the principles of atomic interferometry, the MIGA project, developed in Bordeaux, stands as a demonstrative venture aimed at the detection of GWs [10].

GWs are also of fundamental importance to our understanding of the nature of gravity and the universe as a whole. The detection of GW has confirmed the existence of black holes and neutron stars, as well as the validity of Einstein's theory of general relativity in the strong-field regime. Its exploration could confirm or eliminate candidates for an extension of the standard model [42].

## 1.3 Atomic two-photon interferometry

In the realm of atomic interferometry methods predicated on the utilization of both ground and excited states, the excitation process does not need to be direct. In contemporary practice, a substantial portion of current atomic interferometers harness a two-photon mechanism for the excitation of atoms from their ground state to an excited state. Alkali atoms, which typically exhibit such transitions in the microwave domain, are commonly used for atomic

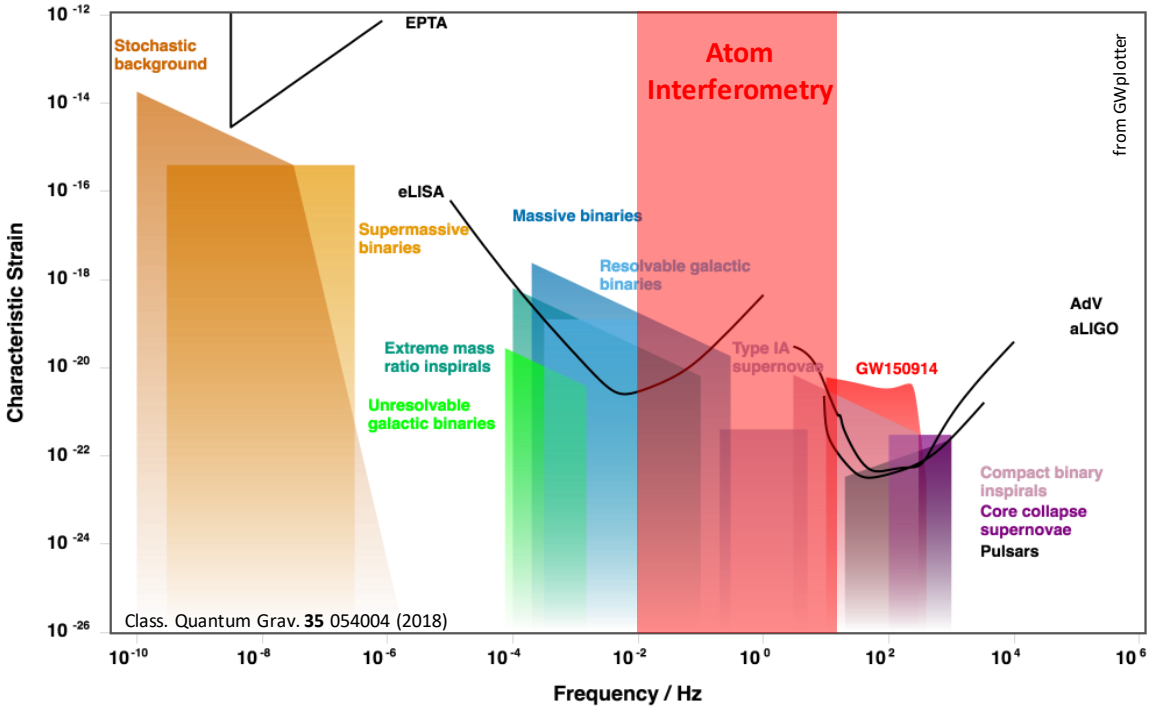


Figure 1.3: Different GW sources according to their frequency domain. GW150914 refers to the first GW measurement by the LIGO project [40, 41].

interferometry, making rubidium a popular choice.

### 1.3.1 Description of the clock transition in the context of two-photon interactions

Let us consider a set of three states denoted as $|a\rangle$, $|b\rangle$, and $|c\rangle$, where $|b\rangle$ exhibits a long decay time towards $|a\rangle$. The transition $|a\rangle \rightarrow |b\rangle$ is designated as the "clock transition." This specific transition can be effectively manipulated by utilizing two distinct photons with different frequencies, thereby interrogating the transitions $a \rightarrow c$ and $b \rightarrow c$. Thus, the atom see the beating between those two counter-propagating fields, at a beating frequency called the Raman frequency, and undergoes the transition

$$|a; p\rangle \rightarrow |b; p + \hbar(k_1 - k_2)\rangle \tag{1.5}$$

where p is the initial atomic momentum and $k_1$ and $k_2$ the photon momentum of two counter-propagating beams. As the two beams are counter-propagating, the quantity $k_1 - k_2$ is approximately $2k$ with $k \approx |k_1| \approx |k_2|$.

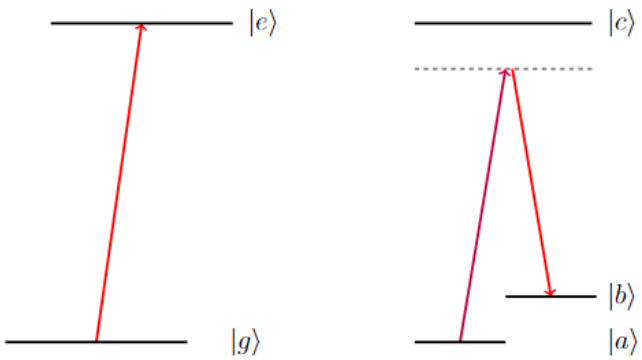


Figure 1.4: On the left, the clock transition between the fundamental state $|g\rangle$ and the excited state $|e\rangle$, is addressed directly via a single-photon transition. Whereas on the right, the transition is addressed via beating two optical fields at the frequency of the clock transition.

If the transition from state $|a\rangle$ to state $|b\rangle$ is very narrow, it may not necessarily be the case for the transitions from states $|a\rangle$ to $|c\rangle$ and $|b\rangle$ to $|c\rangle$. Therefore, if the frequency difference between the two laser beams used to drive these transitions needs to be as close as possible to the $|a\rangle \rightarrow |b\rangle$ transition frequency, the detuning of each laser from the optical transition has to be high in order to avoid populating the intermediate $|c\rangle$ state.

### 1.3.2 Methods using two-photon interferometry

In recent decades, the clock transition of alkali atoms has been utilized in various types of interferometers.

**Raman atomic interferometry**

Raman interferometry is a straightforward two photon based interferometry. In this situation, one laser is in a continuous mode while a second laser is pulsed following the $\frac{\pi}{2}$, $\pi$ and $\frac{\pi}{2}$ sequence. The beating between the two lasers is at the frequency of the clock transition. The Kasevich and Chu experiment of 1991 [4] is widely regarded as the first successful demonstration of Raman interferometry. In this experiment, a laser-cooled sample of sodium atoms was used to measure gravity acceleration using a Raman interferometer.

Recent advances in Raman atomic interferometry have led to the development of highly sensitive sensors for a variety of applications, including inertial navigation, geodesy, and gravitational wave detection [18, 43]. Additionally, Raman atomic interferometry promises

applications in fundamental physics research, such as tests of the equivalence principle [44, 45] and searches for new physics [46].

**Bragg atomic interferometry**

An interferometric scheme alternative to that based on Raman pulses is the Bragg interferometry. In this technique, standing optical waves are used to create a diffraction grating for the matter-waves. The Bragg condition, which requires the momentum transfer to be equal to the photon momentum, is satisfied when the angle between the atomic beam and the standing optical wave is a multiple of the Bragg angle $\theta_{\mathrm{n}}$ given by the relation

$$\lambda_{\mathrm{L}} \sin\theta_{\mathrm{n}} = n\lambda_{\mathrm{dB}} \tag{1.6}$$

with $\lambda_{\mathrm{L}}$ the laser wavelength, $n$ an integer of $\mathbb{N}$, $\lambda_{\mathrm{dB}}$ the de Broglie wavelength of the atom and $\theta_{\mathrm{n}}$ the Bragg angle [47].

This results in a two-photon transition between two momentum states that are symmetrically diffracted. The Bragg beams are typically applied for a certain duration, creating two spatially separated and coherent wave-packets that recombine after a variable time-of-flight, generating an interference pattern but with the notable difference that the internal atomic state does not change

$$|f;p\rangle \rightarrow |f;p+\hbar k\rangle \tag{1.7}$$

which is the main difference with Raman interferometry.

**Ramsey-Bordé atomic interferometry**

First demonstrated by Norman Ramsey in 1950, Ramsey fringes arise when an atomic cloud undergoes interactions with two successive electromagnetic fields [48]. Consequently, two quantum paths interfere at a rate determined by the time of flight between the two field regions.

This approach encounters limitations when the collimation of the atomic beam is not finer than $\lambda/L$, where $\lambda$ represents the laser wavelength and $L$ signifies the laser beam size. This averaging effect tends to suppress the fringes. Consequently, observing Ramsey fringes in the optical domain proved to be technically challenging.

In 1984, Christian Bordé addressed the issue of Ramsey fringe cancellation for optical transitions [49]. Ramsey-Bordé atomic interferometry relies on two pairs of $\frac{\pi}{2}$ pulses inter-

rogating the wave packet, resulting in only two paths effectively interfering. The first two beams are traveling in one direction and the other two beams in the opposite direction. The fringes are encoded on the populations [50]

$$P_{\mathrm{e}} \propto \cos(4\pi(\nu - \nu_0 \pm \delta\nu_{\mathrm{recoil}} + \nu_{\mathrm{sys}})T + \Phi) \tag{1.8}$$

where $p_{\mathrm{e}}$ is the probability to find an atom in the excited state, $\nu$ the laser frequency, $\nu_0$ the transition frequency, $\delta\nu_{\mathrm{recoil}}$ the atomic recoil frequency, $\nu_{\mathrm{sys}}$ all of the systematic frequency shifts of the system, $T$ the evolution time between two beams of the same pair and $\Phi$ the phase difference accumulated.

### Bloch Oscillations

In 1928, Felix Bloch predicted that a single charge placed in a periodic potential and subjected to a constant force would exhibit a periodic oscillation of its position, in contrast to the uniform motion that would typically be expected.

For cold atoms, a standing wave can play the role of the periodic potential. If this standing wave is fixed it allows an external force such as gravity to induce an oscillation of the atomic momentum [51]. Those Bloch oscillations can be seen as an inteferometer in momentum space [52] and the frequency of the Bloch oscillation is proportional to the force applied

$$\omega_{\mathrm{B}} = \frac{Fd}{\hbar} \tag{1.9}$$

Here, $d$ refers to the lattice parameter.

In atom optics, Bloch oscillations can also refer to another experiment, where the force acting on the atoms is induced by an acceleration of the optical lattice. Specifically, by chirping the laser frequency while the atoms are coherently manipulated, the atomic Doppler shift resulting from the photons' kick is compensated, leading to an adiabatic increase of the atomic momentum by $2\hbar k$ at each cycle [28]. This type of Bloch oscillations can be utilized to induce large momentum transfer (LMT) to the atoms without affecting their internal states.

### 1.3.3 Fundamental limitation of the two-photon method for gravitational wave sensors

In 2008, Dimopoulos *et al.*. proposed the first gradiometer to detect gravitational waves based on atomic interferometry [53].

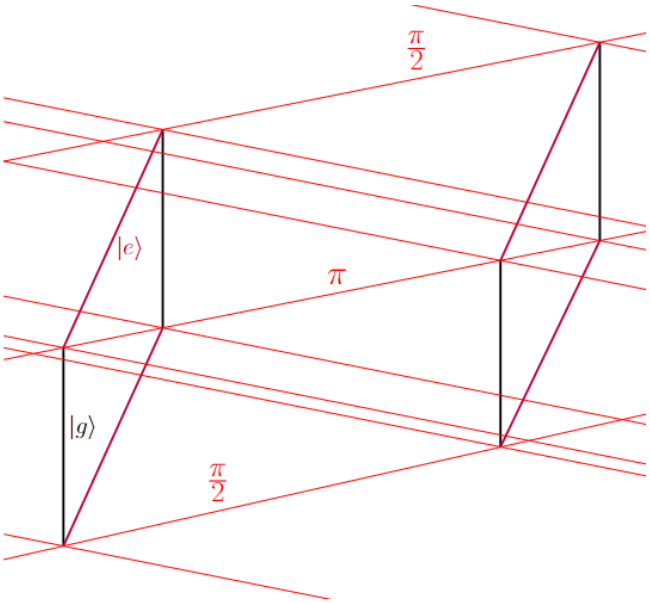


Figure 1.5: Space-time diagram of two atomic interferometers manipulated via a two photons transition. Each of the $\pi$ and $\frac{\pi}{2}$ pulses is generated by the beating between two lasers.

In this configuration of a gravity-gradiometer, two test masses are separated by a distance $L$ and subjected to a $\frac{\pi}{2}$ - $\pi$ - $\frac{\pi}{2}$ sequence. When employed as a GW detector, this setup probes the local phase shift of the optical link established for the pulse sequences. By a measurement of the phase evolution, it becomes possible to discern whether the space-time between the test masses is undergoing oscillations.

$$\phi = hk_{\text{eff}}L \tag{1.10}$$

with $k_{\text{eff}}$ the effective momentum transferred to the atoms.

In this configuration, atoms and light can either co-propagate or travel orthogonally. In both scenarios, this atomic interferometer attains its highest sensitivity when the axis connecting the test masses is orthogonal to the propagation direction of the gravitational wave.

One laser is in common mode with both test masses, while the other is not, resulting in the encoding of its noise in the interferometer's phase. This imposes a constraint on atomic interferometers employing Raman transitions within a single baseline. Introducing a second baseline addresses this limitation, albeit with associated budgetary and technical challenges. Alternatively, the utilization of single photon transitions instead of Raman transitions provides a solution.

## 1.4 Atomic single-photon interferometry

### 1.4.1 Basic principle

A scheme to remove the requirement of having a Michelson interferometer configuration to mitigate the impact of the laser technical noise has been proposed in [54, 55].

The principle of the atomic interferometer remains the same as that of the Raman transition scheme. However, instead of utilizing two counterpropagating beams to address a microwave transition, this scheme employs a single beam to address an optical transition.

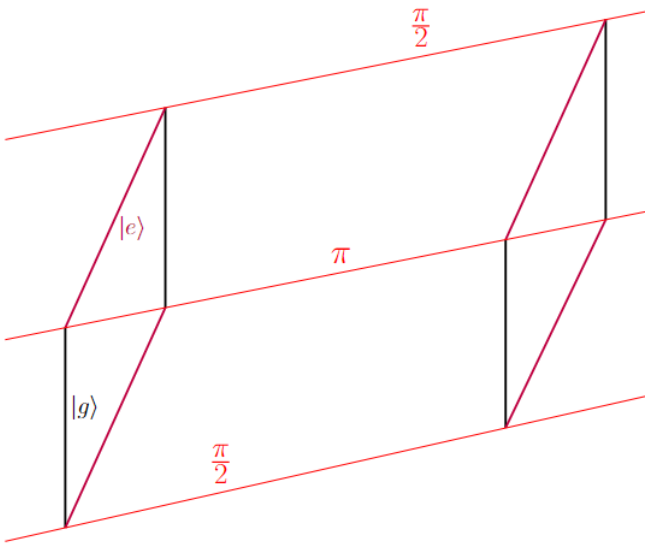


Figure 1.6: Space-time diagram of two atomic interferometers coherently manipulated via a single photon transition. Each of the $\pi$ and $\frac{\pi}{2}$ pulses are from the same laser field.

To implement the $\frac{\pi}{2}$ - $\pi$ - $\frac{\pi}{2}$ sequence in the proposed single-photon transition scheme, a single laser beam tuned at the clock frequency is pulsed. This pulse splits the wave packet,

deflects the atomic trajectories, and recombines the wave packet.

### 1.4.2 Technical aspect

In contrast to the two-photon scheme, the single-photon approach introduces a novel challenge regarding the linewidth of the employed laser. This arises due to the inherent narrowness of clock transitions, which is crucial to evade limitations posed by decoherence effects. Consequently, addressing such transitions directly demands a laser source with an adequately narrow linewidth. Only recent advancements in laser technology have made it possible to attain a linewidth that meets this stringent criterion.

This trend aligns with the efforts of the atomic clock community [56], which is exploring the feasibility of substituting microwave transitions with optical counterparts. When constructing a highly efficient atomic clock, two pivotal parameters come into play: a significantly elevated absolute frequency and an exceedingly narrow linewidth. Optical transitions hold promise in this regard due to their inherently elevated frequency, approximately 10,000 times greater than that of microwave transitions. Consequently, these optical transitions emerge as exceptionally promising candidates for propelling the next generation of atomic clocks. It is noteworthy that other transition types, such as Mössbauer transitions, offer even higher absolute frequencies, reaching around $10^{19}$ Hz, coupled with relatively long decay times of about 10 seconds [57]. However, the current inability to accurately tally the oscillation cycles of such high-frequency fields renders Mössbauer transitions impractical within the context of atomic clocks.

### 1.4.3 Candidates for single-photon interferences

To achieve successful single-photon interferometry, the choice of atoms with optical transitions within the spectral range accessible by current laser technology is crucial. Furthermore, these atoms must possess a natural linewidth that yields long-lived excited states while also being experimentally accessible. Such atoms are considered prime candidates for utilization in single-photon interferometry, as they allow for the efficient generation of high-momentum wave packets that can be manipulated by laser fields to produce interference patterns with

high contrast.

The narrowest lasers available today are limited by the thermal noise of their locking cavity [58], resulting in a linewidth of approximately 10 mHz [59]. For single-photon interferometry, a candidate atom with an optical transition should have a natural linewidth narrower than the characteristic time of the phenomenon probed by the interferometer.

The use of alkaline-earth-like atoms in single photon atomic interferometry is highly promising, given the excellent suitability of these atoms with respect to the conditions mentioned above. Among the alkaline-earth-like atoms, strontium (Sr) is an especially promising candidate due to its relatively narrow natural linewidth, accessibility by laser technology, and established utilization in other domains of physics beyond atomic interferometry. Additionally, other alkaline-earth-like atoms such as Calcium (Ca), Magnesium (Mg), Ytterbium (Yb), and Cadmium (Cd) also exhibit natural features having shown potential for use in single photon atomic interferometry.

# Chapter 2

# The Choice of Strontium

Opting for a direct transition instead of a two-photon process affords the construction of an atomic interferometer wherein the laser field engages the atomic cloud within a solitary baseline. Given its inherent level configuration, strontium emerges as a prime candidate for such an experimental pursuit.

Section 2.1 outlines the principal applications of this atom, complemented by a historical overview of its discovery. Delving further, Section 2.2 elucidates the level structures of the isotope 88, placing emphasis on the transitions salient to the cooling process. The subsequent Section 2.3 presents a repertoire of alkaline-earth-like candidates, describing the properties that render them apt for the realm of single-photon interferometry.

---

## Contents

## 2.1 Introduction to the atom

In recent years, there have been significant advancements in the field of atomic physics regarding strontium. Notably, the successful demonstration of a Bose–Einstein condensate (BEC) consisting of $10^7$ atoms [60, 61, 62], followed by the groundbreaking achievement of the first continuous BEC in 2022 [63].

Strontium's appeal is further reinforced by the utilization of fermions in cutting-edge optical lattice clocks employing $^{87}$Sr isotopes [64], as well as the creation of deeply degenerate strontium Fermi gases [61]. These recent developments have positioned strontium as a highly versatile and promising system for exploring various fundamental phenomena in ultracold atomic physics.

### 2.1.1 The discovery of strontium

The element strontium derives its name from the village of Strontian, where lead mines were discovered in 1722 by Sir Alexander Murray of Stanhope. The York Building Company operated the mine until 1815. Presently, there are no indications of mining activity in the area.

In the late 18th century, significant discoveries regarding the properties of strontium were made by Adair Crawford, an Irish physician at St Thomas's Hospital, and his assistant Thomas Cruikshank. While investigating the clinical applications of barium, Thomas Cruikshank observed that the Strontian ore exhibited distinct characteristics compared to other sources of

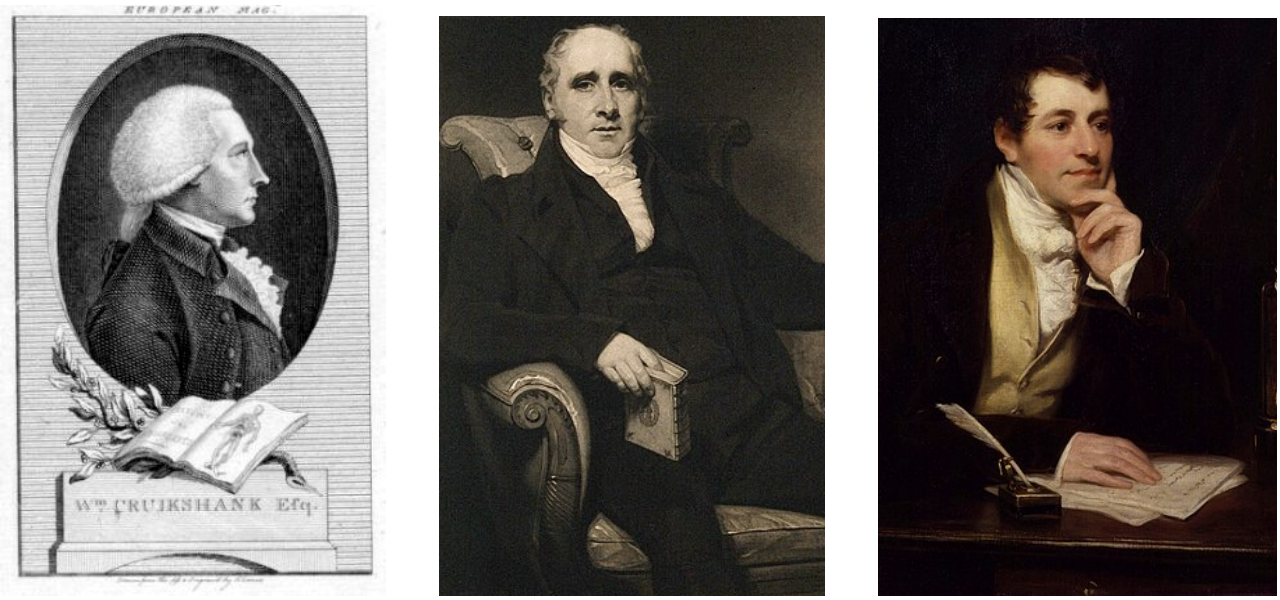


Figure 2.1: Principle chemists participating on the discovery of strontium. From left to right: William Cruickshank, Thomas Charles Hope and Humphry Davy.

"heavy spar". This observation led Crawford to draw a noteworthy conclusion, as stated on page 355 of his work from 1790 [65].:

"*It is probable indeed, that the Scotch mineral is a new species of earth which has not hitherto been sufficiently examined.*"

The first link between strontium's properties with those of calcium and barium was established in 1793 by Thomas Charles Hope, a professor of medicine at the University of Glasgow and physician to Glasgow Royal Infirmary. In his paper "Account of a Mineral from Strontian, and of a peculiar Species of Earth which it contains", as well as confirming Cruikshank and Crawford observations, the name "Strontites" is given by the physician [66]:

"*Considering it as a peculiar earth, I thought it necessary to give it a name: I have called it Strontites, from the place where it was found; a mode of derivation, in my opinion, fully as proper as from any quality it may possess, which is the present fashion.*"

It was not until 1808, approximately 15 years later, that Sir Humphry Davy successfully isolated the element strontium. He achieved this feat through the process of electrolysis, using a voltaic cell that had been introduced by Alessandro Volta eight years prior. Sir Humphry Davy made this significant breakthrough by electrolyzing strontium chloride. Furthermore, it

was Davy who officially named the element "strontium". He made this announcement during a lecture delivered to the Royal Society [67]:

*"These new substances will demand names; and on the same principles as I have named the bases of the fixed alkalies, potassium and sodium, I shall venture to denominate the metals from the alkaline-earths barium, strontium, calcium, and magnium;"*

### 2.1.2 Principal scientific applications

While strontium indeed finds extensive use in the matter-wave community for applications such as atomic interference [55], Bose-Einstein condensates [63] and atomic clocks [64], its scientific applications are not limited solely to these areas.

**Applications for general public**

Strontium has found significant use in various industrial and consumer applications. One notable industrial application is the manufacturing of cathode ray tubes (CRTs) for displays [68]. Strontium carbonate, known for its ability to absorb X-rays, was used in the production of CRT glass. Widely used in televisions and computer monitors until the 1990s, alternative display technologies began to replace them, leading to a decline in the use of strontium carbonate in this industry.

Another application of strontium is in the field of pyrotechnics: strontium salts, such as strontium nitrate or strontium carbonate, are added to fireworks compositions to produce a vibrant deep red color [69]. This is approximately 5% of global strontium production [68].

Finally, as it is biologically inert, strontium aluminate is employed for the production of toys due to its glow-in-the-dark properties.

**Applications in archaeology**

Strontium, due to its similarity to calcium, can be incorporated into bones. The natural isotopes of strontium are assimilated in proportions that reflect their abundance in the environment, and these isotopic ratios remain relatively stable even after burial. However, the specific distribution of strontium isotopes can vary significantly from one geographic region to another. As a result, the Sr isotope ratio in a bone sample can provide valuable information about its geographic origin [70, 71].

This technique has been applied to the analysis of human remains, particularly in the context of battlefield archaeology, to identify the origins of soldiers and reconstruct migration patterns during specific historical periods [72].

In addition, the analysis of Sr isotopes in bones has been utilized for source determination of ancient archaeological materials. By examining the ratios of $^{87}Sr/^{86}Sr$, researchers can identify the geographic sources of materials such as timbers and corn, providing valuable information about major construction events [73].

Furthermore, the Sr isotope analysis has been employed to track animal migrations by analyzing the Sr isotopic ratios in their teeth, offering insights into the movement patterns of ancient animal populations [74].

**Application in medicine**

In a pioneering study conducted by Hahn *et al.* in 1999 [75], the local application of strontium on irritated skin was investigated as a potential method to alleviate sensory irritation, specifically targeting the suppression of discomfort without inducing the typical side effects associated with local anesthetics. This significant finding highlights the potential of strontium as a promising agent for mitigating skin irritation and providing relief, while preserving the normal sensory response.

### 2.1.3 Description of the main isotopes

Strontium exhibits a total of 35 isotopes. However, it is important to note that only four of these isotopes exist naturally: $^{84}Sr$, $^{86}Sr$, $^{87}Sr$, and $^{88}Sr$. While isotopes such as $^{89}Sr$ and $^{90}Sr$ have applications in pharmacology and as radioactive power sources, they are not naturally occurring isotopes of strontium.

**Natural abundance**

Among these isotopes, $^{88}Sr$ is the most abundant, accounting for 82.58% of the natural isotopes. This high abundance makes $^{88}Sr$ a favorable choice for experiments requiring a high atomic flux. The other naturally occurring isotopes include $^{84}Sr$, which represents 0.56% of the isotopic composition, $^{86}Sr$ with 9.86%, and $^{87}Sr$ with 7.00% [76].

To generate an operable atomic beam, strontium ovens typically need to be heated to a

minimum temperature of 500°C. At this temperature, the vapor pressure of strontium reaches a level sufficient to produce an atomic beam suitable for experimentation.

### Electronic properties

With an atomic number of 38, strontium belongs to the alkaline-earth group of elements and has two valence electrons in its outermost $5s$ shell. Many of the atomic properties of strontium can be understood based on this configuration.

When the two valence electrons are paired in the outer shell, their spins cancel each other out, resulting in a total spin of zero (S = 0). This corresponds to a singlet state, where only one spin component is possible.

On the other hand, when the two valence electrons are unpaired in the outer shell, they contribute to a total spin of one (S = 1). This corresponds to a triplet state, where three spin components are possible: -1, 0, and +1.

### Strontium statistics

With two valence electrons in the outer shell of strontium, the total electron number is even, which is a consequence of charge neutrality. According to the spin-statistics theorem, which establishes a connection between the spin of particles and their statistics, an alkaline-earth atom following bosonic statistics requires an integer nuclear spin. As a result, both the number of protons and the number of neutrons in the nucleus of the atom must be even.

When both protons and neutrons are paired in the nucleus, with their spins aligned in opposite directions, the overall nuclear spin becomes zero. This pairing of nucleons with anti-parallel spins leads to the absence of hyperfine structure in all bosonic alkaline-earth elements.

In the case of strontium, three of its natural isotopes, namely $^{84}$Sr, $^{86}$Sr, and $^{88}$Sr, are bosonic isotopes with a nuclear spin of zero. The only natural fermionic isotope of strontium, $^{87}$Sr, has a nuclear spin of 9/2, which is the highest among all stable alkaline-earth isotopes.

| Isotopes | Natural abundance | Neutron number | Statistics | Nuclear spin |
|---|---|---|---|---|
| $^{84}$Sr | 0.56% | 46 | Boson | 0 |
| $^{86}$Sr | 9.86% | 48 | Boson | 0 |
| $^{87}$Sr | 7.00% | 49 | Fermion | 9/2 |
| $^{88}$Sr | 82.58% | 50 | Boson | 0 |

Table 2.1: Natural abundance and nuclear properties of the four natural Sr isotopes.

## 2.2 The level structure of strontium

Every alkaline-earth element, including strontium, exhibits two distinct cooling transitions that are commonly used in experiments. The first transition occurs between the ground state $^1S_0$ and the excited state $^1P_1$, while the second transition takes place between the ground state $^1S_0$ and the excited state $^3P_1$.

In our specific experiment, we have chosen to focus on the isotope $^{88}$Sr. Therefore, the following discussion will primarily center around this particular isotope. However, where relevant, we will also make comparisons with other isotopes, especially $^{87}$Sr.

**Recall on selection rules**

In the realm of quantum mechanics, a transition between two states is deemed "possible" or "allowed" when the absolute value of the integral of the transition moment is relatively high. Conversely, a transition is considered "forbidden" if the transition moment integral approaches zero, although it is important to note that a transition is never truly forbidden unless the integral is exactly zero.

While the exact calculation of the transition moment integral can be intricate, an analysis of the wave function symmetry provides a set of rules, known as "selection rules," that offer insights into whether the integral will be significant or not. These selection rules are dependent on the specific type of spectroscopy under consideration, such as electronic, vibrational, or rotational spectroscopy. In the context of discrete electric dipole (E1) transitions, we will focus on three selection rules:

-The rigorous rule that imposes conditions on the total angular momentum $J$.

-The rule that pertains to the variation of the orbital angular momentum under the influence of $LS$ coupling.

-The selection rule that concerns the variation of the spin angular momentum $S$ under the

influence of $LS$ coupling.

| | Electric dipole (E1) |
|---|---|
| Rigorous rule | $\Delta J = 0, \pm 1$ (except $J = 0 \nleftrightarrow J = 0$) |
| $\Delta L$ under $LS$ coupling | $\Delta L = 0, \pm 1$ (except $L = 0 \nleftrightarrow L = 0$) |
| $\Delta S$ under $LS$ coupling | $\Delta S = 0$ |

Table 2.2: The three fundamental selection rules governing strontium spectroscopy [77]. The crossed double arrow symbol ($\nleftrightarrow$) denotes a forbidden transition.

Those rules are valid for atoms without hyperfine structure. Nevertheless, as $F$ follows the same form as $J$, similar rules can be found for atoms with hyperfine structures.

### 2.2.1 First cooling transition

For $^{88}$Sr, the first cooling transition occurs at a wavelength of 461 nm in the blue region. This transition, which takes place between the ground state $^1S_0$ and the excited state $^1P_1$, is commonly referred to as the "blue transition" and magneto-optical traps (MOT) using this transition are denoted "Blue MOT".

The blue cooling transition is characterized by a strong $E_1$ transition, making it highly allowed according to the selection rules. Consequently, the excited state has a relatively short lifetime which is approximately $\tau_{\mathrm{B}} = 5.22$ ns. A short lifetime corresponds to a broad linewidth of approximately $\Gamma_{\mathrm{B}} = 2\pi \times 30.5$ MHz, as predicted by the time-energy Heisenberg uncertainty principle.

The short lifetime of the excited state in the blue transition enables a high scattering rate when the atoms are interrogated by a laser field, making it a favorable choice for applications such as building a Zeeman Slower. However, one drawback of the blue cooling transition is the significant saturation intensity resulting from its large linewidth $I_{\mathrm{sat}} = \dfrac{\pi h c \Gamma}{3\lambda^3} = 40.7\mathrm{mW/cm^2}$ [15].

It is worth noting that the blue cooling transition satisfies the three selection rules mentioned previously, which is in line with the large linewidth exhibited by this transition.

**Repump transitions**

After undergoing the blue cooling transition, atoms in the $^1P_1$ state can spontaneously decay to the $(4d)^1D_2$ state, resulting in an open transition. The linewidth of this leaking transition

| | $^1S_0$ | $\rightarrow$ | $^1P_1$ | Selection rule |
|---|---|---|---|---|
| $S$ | 0 | | 0 | $\Delta S = 0$ : Allowed |
| $L$ | 0 | | 1 | $\Delta L = 1$ : Allowed |
| $J$ | 0 | | 1 | $\Delta J = 1$ : Allowed |

Table 2.3: Quantum numbers and verification of selection rules for the blue cooling transition in strontium. The Russel-Saunders notation is used to represent the total electronic spin $S$, the orbital angular momentum $L$ and the total angular momentum $J$ under the form $^{2S+1}L_J$.

is measured to be 620 Hz, corresponding to a lifetime of $\tau = 256$ $\mu$s [78]. Given that the lifetime of the blue cooling transition is approximately 50 000 times shorter, a branching ratio of 1:50 000 is considered for the decay to the leaking state.

Atoms that leak from the blue cooling transition can then undergo spontaneous decay either to the $^3P_1$ state with a linewidth of $\Gamma_1 = 2.2 \times 10^3 s^{-1}$, followed by decay back to the ground state via the red cooling transition, or to the $^3P_2$ state with a linewidth of $\Gamma_2 = 1.1 \times 10^3 s^{-1}$. The $^3P_2$ state is a dark state and requires repumping to bring the atoms back to the ground state.

In our experimental setup, atoms trapped in the $^3P_2$ state are connected to the $(6s)^3S_1$ state using a laser field at 707 nm. From the $^3S_1$ state, atoms can decay to any of the triplet $^3P_{1,2,3}$ states. Therefore, another laser field at 679 nm is employed to repump atoms in the $^3P_0$ state.

Alternatively, there are other repumping solutions available. For instance, repumping to the $(4d)^3D_2$ state can be achieved using a laser at 3.0 $\mu$m, repumping to the $(6d)^3D_2$ state can be done using a laser at 403 nm, and repumping to the $(5d)^3D_2$ state can be accomplished with a laser at 497 nm [79].

### 2.2.2 Second cooling transition

The $^3P_1$ state serves as both the final destination of the repumper lasers and the excited state for the "red transition" between the $^1S_0$ and $^3P_1$ states. This transition, occurring at a wavelength of 689 nm, involves a singlet-to-triplet transition and, therefore, does not adhere to the selection rule regarding the conservation of electronic spin, $\Delta S = 0$.

| | $^1S_0$ | $\rightarrow$ | $^3P_1$ | Selection rule |
|---|---|---|---|---|
| $S$ | 0 | | 1 | $\Delta S = 1$ : **Forbidden** |
| $L$ | 0 | | 1 | $\Delta L = 1$ : Allowed |
| $J$ | 0 | | 1 | $\Delta J = 1$ : Allowed |

Table 2.4: Quantum numbers and verification of selection rules for the red cooling transition in strontium.

Nevertheless, due to the spin-orbit interaction between $^1P_1$ and $^3P_1$, a weak E1 transition is allowed. The linewidth of the red cooling transition is significantly smaller compared to that of the blue cooling transition $\Gamma_{\mathrm{R}} = 2\pi \times 7.4$ kHz, corresponding to a lifetime of 21.4 $\mu s$. Consequently, the saturation intensity for the red cooling transition, $I_{\mathrm{sat}}$, is more easily attainable in practical settings, with a value of 3 $\mu$W/cm$^2$.

While some alkaline-earth atoms may have broad enough $^1S_0 \rightarrow^3 P_1$ transitions to be used as the sole cooling transition, in the case of strontium, it is preferable to initially load the atoms into a blue MOT using the blue transition. Subsequently, the atoms can be loaded into a red MOT using the red transition. This two-step process provides better control over the atom population and enhances the efficiency of the cooling process.

### 2.2.3 Clock transition

A "clock transition" is a fundamental concept in the field of atomic clocks, denoting a specific atomic transition utilized for precision timekeeping and interrogation of atoms. One of the crucial prerequisites for a clock transition is its narrow spectral width in the frequency domain, enabling high-accuracy frequency measurements.

In the case of strontium, the $^1S_0 \rightarrow^3 P_0$ transition at a wavelength of 698 nm [76] assumes the role of a clock transition. Notably, this particular transition deviates from the selection rules governing electronic spin, as observed with the red cooling transition, and also disregards the rigorous rule concerning total angular momentum.

In the case of $^{88}$Sr, due to the double violation of the selection rules, the excited state exhibits an exceptionally long lifetime of approximately 6000 years, corresponding to an extremely narrow linewidth of a few pHz, $\Gamma_{\mathrm{clock}} = 5.5 \times 10^{-12}\ s^{-1}$ [80]. While E1 selection rules provide insights into the decay rate of a transition, it is important to note that the

| | $^1S_0$ | $\rightarrow$ | $^3P_0$ | Selection rule |
|---|---|---|---|---|
| $S$ | 0 | | 1 | $\Delta S = 1$ : **Forbidden** |
| $L$ | 0 | | 1 | $\Delta L = 1$ : Allowed |
| $J$ | 0 | | 0 | $\Delta J = 0$ : **Forbidden** |

Table 2.5: Quantum numbers and verification of selection rules for the clock transition in strontium.

lifetime of Sr bosons is primarily influenced by the two-photon $E1M1$ decay processes.

However, for $^{87}$Sr, the clock transition is weakly allowed through nuclear and spin-orbit mixing, owing to its non-zero nuclear spin $I = 9/2$ [81]. Consequently, the linewidth of the clock transition is modified to $\Gamma_{\text{clock}} = 2\pi \times 1.35$ mHz, corresponding to a lifetime of 118 seconds [82]. The saturation intensity of the clock transition is then reduced to $I_{\text{sat}} = 0.41$ pW/cm$^2$.

**Summary**

| Name | States | Selection rules | | | $\lambda$ in nm | $\Gamma/2\pi$ | $I_{\text{sat}}$ |
|---|---|---|---|---|---|---|---|
| | | $\Delta S$ | $\Delta L$ | $\Delta J$ | | | |
| Blue cooling | $^1S_0 \rightarrow {}^1P_1$ | ✓ | ✓ | ✓ | 460.7333 | 30.5 MHz | 40.7 mW/cm$^2$ |
| Red cooling | $^1S_0 \rightarrow {}^3P_1$ | × | ✓ | ✓ | 689.2585 | 7.4 kHz | 3 $\mu$W/cm$^2$ |
| Clock ($^{88}$Sr) | $^1S_0 \rightarrow {}^3P_0$ | × | ✓ | × | 698.4457 | 5.5 $\times 10^{-12}$ s$^{-1}$ | $\sim 0$ |
| Clock ($^{87}$Sr) | $^1S_0 \rightarrow {}^3P_0$ | × | ✓ | × | 698.4457 | 1.4 mHz | 0.41 pW/cm$^2$ |

Table 2.6: Overview of key properties of the principal transitions involved in strontium.

### 2.2.4 Isotopic shifts

The various isotopes of strontium exhibit distinct frequency shifts in their spectroscopic lines attributed to differences in neutron count. Specifically, the isotope shift for $^{88}$Sr atoms amounts to several tens of megahertz per unit of mass, surpassing the linewidth of its corresponding transition.

These shifts typically reach approximately 100 MHz and can be readily achieved using acousto-optic modulators (AOMs). Consequently, switching between studying one isotope to the other within the same experimental setup, particularly with regard to the lasers employed for atomic manipulation, can become a straightforward process.

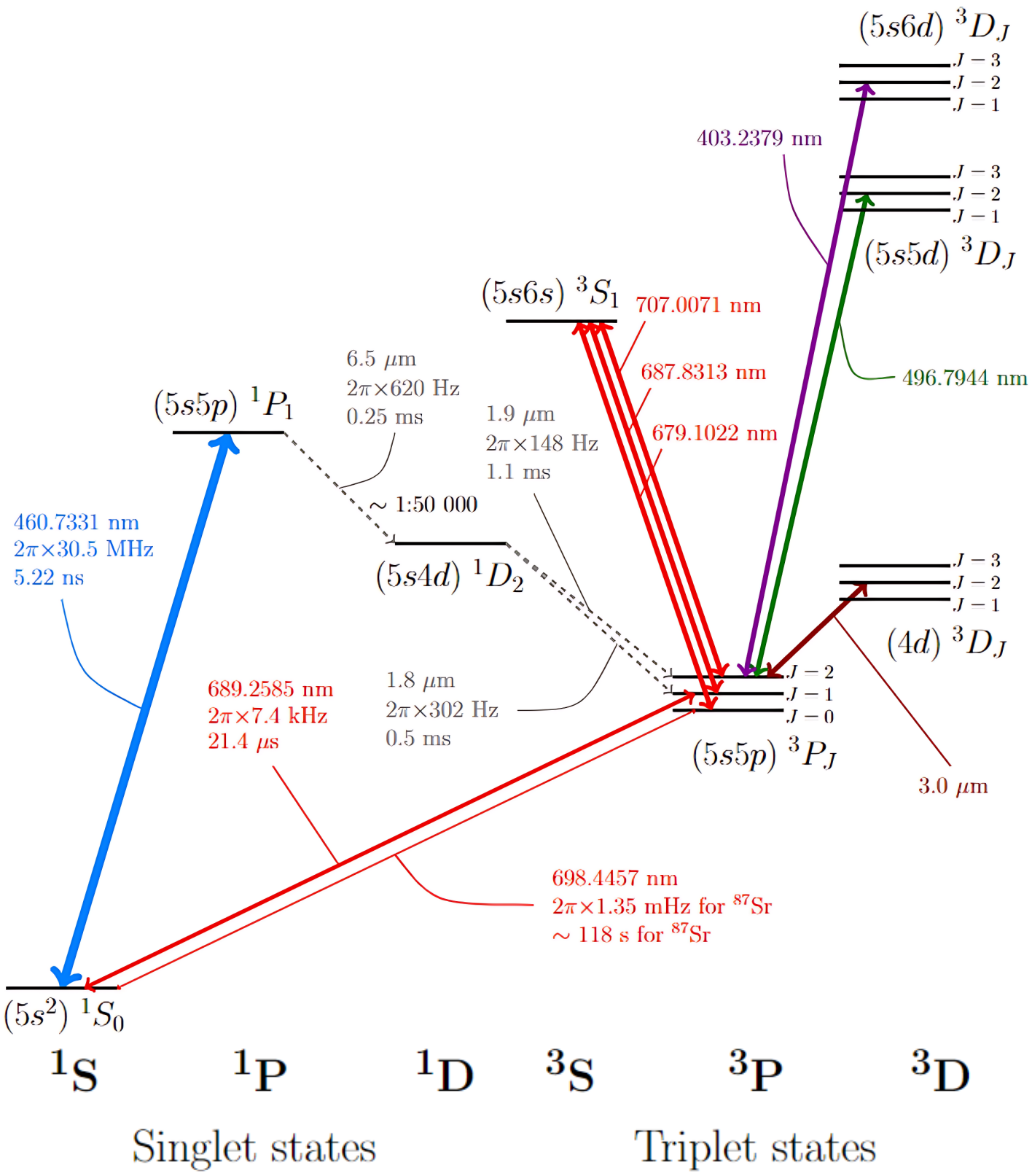


Figure 2.2: Level structure of $^{88}$Sr depicting linewidths, decay times, and wavelengths in air associated with each transition [83, 76, 84]. The line thickness corresponds to the magnitude of the linewidth, with thicker lines representing larger linewidths.

| Isotopes | Blue: $^1S_0 \rightarrow {}^1P_1$ | Red: $^1S_0 \rightarrow {}^3P_1$ |
|---|---|---|
| $^{84}$Sr | -270.8 | -351.5 |
| $^{86}$Sr | -124.8 | -163.8 |
| $^{87}$Sr | -46.5 | -62.1 |
| $^{88}$Sr | 0 | 0 |

Table 2.7: Isotopic shifts in MHz referenced to $^{88}$Sr for the blue cooling transition, as well as the red laser cooling transition [85]. In the case of the fermionic $^{87}$Sr atom, which possesses hyperfine structure, the shift is calculated with respect to an assumed $J = 0$ state.

## 2.3 Similarities with other alkaline-earth-like atoms

The term "alkaline-earth-like" is commonly used to describe elements belonging to the alkaline-earth group as well as certain two-electron systems that exhibit a comparable level structure to that of alkaline-earth elements. It should be noted that helium is not typically included in this category, as its weakest transition occurs in the extreme ultraviolet (XUV) range. Barium and radium will not be considered here due to the absence of a closed cycling first cooling transition. This is why these elements are less frequently chosen for studies and applications in atom optics.

### 2.3.1 Alkaline-earth atoms

#### Magnesium

Mg, the heaviest alkaline-earth-like atom, has garnered interest due to its ultranarrow clock transition at 70 $\mu$Hz between the $^1S_0$ and $^3P_2$ states, as demonstrated in the pioneering work by the Hanover group in the first Mg magneto-optical trap (MOT) [86].

Although Mg is not as commonly used in atom optics experiments compared to other elements, its lightweight nature leads to the shift of most of its transitions to the ultraviolet (UV) range, resulting in exceptionally narrow linewidths. This property confers Mg with remarkable resilience against the effects of blackbody radiation.

Furthermore, in the case of magnesium, the $^1D$ state lies above the $^1P$ state, enabling a closed first cooling transition at 285.2 nm [86]. The equivalent of the red cooling transition can be found at 457.1 nm. These features provide additional advantages and possibilities for

manipulating and cooling Mg atoms in experiments related to atom optics.

**Calcium**

Ca, with atomic number Z = 20, shares similarities with Sr in terms of its first-stage cooling. The counterpart of the blue cooling transition in Ca occurs at 423 nm, with a linewidth of 34 MHz, between the $^1S_0$ and $^1P_1$ states [87]. Atoms in the excited state can leak to $^1D_2$ with a branching ratio of approximately 1:100 000.

The second cooling stage in Ca operates at 657 nm with a narrow linewidth of 370 Hz, which is too narrow to be directly implemented in a MOT. As a result, the state $^3P_1$ is quenched using the $^1D_2$ state. This transition between the two states takes place at 453 nm and exhibits a linewidth of 5 kHz. This technique significantly enhances the scattering rate of the second cooling stage by approximately one order of magnitude, achieving temperatures as low as 6 $\mu$K [88].

### 2.3.2 Other two-electron atoms

**Mercury**

Hg, with an atomic number Z = 80, holds the distinction to be the heaviest atom successfully trapped, excluding radioactive species. Its trapping was first proposed by the Tokyo group in 2008 [89]. The utilization of Hg in atomic physics research is motivated by two key factors. Firstly, the clock transition of this element exhibits reduced sensitivity to blackbody radiation compared to other species. This characteristic enhances its potential as a high-precision atomic clock. Secondly, Hg is of interest in the context of exploring "new physics" beyond the standard model, as certain physical phenomena are significantly influenced by the atomic number. For instance, parity-violating amplitudes scale as $Z^3$ [90], while CP-violating polarizabilities scale as $Z^5$ [91].

Nevertheless, it is important to note that the blue cooling transition equivalent in Hg occurs at a wavelength of 185 nm, while the red cooling transition equivalent takes place at 254 nm. Achieving such wavelengths requires a two-stage frequency doubling process starting from infrared diodes. Notably, similar research on Hg trapping has been conducted by the SYRTE group in Paris [92].

**Cadmium**

Cd, with an atomic number Z = 48, possesses a highly intriguing characteristic: its level structure is identical to that of strontium when the transition frequencies are doubled. Although these frequencies were unattainable a few decades ago, advancements in technology now enable the production of degenerate clouds of cadmium atoms [93]. Consequently, by doubling the frequencies of every laser source utilized in a strontium setup, it becomes possible to construct an experimental setup based on cadmium.

| Transition | Atom | $\lambda$ (nm) | $\Gamma/2\pi$ | Is (mW/cm$^2$) |
|---|---|---|---|---|
| Blue: $^1S_0 \rightarrow {}^1P_1$ | Sr | 461 | 30 MHz | 42 |
| | Cd | 229 | 91 MHz | 992 |
| Red: $^1S_0 \rightarrow {}^3P_1$ | Sr | 689 | 7.4 kHz | $3\times10^{-3}$ |
| | Cd | 326 | 67 kHz | $2.5\times10^{-1}$ |
| Clock: $^1S_0 \rightarrow {}^3P_0$ | Sr | 698 | $\sim$1 mHz | $10^{-9}$ |
| | Cd | 332 | $\sim$1 mHz | $3\times10^{-9}$ |

Table 2.8: Comparative analysis of the three principal transitions in strontium (Sr) and cadmium (Cd).

The presence of a clock transition, along with the low sensitivity of cadmium to both electromagnetic fields and blackbody radiation, positions the Sr-Cd duo as a promising candidate for fundamental physics tests. These tests encompass a wide range of phenomena, including investigations into the weak equivalence principle, non-classical time dilation effects, and spin-gravity coupling [94]. The utilization of cadmium as a complementary element to strontium opens up possibilities for advancing our understanding of fundamental physics principles.

**Ytterbium**

Yb, with an atomic number Z = 70, exhibits a level structure that bears some similarity to strontium, although there are two key differences in practice. Firstly, the red cooling transition at 556 nm (appearing more green in Yb) possesses a linewidth of 182 kHz. As a result, it is possible to directly load a magneto-optical trap (MOT) from the second cooling transition. In fact, the $^1S_0 \rightarrow {}^1P_1$ transition at 399 nm, with a linewidth of 29 MHz, is primarily utilized for the Zeeman slower in Yb setups.

Secondly, the $^1D_2$ state where the atoms are leaking lies above $^1P_1$ in Yb. Thus, the leaking

of atoms from the blue cooling transition occurs predominantly through the triplet $^3D$ state, with a branching ratio of approximately 1:$10^7$. This branching ratio is significantly better than that of Sr. Furthermore, the transition at 399 nm can be easily accessed using a single laser diode, rendering it an excellent choice for implementation in a Zeeman slower [85].

Regarding clock transitions, Ytterbium offers two such transitions due to the ability of the $^3P_2$ state to decay to the $^1S_0$ state [95]. The transition between $^1S_0$ and $^3P_0$ at 578 nm exhibits a linewidth of $\Gamma_{c1} = 2\pi \times 10$ mHz, while the transition between $^1S_0$ and $^3P_2$ at 507 nm has a linewidth of $\Gamma_{c2} = 2\pi \times 15$ mHz.

Although Yb does not offer the same level of coherence precision as Sr, its high atomic mass and optical properties of its level structure makes it a favorable candidate for atom-optics-based experiments. Many research laboratories are conducting their investigations using Yb instead of strontium.

# Chapter 3

# Experimental Apparatus

This chapter is dedicated to an exposition of the experimental apparatus employed in the creation of a magneto-optical trap (MOT) centered around the utilization of $^{88}$Sr. In Section 3.1, an overview of the principal components constituting the setup is provided, with a particular focus on the various stages of the MOT construction essential for the generation of an isolated MOT distinct from the oven source. The laser system employed for this task is detailed in Section 3.2, while Section 3.3 delineates the process behind the generation of the diverse magnetic fields intrinsic to the cooling mechanism. Further insight into the matter is unveiled in Section 3.4, where we elaborate on the strategic methodologies harnessed for spectral properties crucial for interactions with $^{88}$Sr. Notably, the recent integration of a frequency comb at the LP2N has unveiled novel avenues for frequency stabilization. This addition not only serves as a novel tool but also opens new vistas for assessing the stability of a high finesse cavity. The ensuing Section 3.5 is devoted to the two aforementioned facets.

---

## Contents

## 3.1 The vacuum system

The realization of the atomic source has been done in collaboration with the research group led by David Wilkowski in Singapore. The vacuum system employed in this study can be categorized into three main components: the atomic beam-generating oven, the 2D-MOT (two-dimensional magneto-optical trap) chamber, and the 3D-MOT chamber. These chambers, constructed from stainless steel or titanium, have been designed with a compact layout that incorporates the utilization of permanent magnets as the source of the magnetic field for

both the MOT and the Zeeman Slower [96, 97]. However, the Zeeman Slower will not be discussed in this section, as it will be the subject of the next chapter.

Figure 3.1: Picture of the experimental setup.

### 3.1.1 The oven

The vacuum chamber has been designed to ensure close proximity between the oven and the 2D-MOT chamber, with a 25 mm diameter aperture serving as the interface between these two components. The oven is a cylindrical structure housing 5g of high-purity strontium (99% purity, Alfa Aesar).

In order to achieve satisfactory loading of a well-performing 2D-MOT, it is essential for the oven to be heated to temperatures above approximately 500-550°C, while the spectroscopy cell employed for saturation absorption can only be heated up to only 300-350°C.

Situated at a distance of 35 cm from the 2D-MOT chamber, on the opposite side of the oven, is located the viewport used to shine the cooling beam of the Zeeman Slower. Due to its location, this window is in direct sight of the thermal beam generated by the oven.

Consequently, the sapphire window is continuously maintained at a temperature of 380°C to prevent the viewport from coating by strontium deposit.

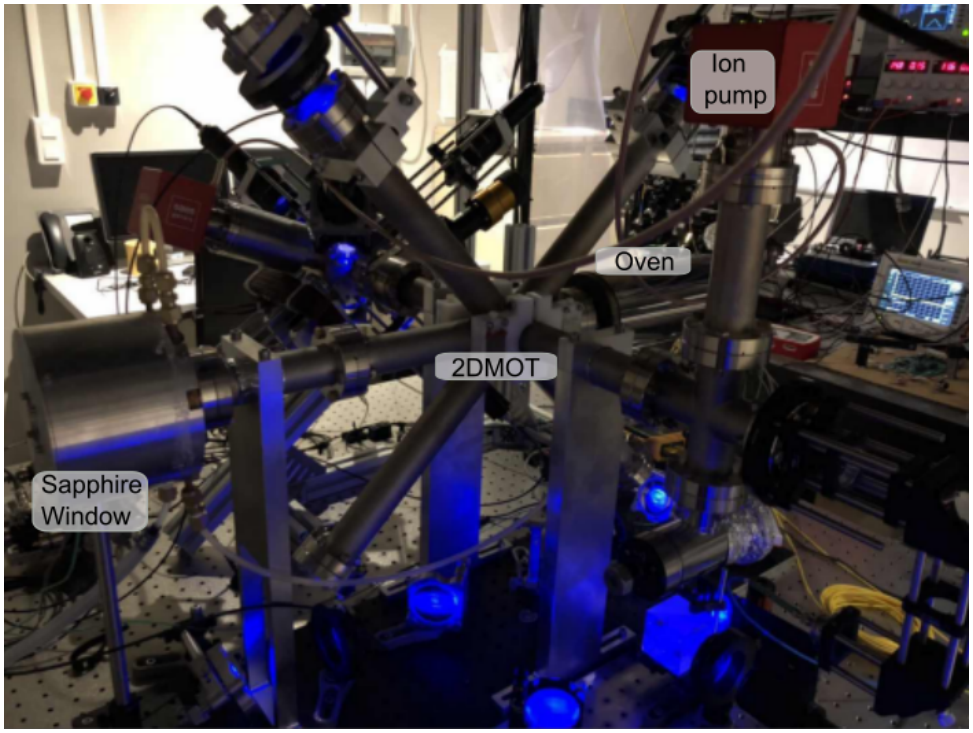


Figure 3.2: 2D-MOT chamber and the atomic source.

To mitigate the potential atomic beam divergence resulting from the 25 mm diameter aperture, an array of micro-sized nozzle tubes consisting of approximately 400 microtubes is employed. This arrangement effectively reduces the divergence of the atomic beam [98].

Considering that the oven and the sapphire window reach high temperatures during operation, the components connecting them to the main chamber are cooled through a water flow system to avoid heat transfer.

**Rotation of the setup**

The vacuum chamber, the oven and the sapphire window were originally aligned horizontally (see Figure 3.3, left). To investigate the potential atomic loss resulting from the positioning of the Sr source, a decision was made to rotate the 2D-MOT chamber by 90°. This adjustment ensures that the oven is now located at the bottom of the experimental setup. By reorienting the chamber in this manner, we aim to mitigate the effect of gravity on the parabolic atomic trajectories to minimize the losses and optimize the performance of the system.

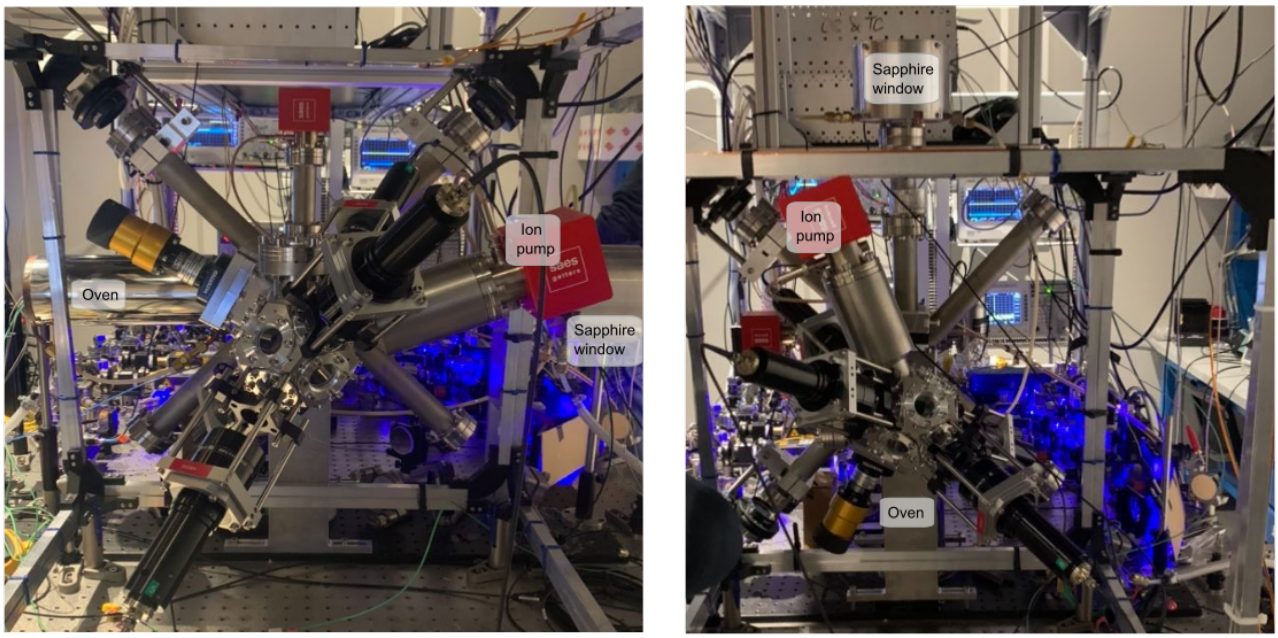


Figure 3.3: Left: Initial configuration of the atom source, with the oven generating a horizontal thermal beam. Right: After rotation. The oven is generating the thermal beam vertically.

By implementing this adjustment, we observed a significant increase in the atom number within the 2D-MOT by approximately a factor of four, while keeping other parameters unchanged. It is important to note that the enhanced atom number cannot be solely attributed to the fact that the atomic trajectories are less bent by gravity and thus having less constraint to escape from the oven. Another contributing factor is the direct interaction between the Sr granules and the Zeeman Slower beam, which leads to a higher ablation rate [99, 100].

This observation is further supported by the measured increase in pressure within the 2D MOT chamber. Within a minute of shining the two Zeeman Slower beams, even without injecting their diode sources (see part 3.2.2), the pressure in the chamber increased by one order of magnitude to descend then slowly.

### 3.1.2 The 2D blue MOT

A 2D-MOT refers to a magneto-optical trap configuration in which the laser beams used to interact with the atoms are confined to a single plane. The magnetic field is generated using four stacks of permanent magnets to establish a linear region of zero magnetic field.

Consequently, the atoms originating from the oven accumulate along a single line perpendicular to the plane of the laser beams. To enhance the transfer of these atoms from the 2D-MOT chamber to the 3D-MOT chamber, also known as the science chamber, a push beam is employed. This push beam is resonant with the atomic transition and has a power of approximately 100 $\mu$W. It is directed along the axis orthogonal to the laser beams' plane, providing a force that propels the atoms towards the science chamber.

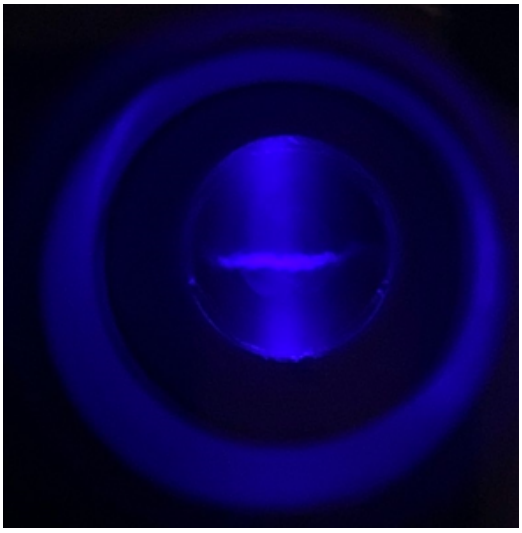

Figure 3.4: Side view of the 2D MOT from the sapphire window.

The 2D-MOT is established by utilizing the blue cooling transition at a wavelength of 461 nm. The laser beams used for cooling are detuned from this transition by $2\pi\times1.1\ \Gamma$, equivalent to a frequency shift of 34 MHz. By employing the blue cooling transition, the resulting Doppler temperature is determined to be $T_D = \frac{\hbar\Gamma}{2k_b} = 720\ \mu$K and a recoil temperature of $T_r = \frac{\hbar^2k^2}{k_bM} = 0.690\ \mu$K. Therefore, the atomic sample is limited by the Doppler temperature and is at the mK level.

The laser beams for the 2D MOT are produced using commercially available gallium nitride (GaN) blue laser diodes with a maximum power output of 500 mW. We operate the diodes at a reduced current and when considering the insertion loss of the optical isolator we use to protect them from optical feedback we obtain an effective power of $\sim$280 mW. If the laser beam is precisely collimated, the diode image is printed on the laser profile. Since the beam does not exhibit a TEM00 mode, a lens is placed in front of the diode's output to

slightly blur the beam, so as to make it more uniform (see Figure 3.5).

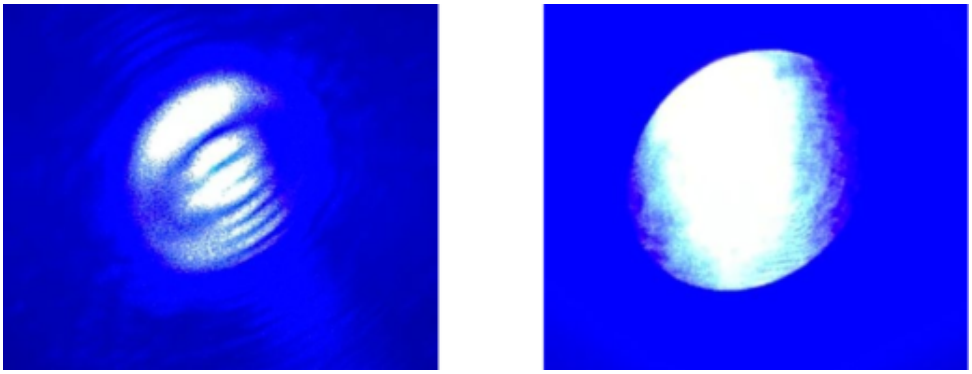

Figure 3.5: Left: 2D MOT beam profile when the lens collimates perfectly the diode beam. Right: 2D MOT beam profile slightly out of focus. As a homogeneous beam profile optimizes the 2D MOT operation, a small optical misalignment yields a more efficient beam profile.

The laser beam passes first in an optical isolator, then in a telescope (ratio 5:1) and is then split using a half-wave plate ($\lambda/2$) and a 2-inch polarizing beam splitter (PBS). This setup generates two retro-reflected beams, each with a power of 70 mW and a diameter of approximately 4 cm. The beams are slightly focused to compensate for any losses introduced by the optics during the reflection process. Before entering the 2D-MOT chamber, the beams pass through a quarter-wave plate ($\lambda/4$) and then undergo retro-reflection.

To minimize the losses, the viewports are anti-reflection (AR) coated within the wavelength range from 390 nm to 570 nm, and the losses due to reflections are estimated to be below 0.5%. Additionally, the deposition of strontium on the viewports can be mitigated by designing the 2D-MOT chamber with long arms, 30 cm in our setup, so that the viewports are out of sight of the high pressure thermal beam.

The magnetic field required for the 2D-MOT is generated by four stacks of permanent magnets (Neodymium Block Magnets N750-RB, Eclipse Magnetics Ltd). These magnets produce a quadrupole magnetic field with a strength of approximately 50 G/cm. The number of magnets used may vary depending on the specific configuration of the Zeeman Slower, which will be discussed in the next chapter.

An ion pump and a getter (SAES Getters, NEXTorr D200-5) are integrated into the setup to maintain a vacuum pressure of approximately $10^{-8}$ mbar in the 2D-MOT chamber when

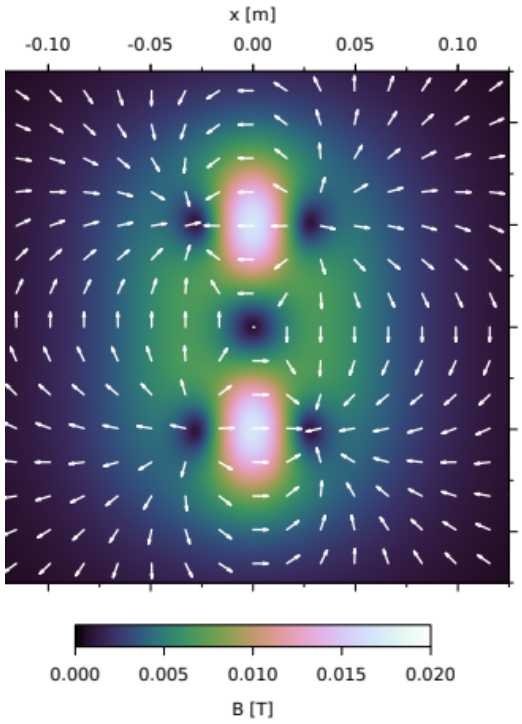


Figure 3.6: Magnetic field generated by four magnet stacks. The color represents the magnetic field's magnitude and the white arrows its direction. Credit: [97].

the oven is active. To create a differential vacuum pressure between the 2D-MOT chamber and the science chamber (3D-MOT chamber), we use a connection pipe. It is achieved by utilizing a connecting tube with a length of 22.8 mm and an inner diameter of 2 mm.

### 3.1.3 The 3D blue MOT

A 3D-MOT, in contrast to a 2D-MOT, refers to a magneto-optical trap that traps atoms in all three spatial directions using a standard quadrupole field with only one point where the magnetic field is zero.

The magnetic field required for the 3D-MOT is generated using a set of coils arranged the closest to the anti-Helmholtz configuration we could achieve. It was not possible to use circular coils due to geometrical constraints. The optical field is produced using the same scheme used for the 2D-MOT beams. The 280 mW delivered by another NICHIA diode after optical isolator are coupled to a fiber, which is connected to connected to a Schäfter+Kirchhoff fiber port cluster.

This device ensures a dual objective: Firstly, it redistributes the incoming laser light to the six arms of the 3D-MOT with high coupling efficiency ($\sim$80%) according to a balance ratio set by the different $\lambda/2$ incorporated. Secondly, it ensures the light for the blue MOT and the light for the red MOT overlap properly. Therefore, the same apparatus can be used for the blue MOT and for the red MOT (see part 3.1.4). In its first phase, the 3D MOT uses the blue cooling transition for atom trapping. However, there is a slight difference in the detuning applied for the 3D-MOT as it is set to 20 MHz, corresponding to $2\pi\times0.65\Gamma$.

The science chamber is designed to maintain an ultra-high vacuum below $10^{-10}$ mbar. This is achieved through the combination of a differential pumping channel towards the 2D MOT chamber and an ion-getter pump (SAES Getters, NEXTorr D200-5) attached to the chamber. Instead of stainless steel, the chamber is constructed from titanium and the viewports are sealed with indium. The fiber ports used for the laser beams are connected to the viewports via CF flanges. Not all viewports are utilized for the cooling process, some are reserved for specific purposes, such as housing repumpers, providing access to a photodiode, or giving access to a potential pulsed beam for an atomic interferometer setup.

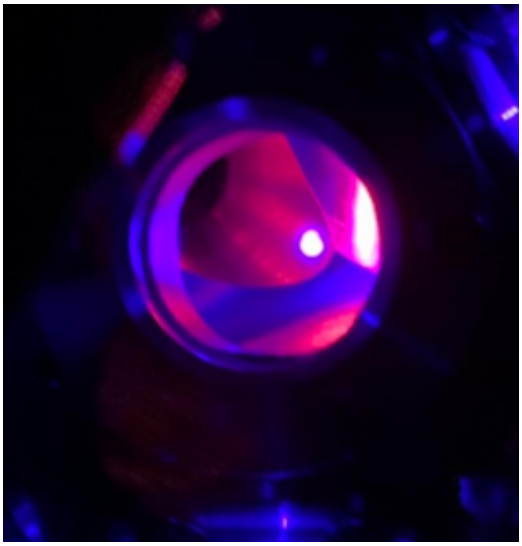

Figure 3.7: 3D blue MOT in steady state with repumpers on. According to [101], the atom number is estimated to be $\sim 7\times10^6$.

Using the blue cooling transition of $^{88}$Sr yields a MOT of $\sim$1 mK. This temperature correspond to a mean atomic velocity of $\sim$1 m/s.

The power scattered by a single atom is

$$P_{\text{scat}} = \frac{\Gamma}{2}\frac{s}{1+s+4\Delta^2/\Gamma^2}h\frac{c}{\lambda} \tag{3.1}$$

The lens collecting the flux scattered by the 3D-MOT is placed at d = 12 cm from the latter and has a radius of r = 12.7 mm. Thus the proportion of the power emitted by the 3D-MOT has to be corrected by a factor

$$\eta = \frac{\pi r^2}{4\pi d^2} \tag{3.2}$$

so approximately $2.8\times10^{-3}$.

The output voltage of the photodiode (PDF10A2, Thorlabs) is expressed in term of the incoming optical power $P_{\text{opt}}$ by the relation

$$V_{\text{out}} = P_{\text{opt}}R(\lambda)G \tag{3.3}$$

where $R(\lambda)$ = 0.25 A/W at 461 nm denotes the detector responsively $G = 1\times10^{12}$ V/A is the transimpedance gain. For the measurement in Figure 3.7, $V_{\text{out}}$ = 6 V.

Therefore, the atomic number in the 3D-MOT can be estimated as [101]

$$N = \frac{P_{\text{opt}}}{\eta P_{\text{scat}}} = \frac{V_{\text{out}}}{\eta P_{\text{scat}} T R(\lambda) G} \tag{3.4}$$

so approximately $7\times10^6$ atoms in the 3D-MOT.

### 3.1.4 The 3D red MOT

The red MOT is somewhat similar to the blue MOT but using the red cooling transition between $^1S_0$ and $^3P_1$ at 689 nm. The natural linewidth is $\Gamma_R = 2\pi\times7.4$ kHz which requires to reduce the laser linewidth to even smaller values to manipulate the atoms at this wavelength. Locking the laser to a high finesse cavity in a classic Pound–Drever–Hall (PDH) scheme is a common technique to achieve this goal. On the other side, the red transition is closed, hence it does not require any repumper and the saturation intensity is easily reached.

The red transition has the interesting particularity of having a lower Doppler temperature than recoil temperature. Thus, a red MOT can reach a temperature as low as 500 nK.

Moving from the mK MOT operated on the 461 nm light to the muK one operated on the

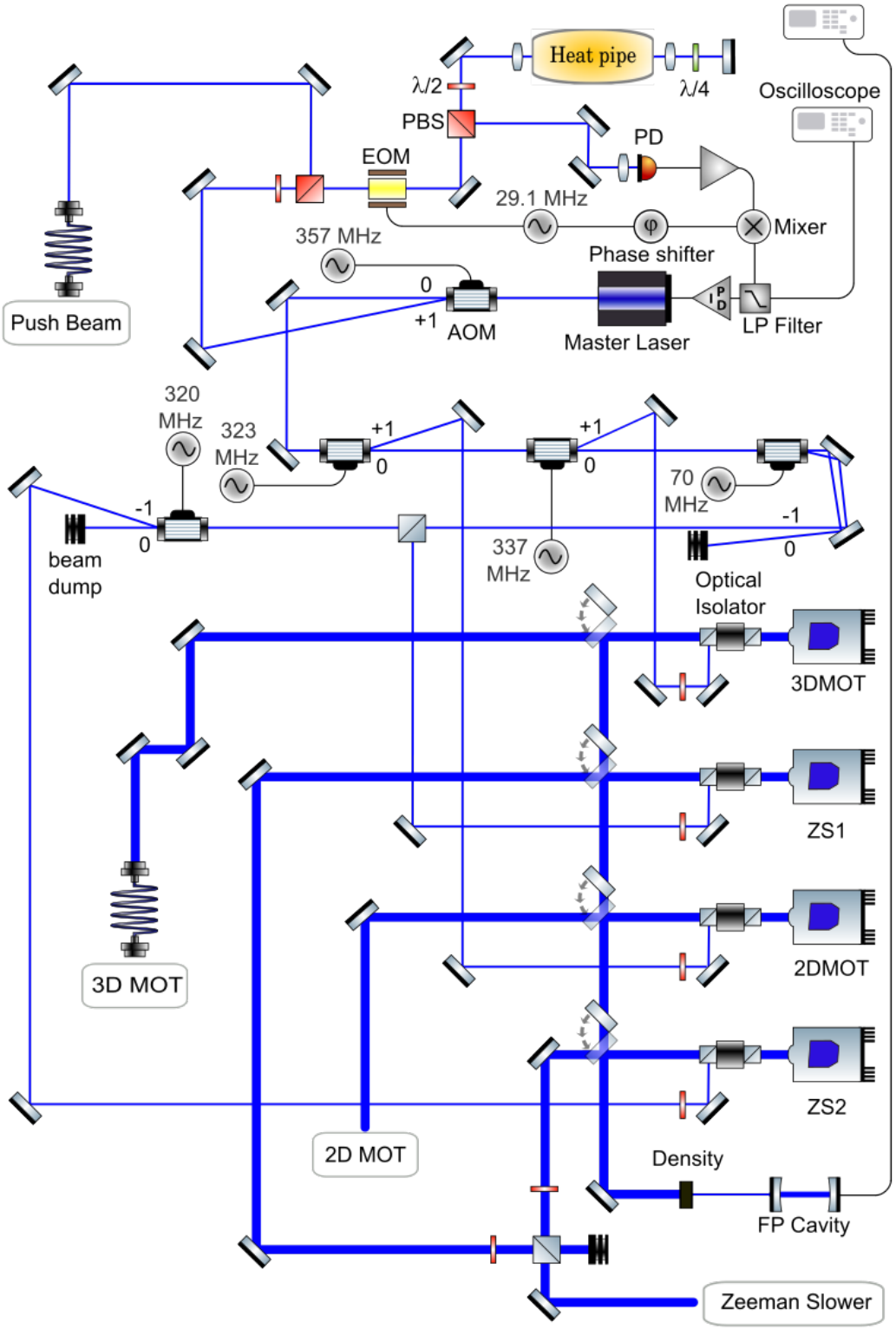


Figure 3.8: Setup relative to the Blue cooling transition. Thin blue lines represent 461 nm light at low intensity, thick blue lines at high intensity and black line represent electrical wires. EOM: Electro-Optic Modulator, AOM: Acousto-Optic Modulator, FB: Fabry-Perot, PD: Photo-Diode, LP filter: Low Pass filter.

| Transition | $\lambda$ (nm) | $\gamma/2\pi$ | $I_s$ | $a_{\text{max}}$ (m/s²) | $T_D$ | $T_{\text{rec}}$ |
|---|---|---|---|---|---|---|
| Blue | 460.7331 | 30.5 MHz | 41 mW/cm² | $9.3\times10^5$ | 720 $\mu$K | 690 nK |
| Red | 689.2585 | 7.47 kHz | 3 $\mu$W/cm² | 155 | 182 nK | 454 nK |

Table 3.1: Main parameters for cooling via the blue or the red transition. $a_{\text{max}} = \dfrac{\Gamma\hbar k}{2m}$ denotes the maximum acceleration an atom can undergo on a transition.

689 nm light requires a specific procedure. In order to efficiently capture all the atoms during the transition, a spectral broadening of the laser field at 689 nm has to be applied to match the Doppler profile of the 3D blue MOT.

This broadening can be produced via a modulation technique using an AOM whose modulation frequency is set to 25 kHz, covering a span of 800 kHz, and red-detuned by 400 kHz. The modulation results in the creation of 32 sidebands in the spectrum and it is important to note that even though the overall intensity of the light is much higher than the saturation intensity, care must be taken to ensure that each sideband has sufficient intensity above the saturation intensity level [102].

Another method to avoid losing atoms during the transition from the blue MOT to the red MOT is to produce a laser field with sufficient intensity to induce power broadening such that the effective linewidth of the red transition can be broadened to match the linewidth of the blue cooling transition. At resonance, the effective linewidth $\Gamma_{\text{eff}}$ due to power broadening is given by $\Gamma_{\text{eff}} = \Gamma_{\text{nat}}\sqrt{1 + I/I_S}$, thus a laser field with an intensity of 51 W/cm² probes all the atoms in the blue MOT.

In both methods, the effective linewidth of the cooling laser must be reduced to be narrower than the natural transition linewidth. In parallel, the magnetic field gradient has to be reduced from 50 G/cm² to 3 G/cm² [102]. Then, the MOT reaches its lowest temperature.

## 3.2 The laser system

### 3.2.1 Master laser

Two External-Cavity Diode Lasers (ECDLs) [103] from TOPTICA (DL Pro) are employed as master laser for both the blue MOT and the red MOT.

### Locking of the blue master laser

The master laser dedicated to the blue MOT is locked to a spectroscopic cell via FM saturation spectroscopy [104]. This method have similarities with PDH locking but applied for saturated absorption. It consists of a modulation of the laser frequency, typically using an electro-optic modulator (EOM), followed by a demodulation of the spectroscopic signal. If the laser frequency is within the Doppler profile, a modulation of the laser frequency causes a different absorption and therefore an amplitude modulation visible with a photodiode. If the mean frequency of the laser is near an extreme, the resulting amplitude modulation is negligible and the resulting signal after demodulation is near zero. If the mean frequency of the laser is on a rising slope of the absorption signal, the demodulating signal is in phase with the spectroscopic signal and yields a positive signal. On the other side, if the mean frequency of the laser is on a descending slope of the absorption signal, the demodulating signal is in phase opposition with the spectroscopic signal and yields a negative signal. The whole signal after demodulation is the derivative of the absorbing signal and is called "error signal".

The master laser is modulated at 29.1 MHz passing through an EOM (EO-F30M3-VIS, Qubig). Then, $\sim$1 mW of optical power is focused via a lens (f = 300 mm) into a heat pipe operating at 350°C containing Sr vapor at $10^{-8}$ mbar and $\sim 10^{-1}$ mbar of argon as a buffer gas to prevent the viewports from Sr deposit. The pump is retro-reflected into the heat pipe in a classical saturation absorption scheme. The probe is collected by a high-bandwidth photodiode after having been focused via a lens (f = 25 mm). More information about the limitations of saturated absorption are reported in part 3.4.3.

After demodulation and passing through a RF low pass filter, the error signal is sent to a commercial PID (Proportional-Integral-Derivative) from Koheron (PI200). A first output of the PID is sent to the laser diode to correct the fast fluctuations via the current while the second output is sent to the PZT of the ECDL to correct slow fluctuations. An offset is applied to the error signal thought the "setpoint mod" input to optimize the 2D-MOT's atomic number.

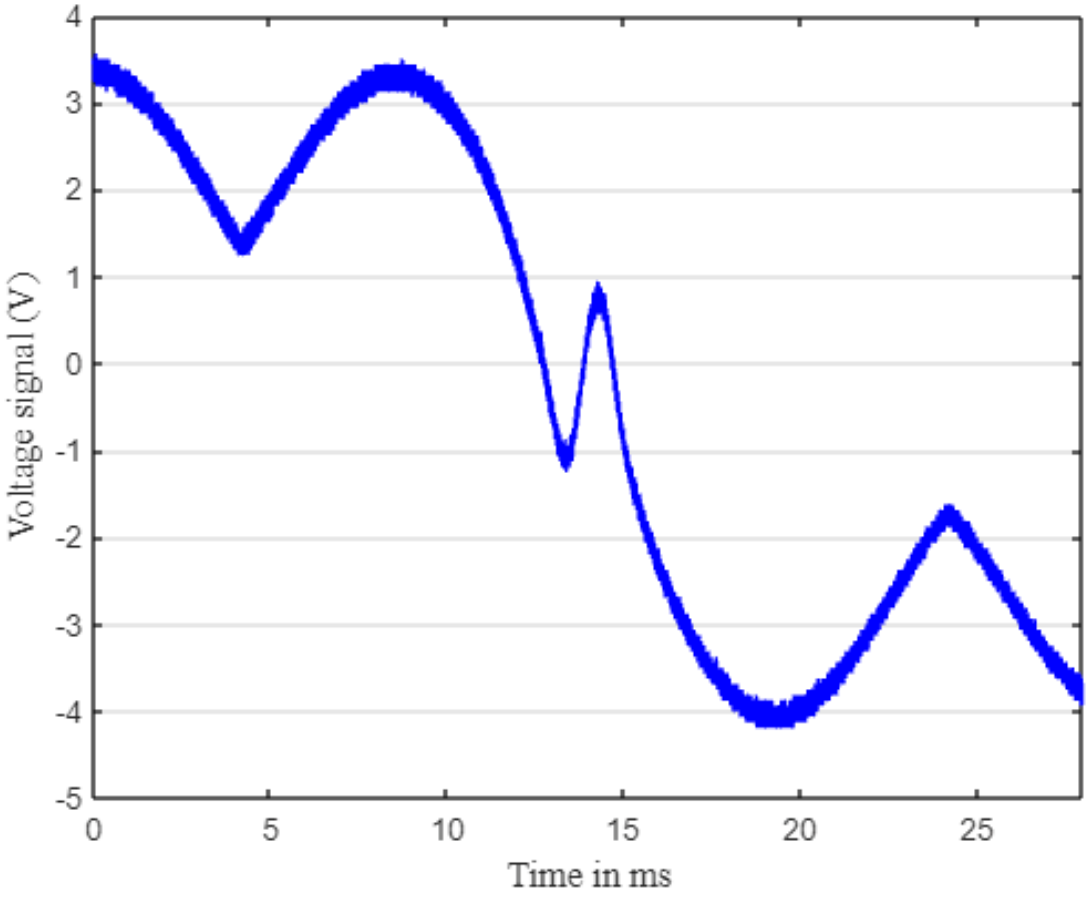


Figure 3.9: Error signal (in blue) generated via saturated absorption on the blue cooling transition. The yellow curve is the TTL at the frequency of the PZT of the ECDL scanning the laser frequency.

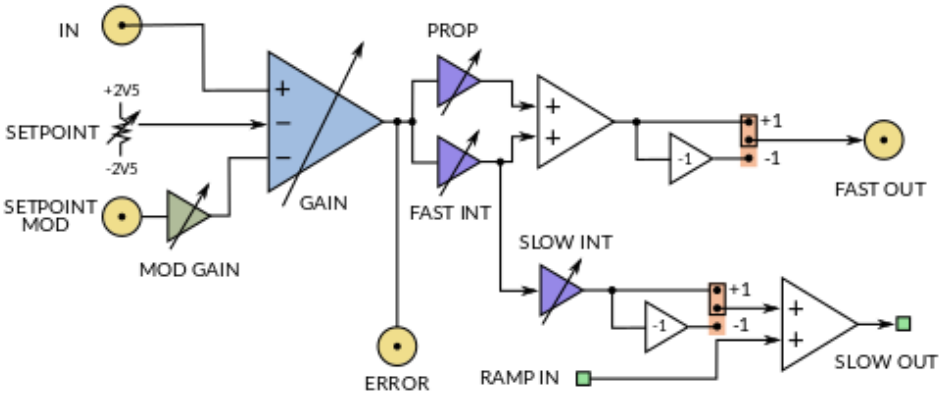


Figure 3.10: Schematic of a PI200 (Koheron). The fast output undergoes a proportional gain and an integration gain in parallel while the slow output is doubly integrated. A set point input is used to optimize the fluorescence of the MOT once the laser is locked [105].

### 3.2.2 Diode injection

Injection locking is a technique used to transfer the optical properties of a weak light field to a more powerful laser source [106]. In a laser cavity, there is a competition among different modes, and the laser cavity tends to select and amplify the mode that is most favored by the properties of the laser diode and the cavity. However, by introducing an external laser field into the cavity, it is possible to impose a particular mode on the laser without significantly affecting the laser's power output. This phenomenon is known as injection locking.

This description provides insights on why the laser current or temperature has to be set precisely as well as how critical is the alignment in this scheme. This method can be implemented to control the optical properties of a laser field up to the hundred of Watts [107].

**Practical realization**

The setup incorporates four optically injected diodes (NDB4916, Nichia): one for the 2D-MOT, one for the 3D-MOT, one for the first Zeeman Slower, and another for the second Zeeman Slower. For a high power blue diode at 500 mW of this type, at least 10 mW of master light must be injected but it is possible to achieve a satisfactory injection with powers down to 1 mW. If the injection power is limited, decreasing the current to optimize the balance between injection power and diode power yields a better injection quality. Typically, the diodes are operated at around 350 mA and maintained at a temperature of approximately 20°C.

Each diode is mounted on a temperature-controlled laser mount (LDM56/M, Thorlabs) and collimated using an aspheric lens (f = 4mm). After collimation, the laser beam passes through a $\lambda/2$ and an optical isolator (I-40T-5H, Isowave) provided with side port for the laser injection from the master laser.

The alignment of the injection beam is performed by overlapping it with the reflection of the NICHIA diode from the viewport of the optical isolator. The quality of the injection is monitored using a scanning Fabry-Perot interferometer (SA200-3B, Thorlabs) with a free spectral range of 1.5 GHz. Initially, a first-order alignment is established to observe a peak on the scanning cavity, but further optimization is necessary. Three parameters can influence the quality of the injection: the temperature of the diode, the current supplied to the diode,

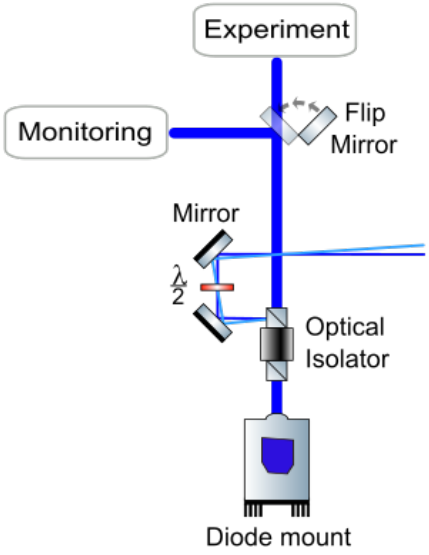


Figure 3.11: Schematic of injection locking. The master laser (DL pro, TOPTICA) has to mode match the beam generated by the diode. The alignment process can be made using the reflection from the optical isolator (light blue). A flip mirror can select either if the beam is analysed by a scanning Fabry-Perot cavity or going to the setup.

and the alignment of the injecting beam. It is generally recommended to set and keep the diode temperature fixed, while the diode current can be scanned to optimize the injection peak. However, if precise control over the current is challenging, the signal can be optimized by scanning the temperature. It is important to note that achieving a good injection may take more time when using the temperature scanning method. In any cases, it is recommended to optimize the alignment before the current (or the temperature). Setting a decent injection with the current will generate many injection peaks, corresponding to the different modes excited by the diode's cavity. An optimized alignment yields a dense spectral profile.

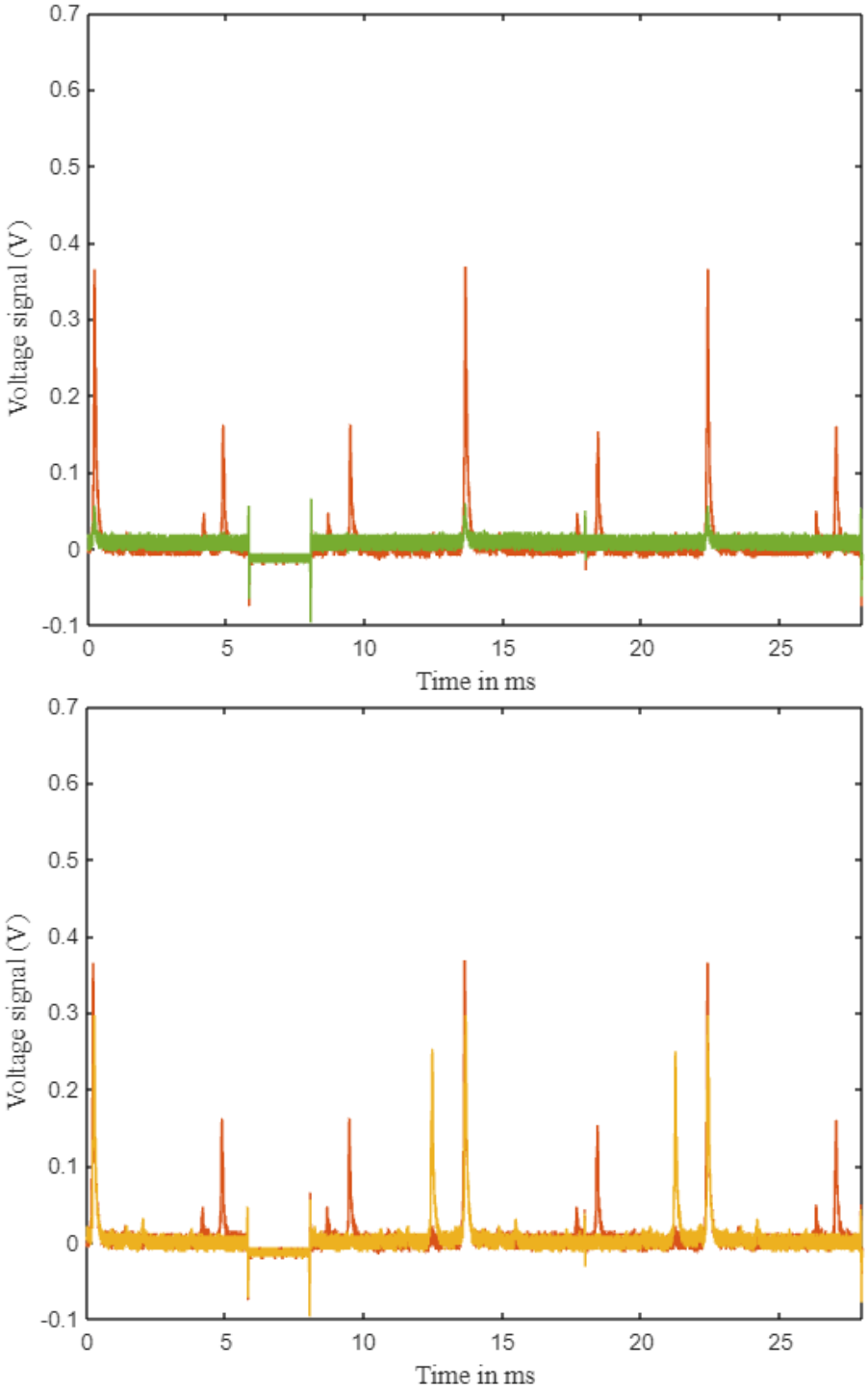


Figure 3.12: Quality of the injection locking monitored via a scanning Fabry-Perot cavity. The green signal (top) shows a poor injection, obtained with a rough alignment of the master laser. By improving the alignment and scanning the current of the diode yields the signal in red (top and bottom). Passing from the red to the yellow signal (bottom) is made only with alignment; even if the mode of interest is lower in the yellow signal, it is better for the quality of the injection to transfer more energy to the other modes at this stage of the process.

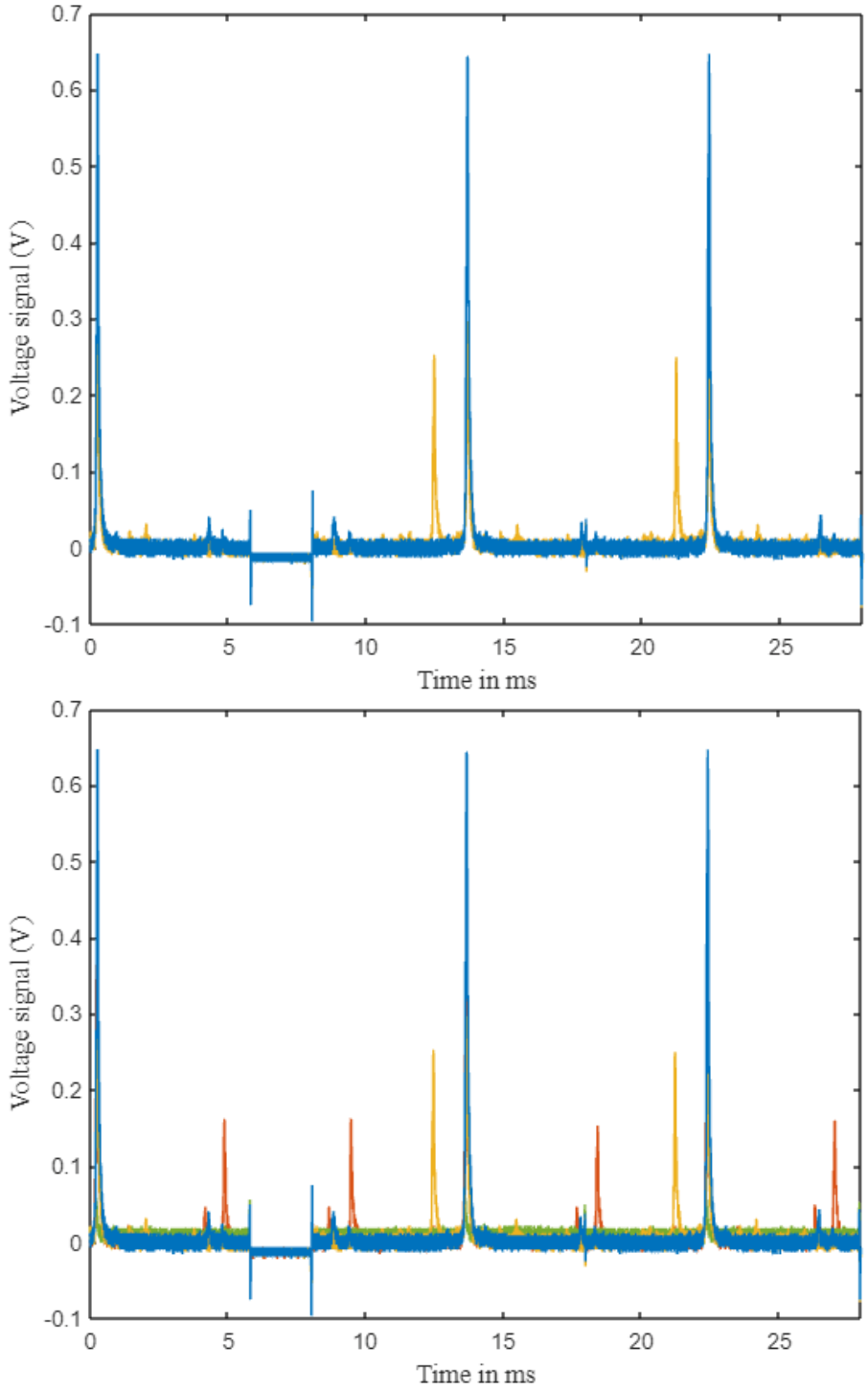


Figure 3.13: Quality of the injection locking monitored via a scanning Fabry-Perot cavity. Once every mode is optimized the alignment can be stopped. Selecting the mode at the frequency of the master laser is then made by scanning the current of the diode. The bottom plot gathers every step of the process.

After optimizing the alignment, the current can be scanned to find the best injection. However, it is important to note that once a certain injection quality is reached by optimizing the current (usually by decreasing it), modifying the current by a tenth of mA is enough to cause the loss of the injection. This phenomenon of threshold exhibits a hysteresis effect. To recover the best injection, the current must be modified by a few mA away from the previously optimized value before gradually approaching it again.

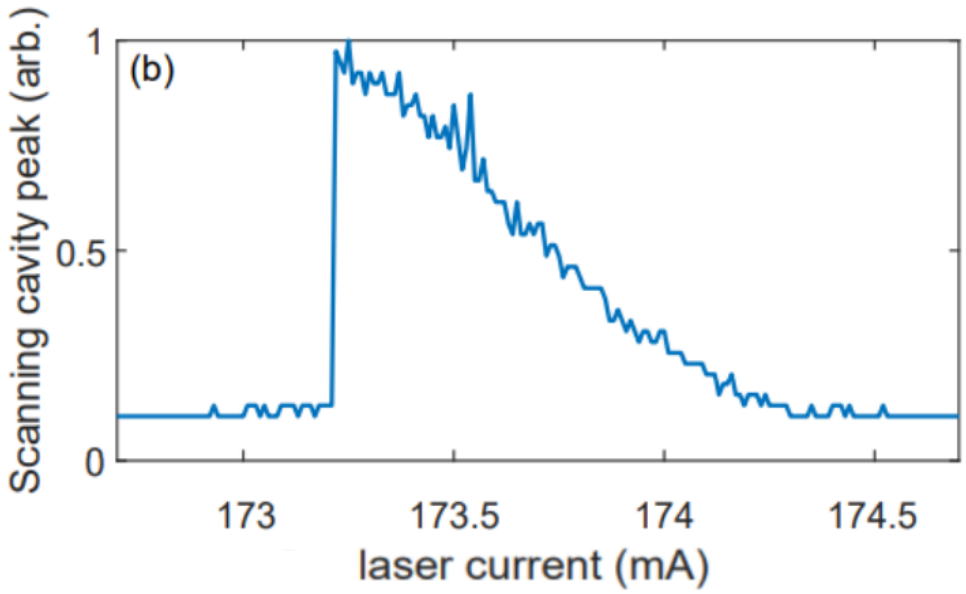


Figure 3.14: Injection efficiency with the diode's current showing the cutoff current at which the injection is lost reducing the current of the injected diode. Credit: [108].

It is possible to servo the diode's current to keep the injection at best but a well injected diode isolated from external perturbations (mainly temperatures fluctuations) can remain locked a few days, rendering this additional work not always necessary.

### 3.2.3 High power blue laser

Frequency doubling a laser field at 922 nm can generate a high-power blue laser beam at 461 nm with a linewidth a the MHz level, i.e. compatible with what required to cool the Sr atoms on the blue cooling transition [109]. This scheme of frequency doubling a laser field at 922 nm circumvents the drawbacks implied by diode injection, allowing both precise control of the laser frequency and avoid injecting multiple diode in parallel.

A tapered amplifier (TA pro, Toptica) amplifies a laser field at 922 nm (DL pro, Toptica), and its output is injected in a resonant Fabry-Perot cavity containing a LBO crystal [110].

Via second harmonic generation, this crystal produces a continuous and single frequency blue laser of 1.05 W at 461 nm starting from 1.19 W at 922 nm, yielding a maximum conversion efficiency of $\epsilon = \frac{P_{\text{out}}}{P_{\text{in}}} = 87\%$.

The phase matching is optimal at 48°C but is also alignment-dependent. The cavity length is servo-controlled using a piezoelectric device, enabling phase matching lock through polarization spectroscopy. This technique converts polarization fluctuations into a voltage error signal [111]. Importantly, this method is modulation-free and enables automatic re-locking of the laser in case of accidental frequency jumps.

If the cavity is locked using polarization spectroscopy, the absolute frequency is locked via the current of the source at 922 nm by beat note locking between the output of the cavity and the master blue laser. A red detuning of 20 MHz with respect to the blue cooling transition has been found to optimize the 3D-MOT fluorescence.

## 3.3 Magnetic field coils

### 3.3.1 3D-MOT coils

To create the necessary magnetic field gradient for both the blue MOT and the red MOT in the science chamber, a rectangular pair of coils is employed. These coils are supplied with a current flowing in two different directions. Each coil is composed of 6x7 turns and has size of 19 cm x 9.8 cm. The resistance of the coil pair is estimated to be approximately 65 m$\Omega$. However, it should be noted that the resistance increases over time due to the heating generated by the 80 A current flowing through the coils during operation.

To go from blue MOT to the red MOT, the current in the coils must be reduced from 80 A to approximately 5 A, in order to change the magnetic field gradient from 50 G/cm to 3 G/cm. This switching can be achieved using the DAC input of the power supply itself. However, if the switching time is longer than the time required for the cloud expansion to leave the cooling region, it may result in a loss of atoms. A scheme involving a Zener diode

can be implemented to reduce the magnetic field slope more quickly [112].

### 3.3.2 External field compensation

In order to compensate for the parasitic magnetic fields, three pairs of square coils are positioned around the science chamber in a Helmholtz configuration. These coils are designed to compensate the Earth's magnetic field, which is identified as the main source of parasitic field. Likewise, the optical table is amagnetic to mitigate the parasitic magnetic fields. The coils are designed to generate a magnetic field strength of approximately 1 G, estimated using a magnetometer.

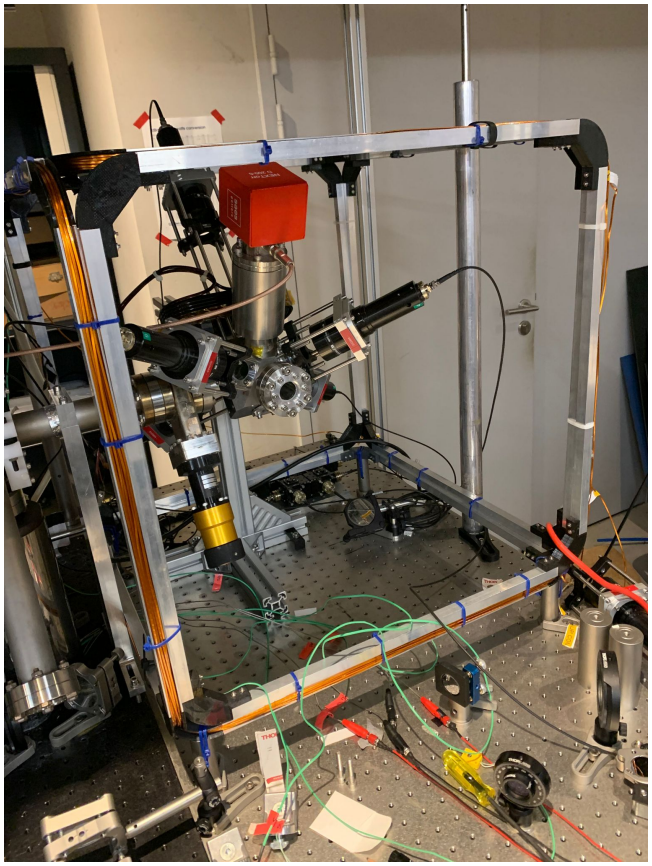

Figure 3.15: Compensation coils are wound around the science chamber to mitigate the effects of external magnetic fields.

To generate a magnetic field strength of approximately 1 G, each of the square coils is wound with 20 turns around square faces of side 55 cm and supplied with a current of around 300 mA.

The resistance of each coil is estimated to be approximately 240 m$\Omega$ and the whole system of compensation coils is supported by posts to properly position the science chamber at the center of the magnetic field generated by the coils.

## 3.4 Clock and cooling laser stabilisation

The red cooling transition has a linewidth of 7.4 kHz. Thus, cooling atoms via this transition requires a laser whose fast fluctuations are at least narrower than this linewidth. Concerning the linewidth of the clock laser, it is dictated by the desired accuracy of the interferometer. For instance, a gravitational wave at 1 Hz necessitates a clock laser with a linewidth below the Hz scale.

Commercials ECDL lasers have typically a linewidth of the order of 100 kHz. Thus, they have to be narrowed before to be used on the atoms. Locking a laser both to the regard of the fast fluctuations (linewidth narrowing) and to the regard of the slow fluctuations (nominal frequency locking) usually involves a double locking scheme, more demanding to implement than a single saturated absorption employed for the blue cooling transition.

### 3.4.1 Linewidth narrowing

The most commonly employed method for narrowing the linewidth of a laser is through the use of a Pound-Drever-Hall (PDH) locking scheme, which takes advantage of the error signal generated by the transfer function of a high finesse cavity. The PDH locking scheme, named after R. V. Pound, Ronald Drever, and John L. Hall, similar to FM spectroscopy, consists of a modulation of the laser frequency and a demodulation in phase quadrature of the reflected signal from the cavity. The resulting error signal, which captures the difference between the laser frequency and the cavity resonance, is then fed into a proportional-integral-derivative (PID) controller. The output of the PID controller is used to adjust the current of the laser diode, effectively narrowing down its linewidth. Locked in a PDH locking scheme, the laser linewidth results to be a fraction $\sim 10^{-4}$ of the cavity linewidth [113].

**Narrowing the red cooling laser**

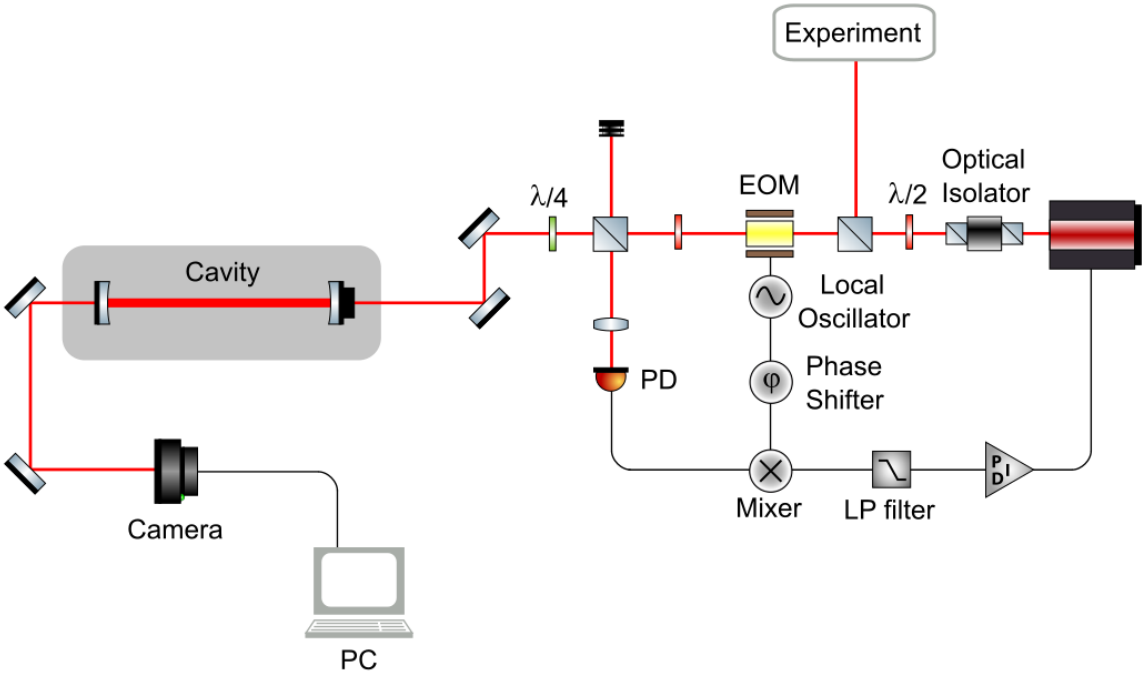


Figure 3.16: Experimental realisation of a PDH locking scheme. The light injected in the cavity is modulated using an Electro-Optic Modulator. The transmission of the cavity is used for monitoring while the reflection is demodulated, sent to a PID and then to the laser actuator to close the servo loop. BS: Beam Splitter, PD: Photo-Diode.

To address a transition with a linewidth of 7 kHz and produce a satisfactory MOT, the linewidth of the laser used should ideally be narrower than or on the same order of magnitude as the transition linewidth. Therefore, a cavity with a linewidth of at most 10 MHz would be suitable. Using a cavity whose free spectral range (FSR) is 1.5 GHz, it yields a finesse of 150 at least.

Modulated at 25.6 MHz via a resonant EOM, the light at 689 nm reflected from a cavity scanned with a PZT (SA200-3B, Thorlabs) is detected using a fast photodiode. The typical PDH error signal is obtained (Figure 3.22) showing the sidebands 25.6 MHz away from the carrier. It is possible to lock a laser to the sidebands, offering another actuator to adjust the nominal frequency of the laser but the piezo-electric transducer (PZT) is used for this purpose in our setup.

The error signal is sent to a PID (PI200, Koheron) whose gain is adjusted monitoring the

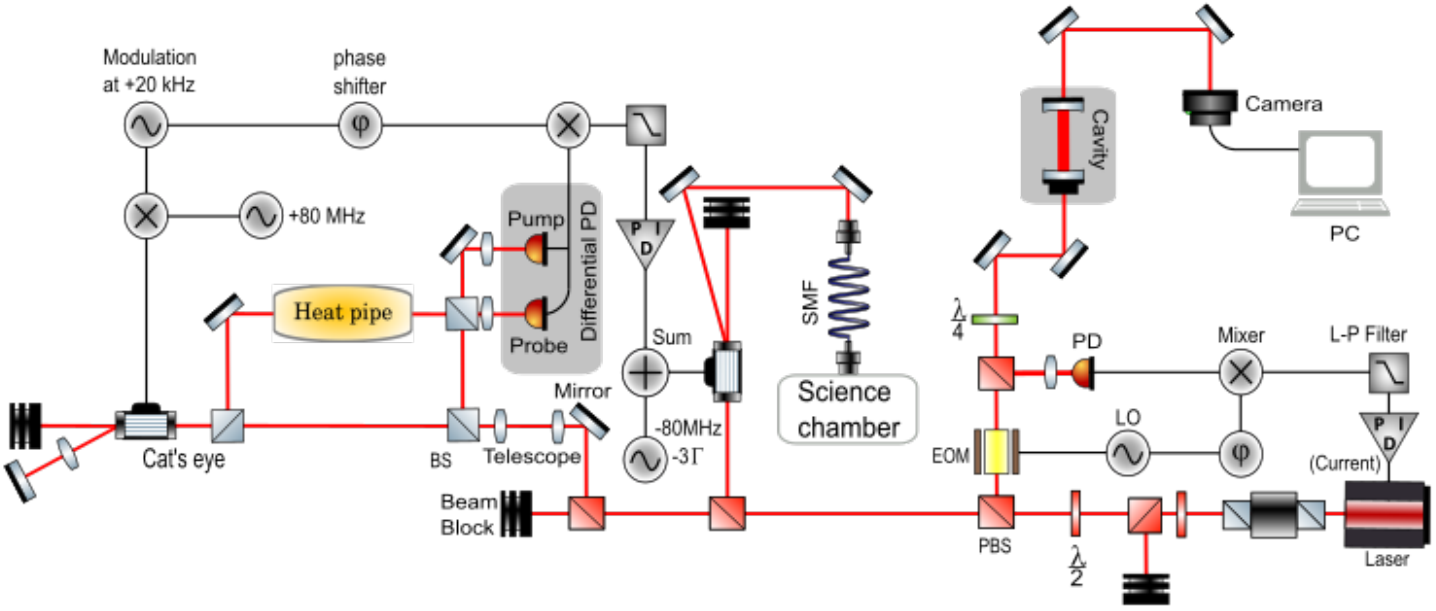


Figure 3.17: Setup relative to the Red cooling transition. EOM: Electro-Optic Modulator, AOM: Acousto-Optic Modulator, PD: Photo-Diode, BS: Beam Splitter, LO: Local Oscillator.

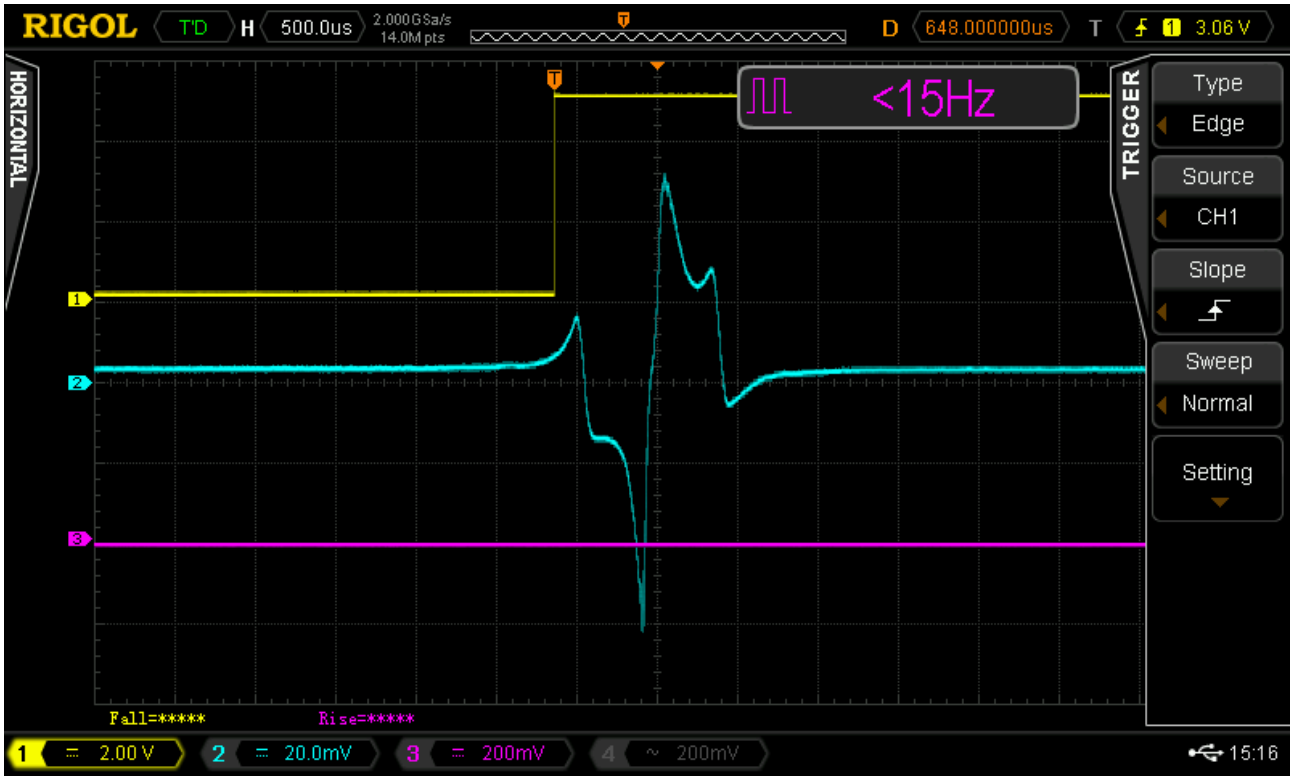


Figure 3.18: Error signal before the PID generated by a Fabry-Perot cavity in a PDH locking. The cavity model is SA200-5B from thorlabs, $\mathcal{F} = 250$ and FSR $= 1.5$ GHz.

cavity output signal. The proportional gain is set to be at its maximum value before inducing oscillations of the error signal. Then, only the PZT of the ECDL is scanned if the laser has to be re-locked. Indeed, working on the setup may disturb the optical or the RF signal, leading to a jump of the laser frequency. Otherwise, under normal operating conditions, the laser stays locked for several weeks.

**Narrowing the clock laser**

A standard cavity is inadequate for narrowing the linewidth of an interferometric laser at the Hz level. The accuracy of the resolved frequency is limited by the linewidth of the clock laser. To mitigate this limitation, a high finesse cavity (ORC-Cylindric, Menlo) with a finesse $\mathcal{F}$ better than 250,000 at 698 nm is utilized to significantly narrow the linewidth of the clock laser. The cavity has a length of 12.1 cm, resulting in an FSR of 1.24 GHz. However, measuring the linewidth is not a straightforward process. The recently installed frequency comb at LP2N will be employed to estimate it.

The locking scheme employed for the clock laser is similar to that of the red cooling laser, with the distinction that the laser is modulated at 20 MHz to be distinguishable from the error signal generated by a modulation of 25.6 MHz for the locking of the laser at 689 nm. The setup's breadboard is directly mounted on the cavity to maximize isolation from mechanical vibrations. The cavity will be later placed on a vibration isolator (Minus K) and shielded to minimize the influence of air fluctuations.

The error signal is sent to a commercial PID controller (FALC Pro, TOPTICA), which adjusts the current of the clock laser to lock it on a peak of the cavity.

### 3.4.2 Absolute frequency reference locking

Locking a laser to a cavity solves the problem of the linewidth but not the one of the absolute frequency. Given that the current of the diode laser is used as actuator in the PDH scheme, it is necessary to use another actuator to servo the nominal frequency.

Given that the red laser at 689 nm is locked to a cavity mounted on a PZT, the cavity length can be stabilized to maintain the nominal frequency at resonance with the atomic transition generated by saturated absorption. The modulation frequency is set at 25 kHz. At

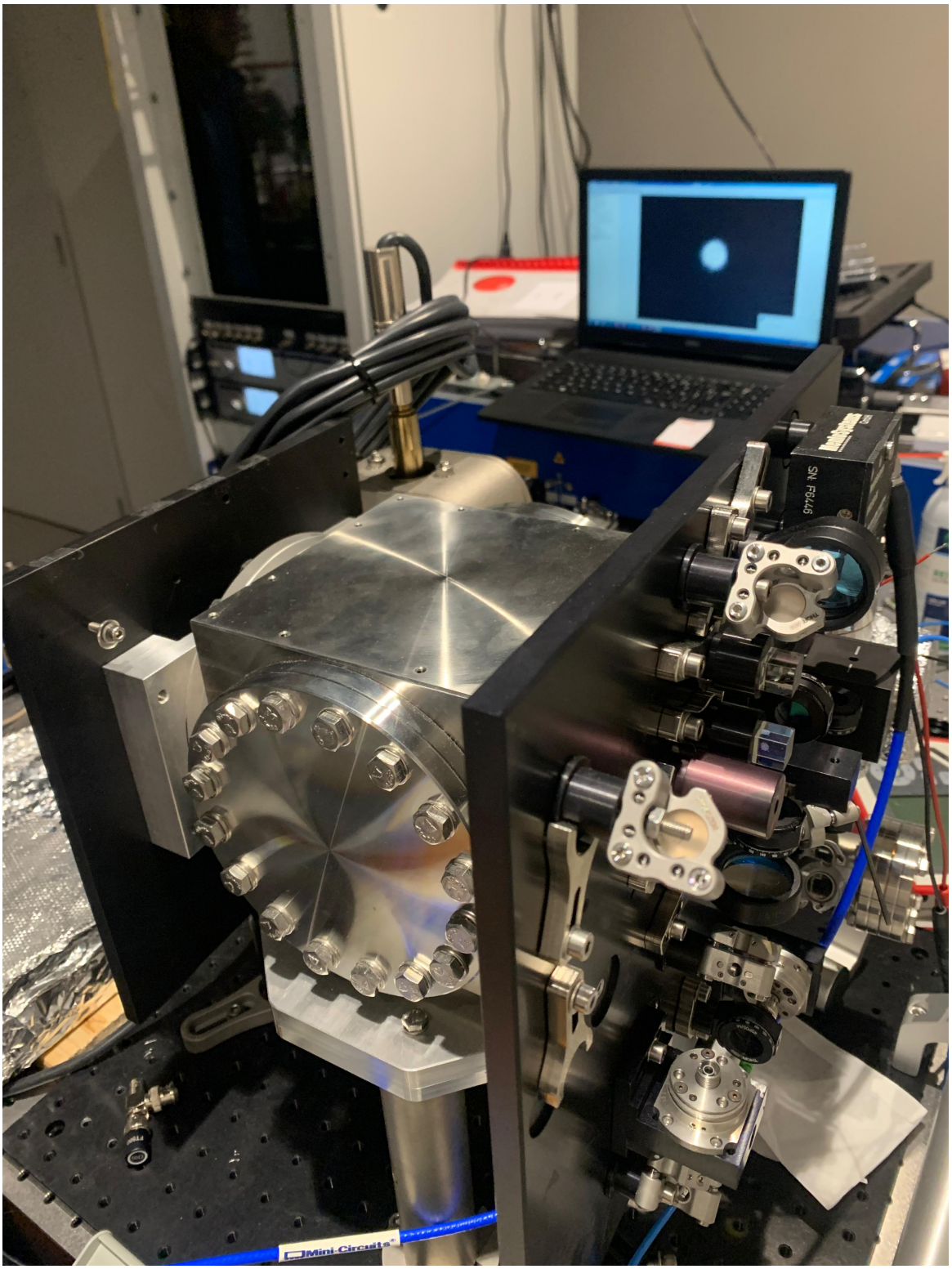


Figure 3.19: High finesse cavity from MenloSystems, $\mathcal{F}$ = 250 000 @ 698 nm. The setup involving the PDH locking scheme is mounted on the cavity to minimize the noise due to vibrations. The cavity transmission is monitored with a CCD camera, and shown on a laptop.

this frequency, it is possible to modulate the RF frequency of an AOM without the limitation by the angular deviation implied by the frequency modification.

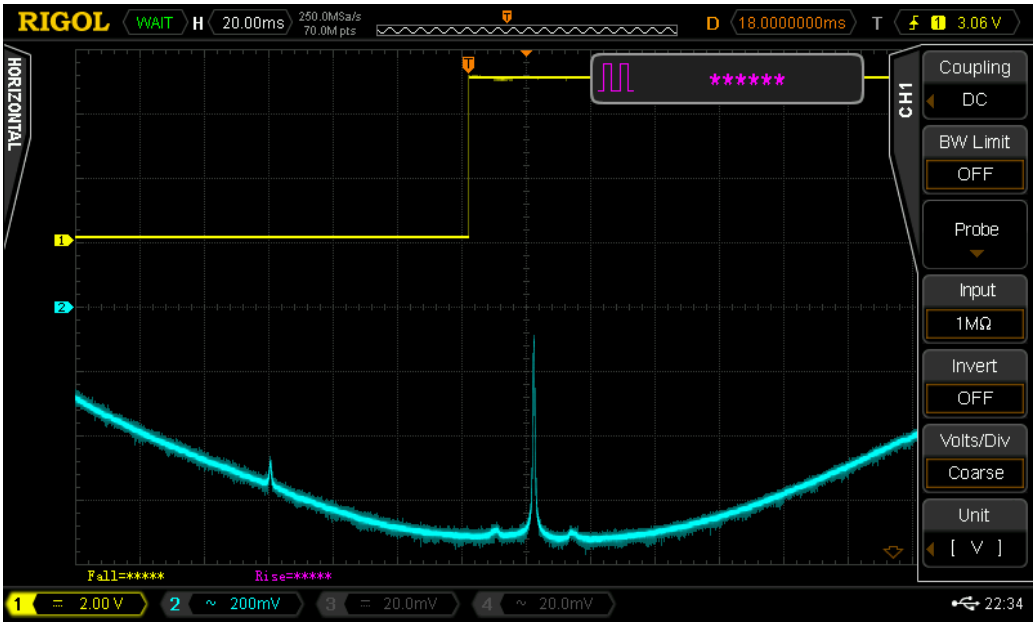


Figure 3.20: Sub-Doppler signal on the red cooling transition detected via a differential photodiode. The central peak and the two smaller sidebands are related to the most abundant isotope $^{88}$Sr while the small one on the left is related the second most abundant isotope $^{86}$Sr.

The pump and the probe beams involved in the saturated absorption are detected in parallel using a free-space balanced amplified photodetectors (PDB210A/M, Thorlabs) and sent to a PID (PI200, Koheron). The generated error signal is sent as an offset to the PZT voltage control driver and the locking efficiency is monitored via the saturated absorption signal.

The stability of the cavity length is rather low, given that one of its mirror is mounted on a PZT to have the possibility to scan the cavity length; as a consequence it is difficult to employ the previous technique for locking the nominal frequency of the laser at 698 nm.

One option is to regulate the cavity temperature, but this approach should be avoided given that the temperature should be fixed at the inversion point where the cavity exhibits the least sensitivity to temperature fluctuations. The sidebands also generate an error signal that could be used to lock the absolute frequency of the laser. In this scheme, the actuator is the EOM.

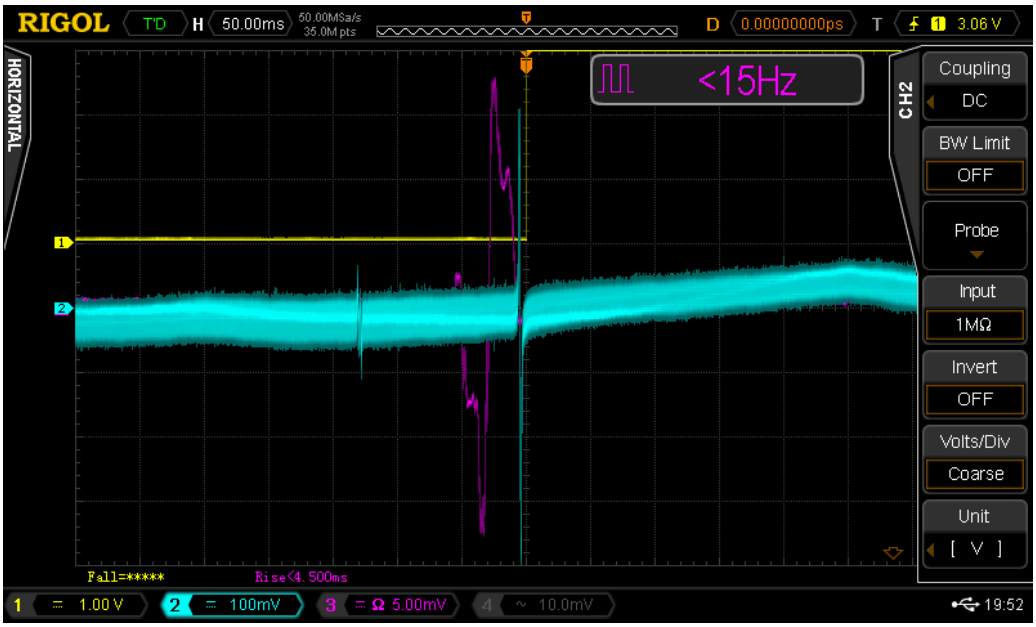


Figure 3.21: Spectroscopic error signal (light blue) generated by modulation of the AOM at 25 kHz before entering the heat pipe in a FM spectroscopy scheme. It has to be adjusted within the carrier of the PDH signal (pink-purple) generated by the reflection of the cavity in order to lock the laser on the sub-Doppler signal. On this figure, it is shifted away from the PDH signal for sack of clarity.

Until now, experiments involving Sr atoms have utilized cavities mounted on PZTs despite the finesse limitation. However, the recent development of commercial frequency combs has provided an alternative solution for precise locking of the nominal frequency without the need to modify the cavity length.

### 3.4.3 Saturated absorption limitations

Using the error signal generated by the saturated absorption to obtain the absolute reference for the red cooling transition, is a critical issue, which requires to take into consideration several measures.

#### Power broadening

The probability for an atom to absorb a photon out of resonance increases with the laser intensity, which is known as power broadening. Specifically, the power broadening effect scales with the square root of the laser intensity

$$\Gamma_{\text{eff}} = \Gamma_{\text{nat}}\sqrt{1 + \frac{I}{I_S}} \tag{3.5}$$

where $\Gamma_{\text{eff}}$ is the effective linewidth, $\Gamma_{\text{nat}}$ the natural one, $I$ the laser intensity and $I_S$ the saturation intensity of the transition [15, 114].

The saturation intensity of the red cooling transition is $I_S = 3\ \mu$W/cm$^2$; using 1 mW/cm$^2$ in the spectroscopic cell broadens the natural linewidth $\Gamma_{nat} = 7.4$ kHz up to $\Gamma_{\text{eff}} = 135$ kHz. Given that the spectroscopic signal is involved in a FM spectroscopy scheme, the accuracy of the nominal frequency servo is way better than the transfer function's linewidth and as a result, at 1 mW/cm$^2$ this broadening is not enough to disturb the locking process. Nevertheless, increasing the laser intensity above the W level could disturb the locking scheme and in practice a compromise has to be found between the signal gain and its enlargement due to power broadening.

**Pressure broadening**

Atoms in a spectroscopic cell exchange energy during collisions; in our heatpipe we must consider Sr-Sr and Sr-Ar interactions. Specifically, atoms can absorb photons that are not resonant with the atomic transition thanks to the energy added via the collisions, resulting in spectral line broadening [115].

Experimentally, the sub-Doppler signal is monitored while pumping the heat pipe and the pressure broadening can be considered negligible around $\sim 10^{-3}$ mbar of buffer gas. If the temperature of the heat pipe can be as low as 350°C for the blue cooling spectroscopy, an optimized signal has been found at ∼450 °C for the red one, implying $\sim 10^{-6}$ mbar of Sr vapor pressure in the heat pipe.

**Time of flight**

The transit time broadening arises as a consequence of the Fourier transform of the interaction time between atoms and a laser beam. When an atom with velocity $v$ is illuminated by a laser beam with a waist diameter $\omega$, the interaction time is limited to $\Delta t = \frac{2\omega}{v}$ at maximum. As a result, a frequency difference of $\Delta\nu = \frac{1}{\Delta t}$ cannot be resolved, which leads to the broadening of the absorption signal.

At a temperature of 450 °C, the most probable atomic velocity is approximately $v = 350$

m/s. To ensure that the atoms are probed at their most probable velocity, a beam diameter of $2w = \frac{v}{\Delta\nu} \sim 5$ cm is required. A rigorous calculus can be found in [116] where the transit time broadening is estimated to be

$$\delta\omega_{\text{tr}} = \sqrt{2\ln 2}\frac{2v}{w} \approx 2.4\frac{v}{w} \tag{3.6}$$

Therefore, the broadening is approximately 30 kHz, negligible compared to the power broadening in our setup but not in a setup where the intensity in the heat pipe is much lower than 1 mW.

**Zeeman levels**

Due to the extremely narrow linewidth of the clock transition and the specific isotope selection, obtaining the saturated absorption signal for the clock laser addressing the $^{87}$Sr isotope, which represents only 7% of the natural abundance, is practically impossible. Consequently, an alternative approach is required to accurately determine the laser frequency and establish a reference for locking its nominal frequency.

One viable solution is to employ a frequency comb, which enables the precise measurement and estimation of the laser frequency.

## 3.5 Locking via a frequency comb

The advancements in laser technology have made it possible to generate ultrashort laser pulses, which are characterized by a duration below the picosecond level. These ultrashort pulses are typically produced using mode-locked oscillators. Mode-locking is a technique that involves constructive interference among all the longitudinal modes of a laser, resulting in a periodic train of laser pulses [117]. By introducing a mechanism that provides higher gain for short pulses, it becomes possible to selectively generate shorter pulses instead of continuous waves. The duration of the pulses is ultimately limited by the excited state's lifetime.

While mode locking is often discussed in the time domain, it is the analysis in the frequency domain that leads to the concept of a frequency comb: a collection of regularly

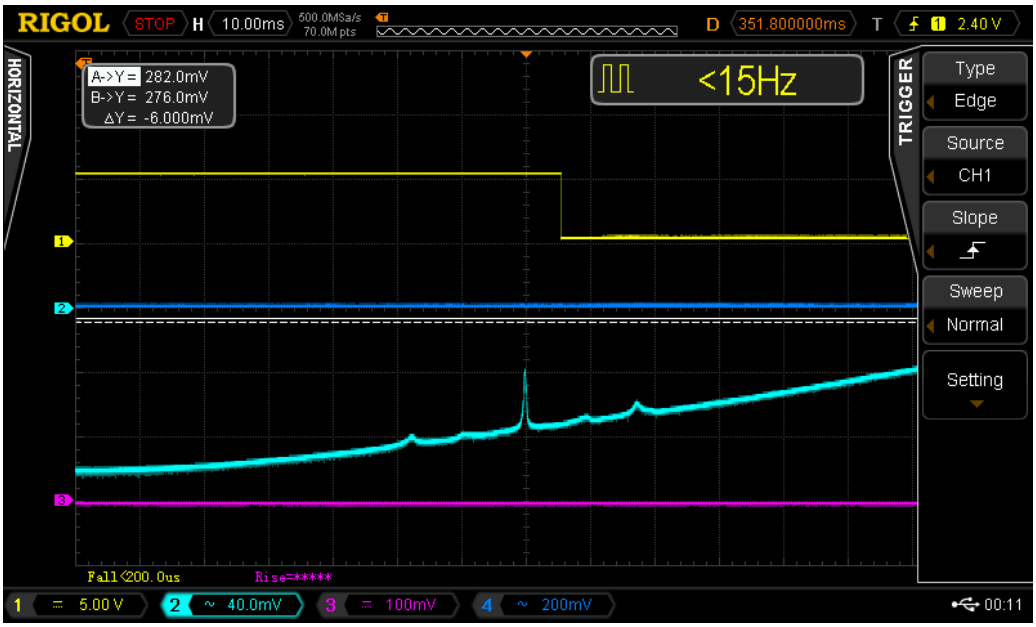


Figure 3.22: Splitting of the $m_J$ levels by adding a DC magnetic field on the saturated absorption spectroscopy.

spaced and sharply defined spectral lines that arise from the properties of ultrashort laser pulses [118].

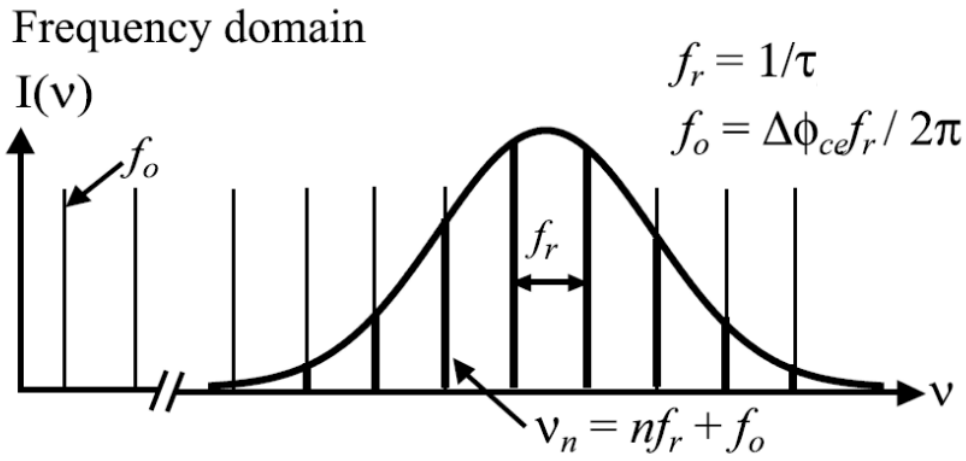


Figure 3.23: Frequency distribution of a frequency comb with respect to the offset $f_0$ and the repetition rate $f_{\text{rep}}$ . Credit: [119].

### 3.5.1 Fundamental principles of frequency combs

When the Fourier transform is applied to a single ultrashort laser pulse, it results in a Gaussian-shaped spectrum centered around the carrier frequency. The width of this Gaussian profile is inversely proportional to the temporal width of the pulse's envelope. However, it is the interference between multiple laser pulses that gives rise to the unique comb structure in the frequency domain.

The Fourier relations dictate that a spectrometer capable of resolving the individual comb lines in the frequency domain cannot simultaneously distinguish the individual pulses in the time domain. Therefore, it is essential to consider the interference between these pulses when analyzing the comb spectrum. The detailed description of this phenomenon can be found in [120].

Let's consider a single pulse as

$$E_p(t) = \hat{E}(t)e^{i(\omega_c t+\phi_{ce})} \tag{3.7}$$

where $\hat{E}(t)$ is the envelope function, $\omega_c$ the carrier angular frequency and $\phi_{ce}$ the carrier-envelope phase of the pulse. Due to the difference between phase velocity and group velocity in the laser cavity, this phase $\phi_{ce}$ evolves between consecutive pulses. Without perturbation of the laser, this shift is constant and is denoted $\Delta\phi_{ce}$.

Considering the time interval $\tau$ between two consecutive pulses and $\phi_0$ the carrier-envelope phase of the first pulse, the laser field can be written as

$$E(t) = \sum_n E_P(t - n\tau) = \sum_n \hat{E}(t - n\tau)e^{i(\omega_c(t-n\tau)+n\Delta\phi_{ce}+\phi_0)} \tag{3.8}$$

Taking the Fourier transform,

$$E(\omega) = \sum_n e^{i(n(\Delta\phi_{ce}-\omega_c\tau)+\phi_0)} \int \hat{E}(t - n\tau)e^{-i(\omega-\omega_c)t} \tag{3.9}$$

After simplifications,

$$E(\omega) = e^{i\phi_0}\tilde{E}(\omega - \omega_c) \sum_n \delta(\Delta\phi_{ce} - \omega\tau - 2\pi n) \tag{3.10}$$

where $\tilde{E}(\omega) = \int \hat{E}(t)e^{-i\omega t}$

This is the frequency comb formula, each tooth occurring for

$$f_n = nf_r + f_0 \tag{3.11}$$

with $f_0 = \frac{1}{2\pi} f_r \Delta\phi_{ce}$ (a minus sign can be added depending on the sign convention) and $f_r = 1/\tau$ repetition rate of the pulses, equal to 250 MHz for the frequency comb we are using.

Consequently, the spacing between the lines in the frequency comb is determined by the time delay $\tau$ between consecutive pulses, while the overall offset of the comb is determined by the phase difference $\Delta\phi_{ce}$ between successive pulses.

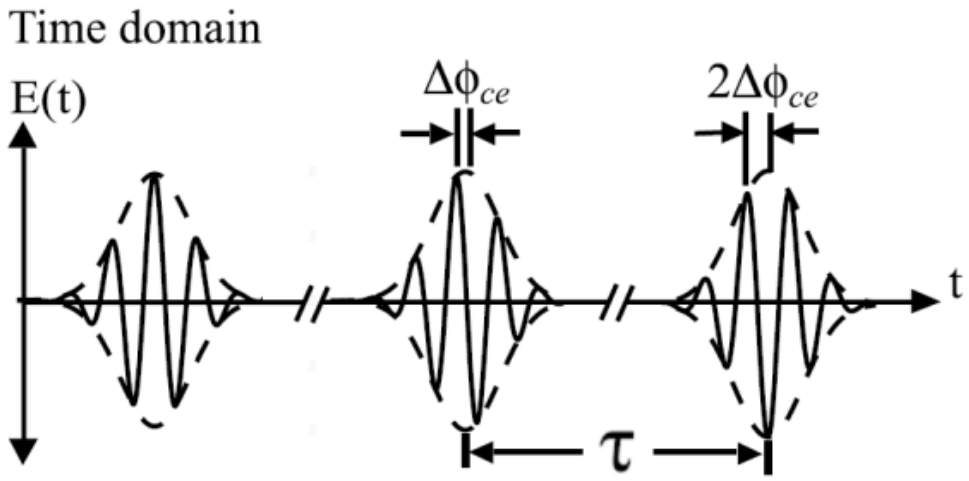


Figure 3.24: Frequency comb in the time domain. $\phi_{ce}$ denotes the phase delay from a pulse to another the time between theses two pulses. Credit: [119].

### 3.5.2 Stability transfer frequency chain

The frequency of a continuous laser field can be determined and servo thanks to its beat note with the frequency comb. With the above notation, and $n$ the number of the nearest comb mode, the frequency of the laser field $f_{cw}$ is linked to the comb properties by

$$f_{cw} = n \cdot f_r \pm f_0 \pm f_{beat} \tag{3.12}$$

where "$\pm$" indicates that the signs of $f_{beat}$ and $f_r$ have to be determine. $n$ is usually a big integer, equal to 1 716 926 in the case of the clock laser at $\lambda$ = 698.44 nm and can be

determined using the relation

$$n = \frac{c}{\lambda f_r} \tag{3.13}$$

Beating with the frequency comb means for the laser to beat with each comb line. Nevertheless, the nearest comb mode yields the lowest beat frequency and can thus be selected using a low-pass filter whose cutoff frequency is around half the repetition rate frequency.

Then, it has to be determined if the laser frequency is above or below the comb line's frequency. This can be done modifying slightly the repetition rate $f_r$ of the comb and analyzing the resulting beat frequency shift. This measurement provides the sign of $f_{beat}$ in equation 3.12.

The sign of $f_0$ also needs to be determined. Although it may be difficult to comprehend how $f_0$ can be negative, it can be understood as the result of interference between two laser fields: one around $2f$ and the other resulting from frequency doubling of a field at $f$ by a second harmonic crystal. Even though a photodiode can only detect the unsigned beat frequency, there is a physical distinction if the second harmonic of $f$ is below or above $2f$, resulting in a different sign for the offset ($f_0$). By modifying the frequency of $|f_0|$ and observing the change in beat note frequency, the sign of $f_0$ can be determined. If the comb moves to higher frequencies, it indicates a positive $f_0$, while if the comb moves to lower frequencies, it indicates a negative $f_0$.

Therefore, every term in 3.12 is known and $f_{cw}$ can be determined. In practice, the beat note detection is performed by overlapping the light from the frequency comb and the laser of interest using a BDU-FF (Beat Detection Unit - Fully Fiber) from MenloSystems.

### 3.5.3 Frequency comb stabilization

Locking a frequency comb results is servo-controlling $f_0$ and $f_r$. The latter is straightforward as the pulses can be detected with a fast photodiode, but measuring $f_0$ is more demanding. Given that the frequency comb spans an octave, it can be measured as mentioned above in a f-2f scheme via interference between a comb line at high frequency and a comb line at a frequency twice lower but doubled using a second harmonic crystal. The heterodyne beat


Figure 3.25: Commercial frequency comb from MenloSystems in white (right) and the associated BDU (left) in blue. Each BDU is designed for a particular wavelength.

yields $f_0$

$$2f_n - f_{2n} = 2(nf_r + f_0) - (2nf_r + f_0) = f_0 \tag{3.14}$$

In practice, the quantities $f_0$ and $f_r$ can be actively controlled and stabilized using various actuators. One common approach is to adjust the length of the laser cavity that generates the pulses. This can be achieved by using a PZT mounted on a mirror within the cavity. By precisely controlling the PZT voltage, the cavity length is modified, leading to a corresponding adjustment in $f_0$ and $f_r$.

Another method involves manipulating the diode current that drives the laser. The nonlinear medium within the cavity converts changes in the laser intensity into phase shifts of the pulses. By adjusting the diode current, the phase of the pulses can be controlled, allowing for fine-tuning of $f_0$ and $f_r$.

The long term fluctuations of the frequency comb can be servo via a GPS signal. Nevertheless, the requirement to compare state of the art optical clocks gave rise to a different method such as the french network REFIMEVE+ [121]. This national network consists of a

laser at 1.55 $\mu$m referenced to the atomic clocks of the SYRTE (Paris) and distributed across the territory via optical fibers. Allan variance versus time implied by this method is two orders of magnitude better than the one implied by GPS signals. Both methods can be used to lock the frequency comb on the long term.

The fast fluctuations of the frequency comb can be servo-controlled using a high finesse cavity. The laser at 698 nm employed to address the clock transition is divided into three optical parts: one part is going to the atoms in the science chamber, another to the high finesse cavity to lock the laser and the last one to the frequency comb. The latter can be used to correct the fast fluctuations of the frequency comb, the finesse of the cavity determining the bandwidth of the servo loop. As a result, the frequency comb becomes a tool to monitor the slow temperature fluctuations that could affect the cavity because they determine the frequency of the laser locked to it.

This system will be used only to characterize the temperature stability of the cavity, then we will adopt a standard configuration, where the comb is lock to GPS or REFIMEVE+ at long term and on the cavity at short term

### 3.5.4 Temperature Stabilization of a Fabry-Perot cavity

The high finesse cavity, manufactured by MenloSystems, is installed in a vacuum system at a pressure of approximately $10^{-9}$ mbar through a pumping system. The cavity's length is carefully controlled and maintained by utilizing a bar of glass made from Ultra-Low Expansion (ULE) material. It has two different features: firstly, a very low thermal expansion coefficient in general; secondly, an inversion point where this coefficient changes sign. At that position the dependence of the piece length from the temperature vanishes. For our cavity that point is between 27 and 27.5 °C. The cavity (spacer + mirrors) is installed in a stainless steel block, which is thermalized thanks to a NTC resistance as temperature sensor and a 4$\Omega$ Peltier element as actuator.

The Peltier is controlled by an H-Bridge configuration that allows it to be operated in either cooler or heater mode, depending on the required temperature adjustments. It is controlled by an Arduino microcontroller mounted on a 160 mm x 100 mm Euro card housed in a rack

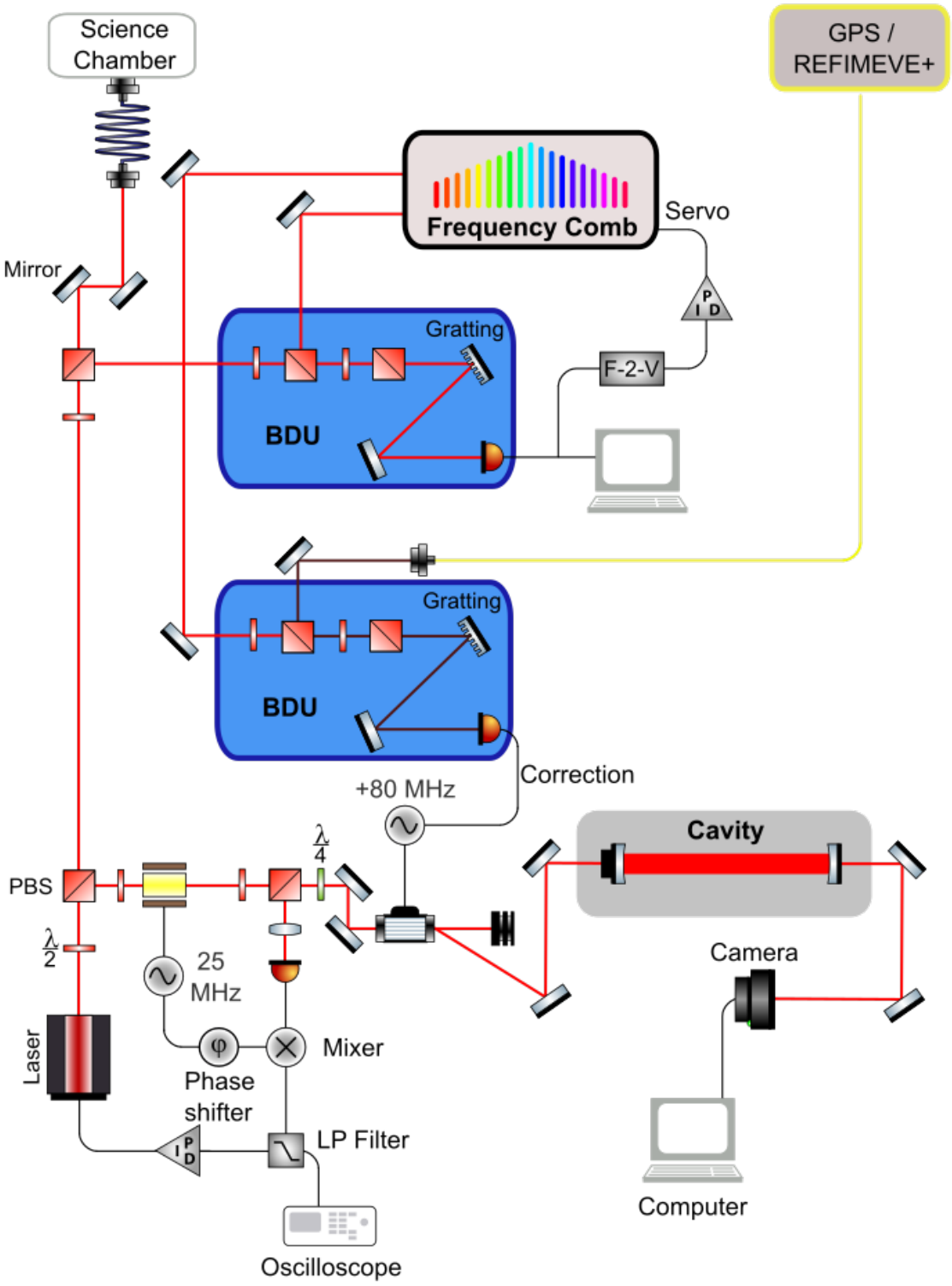


Figure 3.26: Scheme of the three paths taken by the clock laser at 698 nm: One goes to the atoms, another to the frequency comb and the last one to the cavity. The light going to the cavity is employed to lock the laser while the beat note between the laser and REFIMEVE+ (or GPS) stabilizes its long term drift.

which controls a power driver for the Peltier.

The temperature measurement of the cavity is performed using two Epcos B57703M103G40 NTC thermistors, each with a resistance of 10 kΩ. These thermistors can be connected in parallel for averaging the temperature measurement, interfaced with the Arduino for temperature control and sensing. In practice, we only read one channel.

To read the temperature of a NTC thermistor, a voltage reference chip generates a stable voltage of 2.5 V. This reference voltage is connected to one end of a reference resistor, $R_{ref}$, which has a value of 10 kΩ. The other end of the reference resistor is connected to the thermistor via a cable with sub-D 15-pin connectors from Thorlabs.

The voltage across the thermistor, denoted as $V_{therm}$, is measured with a 24 bits Analog-to-Digital Converter (ADC) connected to the Arduino. The ADC reads the ratio $\frac{V_{therm}}{V_{ref}}$ and by analyzing it, the Arduino can determine the temperature of the cavity based on the characteristic temperature-resistance relationship of the NTC thermistor.

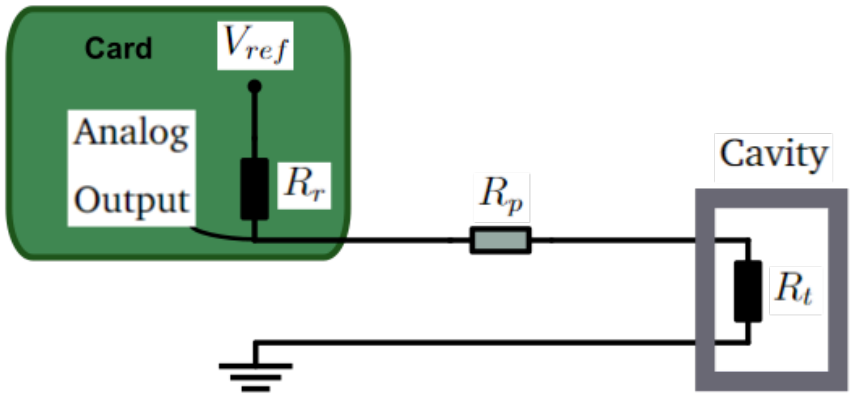


Figure 3.27: Schematic of temperature monitoring via an NTC thermistor. Knowing the dependence of the NTC from temperature, the voltage across the resistance of reference gives the temperature of the cavity. $V_{ref}$ = 2.5 V denoted the voltage of reference, $R_r$ the value of the resistance of reference, $R_p$ the one of the parasitic resistance inside the cable and $R_t$ the one of the thermistor.

The Arduino also implements a digital PID that has been tuned regarding the pulse response of the cavity temperature. Indeed, applying a short-duration pulse input to the system and measuring its output response gives insights on the PID parameters that have to be ap-

plied.

The optimum working temperature is the one at the inversion point. There, the laser servo-loop is the most precise and any measurement should be taken at this temperature of the cavity. For the specific cavity employed, the optimum working temperature is around 27°C.

The ADC connecting the Arduino to the cavity has a rms noise of 0.7 ppm in 160 ms according to the datasheet. Averaged over six measurements every second, it yields an rms noise of 700 nV. Given that the sensitivity of the H-bridge is of ∼22000 ppm/C°, the rms noise of the ADC should be around 13 $\mu$K. The rms we measure is consistent with the expectation, just a factor 2.5 bigger. To take full advantage of this resolution, thermal drifts have to be minimized. Two sources of noise will be discussed and corrected in this work.

### 3.5.5 Differential measurement of temperature fluctuations

The first source of noise is the variation of resistance in the cables between the card and the NTC thermistor due to thermal fluctuations. The resistance of a cable is of the order of $1\Omega$ and the resistivity of copper is of the order of $0.4\%/C°$, inducing both an offset and a thermal drift with the room's temperature.

Let's denote $R_t$, $R_p$ and $R_r$ respectively the resistance of the NTC thermistor, the parasitic resistance and the resistance of reference. We introduce the quantities $\eta = \dfrac{R_t}{R_r + R_t} \approx 0.5$ and $\eta_p = \dfrac{R_t}{R_r + R_t} \approx 10^{-4}$. Therefore, at the first order in $\eta_p$, taking into account the parasitic resistance the ADC reads the quantity

$$\eta_1 = \frac{R_t + R_p}{R_t + R_p + R_r} = \frac{\eta + \eta_p}{1 + \eta_p} = \eta + (1 - \eta)\eta_p + O(\eta_p^2) \tag{3.15}$$

Having two thermistors, the end of the second line is short-circuited so that it yields a circuit with the same resistance of reference and the same parasitic resistance as the first line but without the thermistor. Therefore, assuming that the thermal noise is identical in both cables, it can be corrected in the first line. The quantity read by the second ADC is

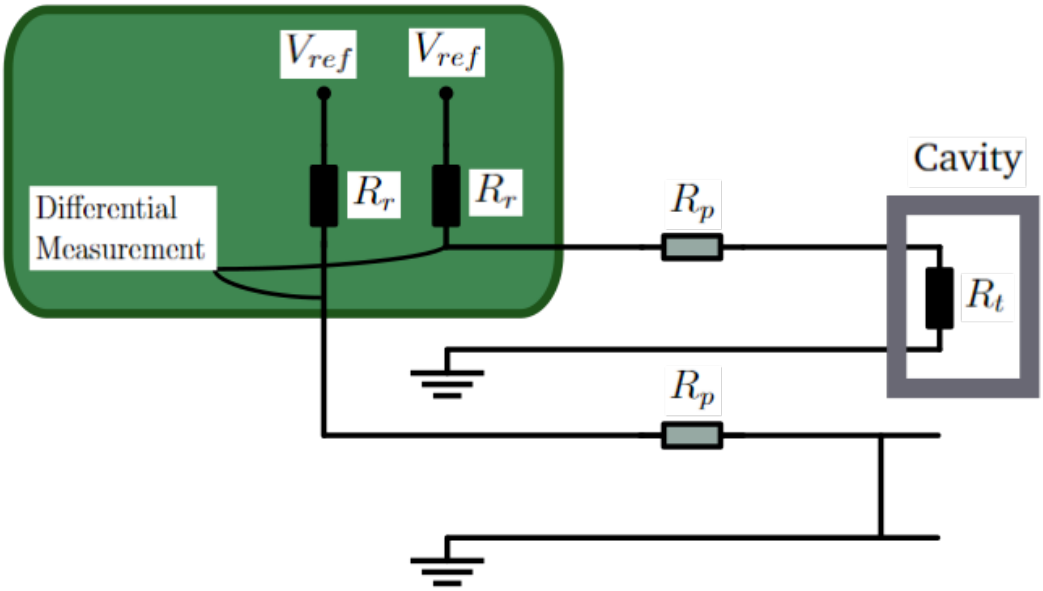


Figure 3.28: A circuit similar to figure 3.27 is implemented based on the same card but short at the end and the voltage difference between the two lines is analysed to cancel $R_p$, the parasitic resistance in the cables.

$$\eta_2 = \frac{R_p}{R_p + R_r} = \frac{R_p}{R_p + R_r + R_t - R_t} = \frac{\eta_p}{1 - \eta + \eta_p} = \frac{\eta_p}{1 - \eta} + O(\eta_p^2) \tag{3.16}$$

As a result, the quantity that should be read by the ADC without parasitic resistance $\eta$ can be determine from $\eta_1$ and $\eta_2$

$$\eta = \eta_1 - \eta_2(1 - \eta_1)^2 \tag{3.17}$$

Enabling or not the correction while applying a ramp of temperature on the cables of both lines should produce a behavior visible on the frequency comb, proving the efficiency of the correction.

### 3.5.6 Measurement of readout fluctuations with the card temperature

The second source of noise is due to the temperature fluctuations of the card in the rack. The resistance of $R_{ref}$ mounted on the card drifts with temperature which modifies the voltage read by the ADC. The datasheet provides a value of $\pm 10$ ppm/C° for the temperature

coefficient of the resistance, which is a mean measurement between two limit temperatures. Removing the cable and replacing it by a resistance with very low temperature coefficient, 0.2 ppm/°C, the real curve can be obtained applying a ramp of temperature on the card and measuring the output of the ADC. The temperature of the card is read by an auxiliary sensor mounted on it.

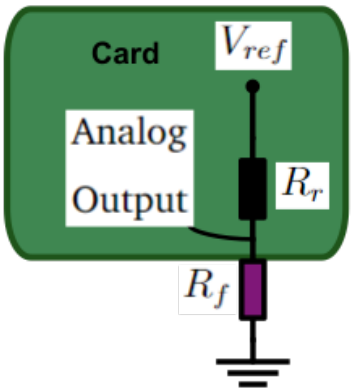


Figure 3.29: The readout error is characterised replacing the cables by a resistance $R_f$ whose temperature dependency is stable: 10 kΩ ± 0.2 ppm/°C (Vishay, Y145310K0000T9L). A function linking the temperature of the card and the readout error can be established and used to compensate it in the setup reading the cavity temperature.

Given the ADC output variations with temperature in this scheme, it is possible to build a lookup table (LUT) or a symbolic function that provides the correction to apply given the temperature read by the auxiliary sensor: $\sim -1.5 \times 10^{-4}$.

Finally, the efficiency of the correction is monitored with the frequency comb while applying a ramp of temperature on the card. Comparing the case where the correction is adopted with the case where it is not yields a measurement of the correction's efficiency.

This experiment and the previous one on the differential measurement of temperature fluctuations are conducted as this manuscript is written.

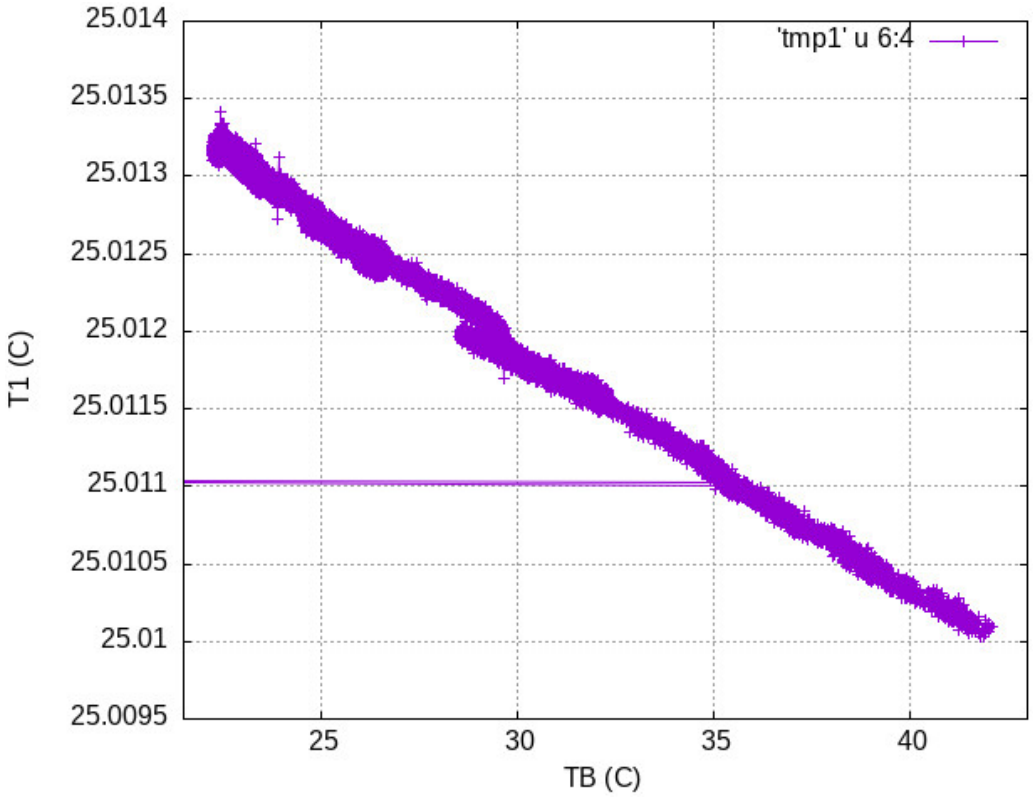


Figure 3.30: Function linking the temperature of the board (TB) to the temperature from readout (T1) taken between the resistance of reference and the stable resistance.

# Chapter 4

# Compact and High Flux Strontium Atom Source

In the field of Atomic, Molecular, and Optical physics (AMO), particularly within the domain of atomic interferometry, a notable emphasis is placed on the utilization of cold atomic ensembles characterized by a substantial atom number represented as N. This emphasis stems from the fact that in such scenarios, a crucial limiting factor is the quantum projection noise (QPN) [122], which imposes a constraint on the achievable phase resolution. This limitation is proportional to $1/\sqrt{N}$, highlighting the critical importance of attaining cold atomic clouds comprising a significant population of atoms.

By establishing a magnetic field configuration for the 2D-MOT as outlined in the preceding chapter, novel forms of Zeeman Slowers can be devised. These advancements facilitate the realization of a consistent atom number confinement within a MOT, all within the confines of a compact experimental setup.

A theoretical exposition of the Zeeman Slower's fundamental principles is provided in Section 4.1. This section encompasses a mathematical elucidation of the underlying effect, as well as an exploration of the sources employed for generating the requisite magnetic field. In Section 4.2, a novel Zeeman Slower scheme is introduced and examined, employing the apparatus outlined in our experimental setup. This section delves into the rationale behind parameter selection, delimitations, and a presentation of measurement outcomes. Building upon the preceding section, Section 4.3 showcases an upgraded iteration of the Zeeman

Slower and provides an analysis of the associated experimental outcomes. Concluding the analysis, Section 4.4 undertakes a discussion of observed limitations, along with a discourse on prospective enhancements to circumvent them. Additionally, the final section addresses the suitability of alternative alkaline-earth-like candidates for similar Zeeman Slower implementations.

---

## Contents

## 4.1 Zeeman Slower principle

### 4.1.1 The Zeeman effect

The Zeeman effect is a phenomenon in which a spectral line is shifted under the influence of a magnetic field, resulting in a change in energy levels. This effect is named after the scientist who first observed it but has been predicted by Lorentz in its classical form. The Hamiltonian of the system can be written as a sum of the unperturbed Hamiltonian and the perturbation Hamiltonian due to the Zeeman effect. The latter is given by the dot product of the magnetic moment of the atom and the magnetic field, denoted by $\vec{\mu}$ and $\vec{B}$, respectively. In other words, the Hamiltonian can be written as:

$$H = H_0 + V_Z, \tag{4.1}$$

where $H_0$ is the unperturbed Hamiltonian, and $V_Z$ is the perturbation Hamiltonian due to the Zeeman effect.

$$V_Z = -\vec{\mu} \cdot \vec{B} \tag{4.2}$$

The atomic magnetic moment consists of two components: the electronic magnetic moment and the nuclear magnetic moment. However, since the nuclear magnetic moment is much smaller than the electronic magnetic moment, it is typically neglected. Thus, the total magnetic moment of an atom can be expressed as:

$$\vec{\mu} = -\frac{\mu_B(g_l\vec{L} + g_s\vec{S})}{\hbar} \tag{4.3}$$

where $\mu_B$ is the Bohr magneton, $g_l$ and $g_s$ are the Landé factors associated with the orbital angular momentum $\vec{L}$ and the spin angular momentum $\vec{S}$, respectively. Under approximation, $g_l = 1$ and $g_s = 2$.

If the magnetic field is weak enough not to decouple $\vec{L}$ and $\vec{S}$, the average spin projected

along $\vec{J}$ is then

$$\vec{S}_{avg} = \frac{(\vec{S} \cdot \vec{J})}{J^2} \vec{J} \tag{4.4}$$

and

$$\vec{L}_{avg} = \frac{(\vec{L} \cdot \vec{J})}{J^2} \vec{J} \tag{4.5}$$

Projected onto the energy space, $V_Z$ becomes $\Delta E$ and using $\vec{L} = \vec{J} - \vec{S}$ equation 4.3 yields [123]

$$\Delta E = \mu_B m_j \left(1 + \frac{j(j+1) + s(s+1) - l(l-1)}{2j(j+1)}\right) B \tag{4.6}$$

Let's introduce g, the Landé factor as [124]

$$g = 1 + \frac{j(j+1) + s(s+1) - l(l-1)}{2j(j+1)} \tag{4.7}$$

Then, equation 4.6 yields

$$\Delta E = \mu_B m_j g B \tag{4.8}$$

The expression in Equation 4.8 is valid for weak magnetic fields that do not decouple the spins. However, if the magnetic field is strong enough, the angular momenta $\vec{L}$ and $\vec{S}$ precess independently about $\vec{B}$, and the formula is no longer valid. This phenomenon is known as the Paschen-Back effect.

In practical settings, it is uncommon for a magnetic field to be sufficiently weak such that the decoupling between $\vec{L}$ and $\vec{S}$ is perfect. However, in this scenario, equation 4.8 remains valid to the first order, but a state possessing $m_j = 0$ experiences a slight deviation to the second order. In the context of a Zeeman Slower, the typical transition occurs between a ground state at $m_j = 0$ and an excited state at $m_j \neq 0$. Consequently, this effect can be ignored.

In addition, for transitions between singlet states, the Landé factor $g$ is equal to 1, simplifying equation 4.8 to

$$\Delta E = \mu_B m_j B \tag{4.9}$$

which is referred to as the "Normal Zeeman Effect". In contrast, equation 4.8 corresponds to the "Anomalous Zeeman Effect".

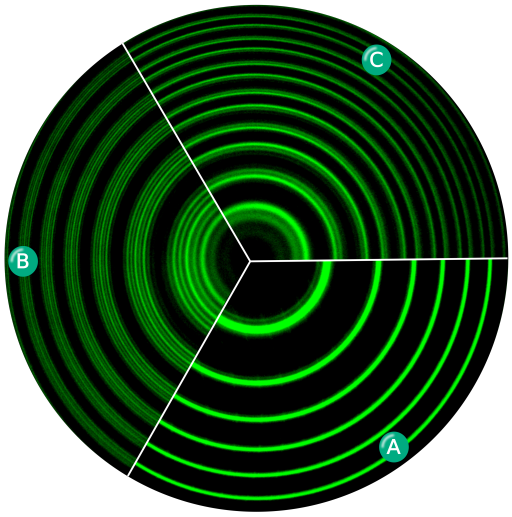


Figure 4.1: Spectral structure of $^{198}$Hg at 546 nm using a Fabry-Perot interferometer [125]. Three configurations of magnetic field are presented; A: No magnetic field; B: Magnetic field applied perpendicularly to the direction of the light; C: Magnetic field parallel to the direction of the light.

### 4.1.2 Theory of Zeeman Slowing

A Zeeman Slower is a tool employed in atomic physics to reduce the velocity of a hot atomic beam along a specific direction. William D. Phillips and Harold Metcalf proposed the first Zeeman Slower in 1982, which utilized the yellow D line of Na [13]. The Zeeman Slower integrates the effects of radiation pressure, Doppler effect, and Zeeman effect to achieve its objective.

#### Radiation pressure

The Zeeman Slower operates on the same principle as a Magneto-Optical Trap (MOT), but along a single orientation. As a result it does not trap but only slows down. When an atom absorbs a photon from a counter-propagating laser beam, it experiences a momentum change of $\hbar k$, resulting in deceleration. In this context, $k$ refers to the norm of the laser field's wave vector. The atom can then re-emit the photon in a random direction via spontaneous emission and return to the ground state, allowing it to absorb another photon and continue the cycle.

The spontaneous emission induced by the Zeeman beam does not heat the atom along the direction of the beam, as its direction of emission is random. However, it does cause

transverse heating [126]. The force experienced by an atom in a Zeeman Slower is given by

$$F_{ZS} = \frac{\hbar\vec{k}\Gamma}{2}\frac{s}{1+s+\left(\frac{2\delta_{ZS}}{\Gamma}\right)^2} \tag{4.10}$$

This expression depends on the effective laser detuning $\delta_{ZS}$, the saturation parameter $s = \frac{I}{I_s}$, and the natural linewidth of the atomic transition $\Gamma$.

Thereby, this force increases with $s$ and when $\delta$ approaches zero. The maximal deceleration is then

$$a_{max} = \frac{F_{max}}{m} = \hbar k\frac{\Gamma}{2m} \tag{4.11}$$

where $m$ is the atomic mass.

Another proof of this formula can be found in section 4.3.3.

**Doppler shift**

Tuning the laser at the transition frequency results in a Zeeman Slower probing the atoms at rest in the frame of the lab. To address the atoms moving towards the Zeeman Slower beam, the laser has to be frequency shifted to match the atomic Doppler shift. Accounting for the Doppler shift, the detuning can be expressed using the laser detuning at rest $\delta_0$ as

$$\delta_D = \delta_0 - \vec{k}\cdot\vec{v} \tag{4.12}$$

where $\vec{v}$ denotes the atomic velocity.

When an atom is perfectly at resonance and absorbs a photon ($\delta_0 = 0$), it is decelerated and experiences a different detuning due to the Doppler effect at each cycle. As a result, the slowing force becomes less effective over greater distances of propagation. Specifically, the absorption of one photon causes a Doppler shift of

$$\Delta\delta_D = k\Delta v = k\frac{h}{m\lambda}, \tag{4.13}$$

where $\lambda$ is the wavelength of the laser field.

For Rubidium atoms on the D2 transition at 780 nm, absorption of one photon results in a deceleration of approximately $5.9$ mm/s and a Doppler shift of $2\pi \times 7.5$ kHz. Similarly, for strontium atoms on the blue cooling transition at 461 nm, absorption of one photon corresponds to a deceleration of approximately $9.8$ mm/s and a Doppler shift of $2\pi \times 21$ kHz. To counteract this Doppler shift, the Zeeman effect is employed.

**Zeeman effect**

In order to maintain the effective detuning closest to zero, a magnetic field gradient is applied to shift the atomic levels via the Zeeman effect, counteracting the Doppler shift induced by each photon absorption. This results in an effective detuning given by

$$\delta_{ZS} = \delta_0 - \vec{k} \cdot \vec{v} + \frac{\mu_B m_j g B}{\hbar} \tag{4.14}$$

Equation 4.8 is used in the Zeeman shift term. It should be noted that this formula is valid only when the laser polarization is adjusted to interrogate a $\sigma$ transition. In our model, a $\pi$ transition is not sensitive to the Zeeman effect ($m_j = 0$).

Consider an atom with an initial velocity of $v_0$ at the output of the oven, and assume the origin of distances is taken at this point. Under a constant deceleration of magnitude $a = -|a|$, the velocity of the atom evolves as

$$v(t) = -|a|t + v_0$$

and the position evolves as

$$z(t) = -\frac{1}{2}|a|t^2 + v_0 t$$

Solving for $z(t)$ and substituting it back into the expression for $v(t)$ yields the velocity as a function of distance:

$$v(t) = \sqrt{v_0^2 - 2|a|z(t)}. \tag{4.15}$$

Let $k$ and $\theta_B$ be defined such that $\vec{k} \cdot \vec{v} = kv\cos\theta_B$ and $\alpha_j = \frac{\mu_B m_j g}{\hbar}$, respectively. As the deceleration is maximal for $\delta_{ZS} = 0$, we obtain an expression for $B$ as a function of the velocity $v$:

$$B = \frac{kv\cos\theta_B - \delta_0}{\alpha_j} \tag{4.16}$$

The appropriate magnetic field profile for the velocity class $v_0$ is then

$$B(z) = \frac{\vec{k} \cdot \vec{v_0}\sqrt{1 - \frac{2|a|z}{v_0^2}} - \delta_0}{\alpha_j} \tag{4.17}$$

where $\vec{k} \cdot \vec{v_0} = kv_0\cos\theta$.

In the original paper of 1982, Philips and Metcalf wrote this relation as

$$B = B_b + B_0 \left( \sqrt{1 - \frac{2az}{v_0^2}} \right)$$

The constant bias field $B_b$ is employed to avoid optical pumping of a state experiencing no Zeeman effect.

Atoms with velocities lower than $v_0$ will be affected by the designed magnetic field and undergo deceleration. However, the deceleration process will start further away from the output of the oven, where the magnetic field matches their Doppler profile. On the other hand, atoms with velocities higher than $v_0$ will not experience deceleration by the Zeeman Slower due to the mismatch between their Doppler profile and the magnetic field.

### 4.1.3 Magnetic field sources for Zeeman Slowing

#### Using electromagnets

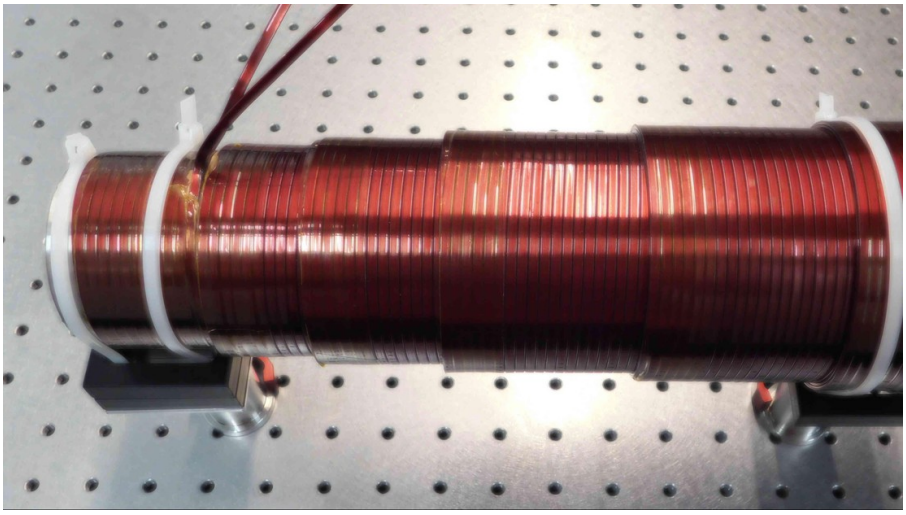

Figure 4.2: A Zeeman Slower constructed by winding multiple layers of electrical wire. Picture from the Laboratory for Quantum Gases, EPFL.

Since the first demonstration in 1982 by Phillips *et al.*. [13], most Zeeman Slower setups have relied on electromagnets to generate the required magnetic field gradient. In these designs, a solenoid is wrapped around the vacuum tube containing the atom beam to generate the Zeeman effect, with additional coils added as the atoms approach the oven to create the necessary magnetic field gradient.

It should be noted that in this configuration, the magnetic field is co-linear with the atomic beam, meaning that any optical polarization of the Zeeman Slower beam will interrogate a $\sigma$ transition, which is necessary for the Zeeman Slower to work.

One of the major drawbacks of this approach is that it requires a bulky setup. strontium atoms need to be heated to approximately 550-600°C in most experiments [96], resulting in a broad atomic velocity distribution and necessitating a large electromagnet. Additionally, such a Zeeman Slower design is complex and energy-intensive.

**Using permanent magnets**

A new configuration to trap atoms effused from an oven and bring them in a second UHV chamber has been introduced in [127]: there, a 2D MOT obtained with permanent magnets is transversely loaded with the low velocity tail of the thermal distribution coming from the oven. In this experiment, a source of up to $10^{10}$ $^6$Li atoms is side loaded by an oven in a 2D-MOT whose magnetic field is generated by two stacks of permanent magnets.

A first improvement has been proposed by Lamporesi *et al.* in 2013 [97]. A Zeeman Slower for sodium is implemented benefiting from the magnetic field generated by the permanent magnets far from the 2D MOT region.

In 2017, Nosske *et al.* improved that scheme to produce a Zeeman Slower on strontium using four stacks of permanent magnets [96]. This setup offers a loading rate of $10^9$ atoms/s with an oven operating at a lower temperature of 500°C compared to conventional methods. In addition, this work proposes two regions to implement the Zeeman Slower: the rising slope of the magnetic field and the descending one.

Furthermore, in addition to the problems mentioned before, this compact setup addresses or mitigates the issues associated with vacuum contamination and black-body radiation originating from the oven [128, 129]. Indeed, the science chamber (3D-MOT chamber) is loaded from a jet of cold atoms (the 2D-MOT) orthogonal to the thermal beam originating from the oven. Therefore, there is no line of sight of the hot oven region

Specifically, the placement of two pairs of permanent magnets around the 2D MOT chamber generates the required magnetic field gradient. As such, this approach offers a practical and effective alternative to the traditional electromagnet-based cooling methods [96, 97].

In our setup, the external magnetic field gradients present outside the 2D-MOT chamber

is utilized to implement a Zeeman Slower (see Figure 4.3), thereby eliminating the need for additional components in the setup. Notably, in contrast to the Zeeman Slower involving coils, the direction of the magnetic field is perpendicular to the velocity of the atoms. Consequently, depending on the polarization of the beam employed for the Zeeman Slower, either a $\pi$ transition, a $\sigma$ transition or both transitions will be addressed (in this latter case, half of the power of the laser beam is dedicated to each transition). Hence, the polarization must be meticulously adjusted.

## 4.2 Enhanced single frequency Zeeman Slower

To decelerate the atomic flux emitted by the oven, the Zeeman Slower beam is directed through the sapphire window positioned opposite the oven with respect to the zero magnetic field as shown in Figure 4.3.

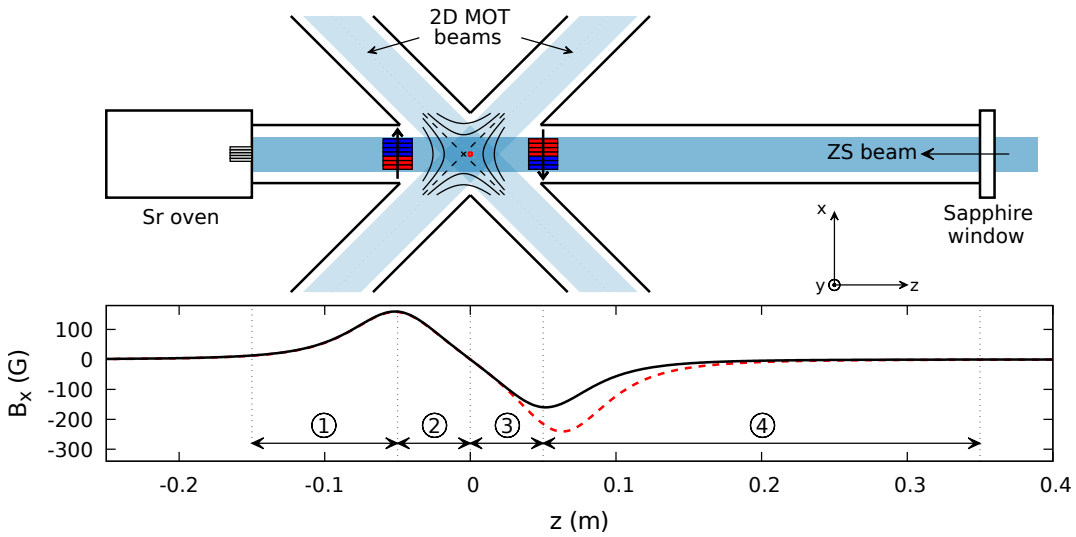


Figure 4.3: Top: schematic of the setup utilizing permanents magnets both for the magnetic field of the MOT and for Zeeman slowing. The 2D-MOT is located at 15 cm of the oven (left) and at 35 cm of the sapphire window (right) used for the entrance of the Zeeman Slower beam. Bottom: magnetic field generated by the permanent magnets. The red dotted line denotes the magnetic field modified for Zeeman slowing improvement.

The stacks of permanent magnets produce a magnetic field that can be divided into four regions, as represented in Figure 4.3: ① between the oven and the magnet stacks at negative

z, ② between the magnet stacks at negative z and the 2D-MOT, ③ between the 2D-MOT and the magnet stacks at positive z and finally ④ between the magnet at positive z and the sapphire window.

If previous work considered alternatively region ① or region ② to build a Zeeman Slower [96], our group aimed to slow down atoms by using simultaneously different regions for the atomic deceleration, so as to optimize the process. Indeed,extending the distance over which the atom are decelerated increases the maximum atomic velocity that can be brought within the capture range of the 2D-MOT, thus giving a higher cold atomic flux

### 4.2.1 Choice of the frequency

The velocity distribution, integrated over a solid angle, of the thermal atomic beam effused by the oven follows a Maxwell–Boltzmann distribution [130]. The most probable velocity is given by

$$f(v) = \left(\frac{m}{2\pi k_B T}\right)^{3/2} 4\pi v^2 \exp\left(-\frac{mv^2}{2k_B T}\right) \tag{4.18}$$

with $f(v)$ the probability density function to find an atom at the velocity $v$ in one direction, $m$ the atomic mass, $k_B$ the Boltzmann constant and $T$ the cloud temperature. At the temperature of 550°C that we use for our oven, this most probable velocity is approximately 400 m/s. For velocities below this peak value, the number of atoms per unit velocity increases with the velocity.

Until now, a laser used to slow down the atoms effused by the oven has been considered to address only region ① or ②. However, as shown in Figure 4.5, a laser with a large enough detuning from the atomic resonance and containing both $\sigma^+$ and $\sigma^-$ polarizations addresses two adjacent velocity classes

In Figure 4.5, two output atomic beams are produced but on opposite sides of the 2D-MOT. An optimized detuning is reached when the red output beam is slowly reaching the 2D-MOT trapping region from the negative side, whereas the blue output beam does not hit the sapphire window, inverts the trajectory thanks to far off resonance scattering and then falls back to the 2D MOT as illustrated in blue in Figure 4.7.

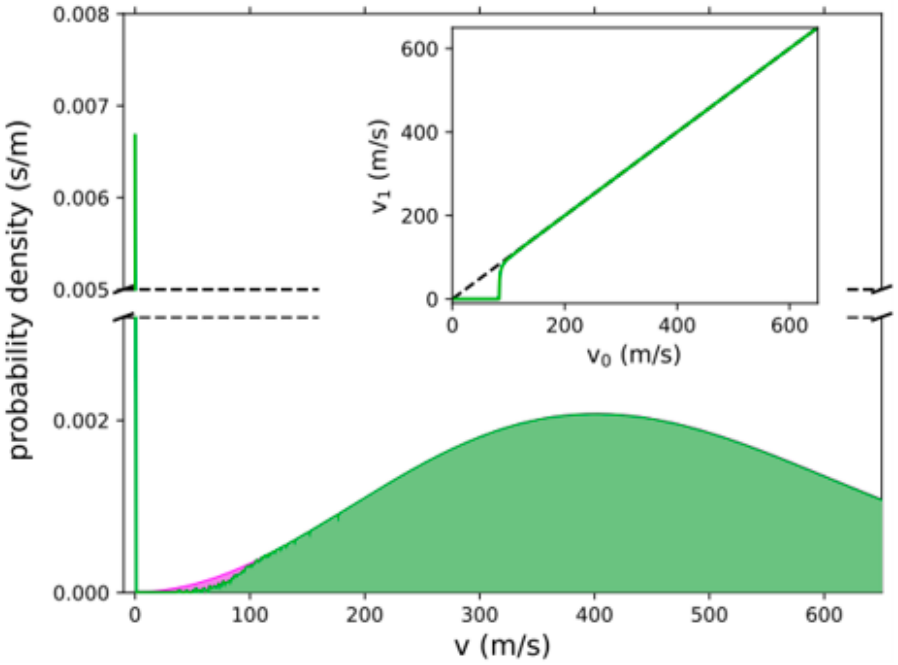


Figure 4.4: Probability density versus velocity of atoms emitted by the oven at 550°C (pink), and when the 2D MOT is operating (green).

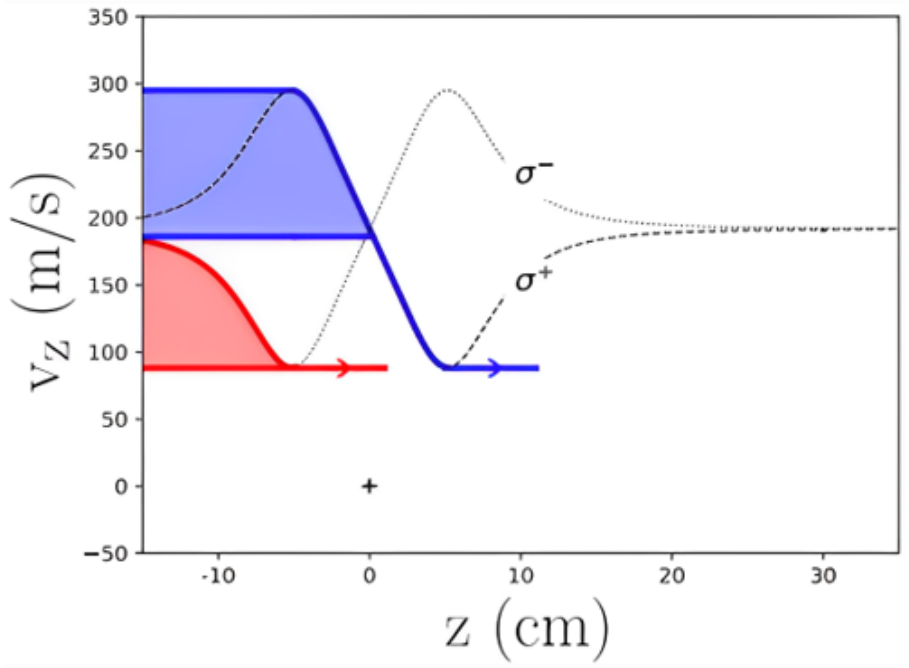


Figure 4.5: Velocity class versus position. The MOT position is represented by a cross at the origin, the fastest velocity classes captured by the Zeeman Slower in blue, the slowest in red and the atomic velocity resonant with each cooling beam polarization in black dotted/dashed.

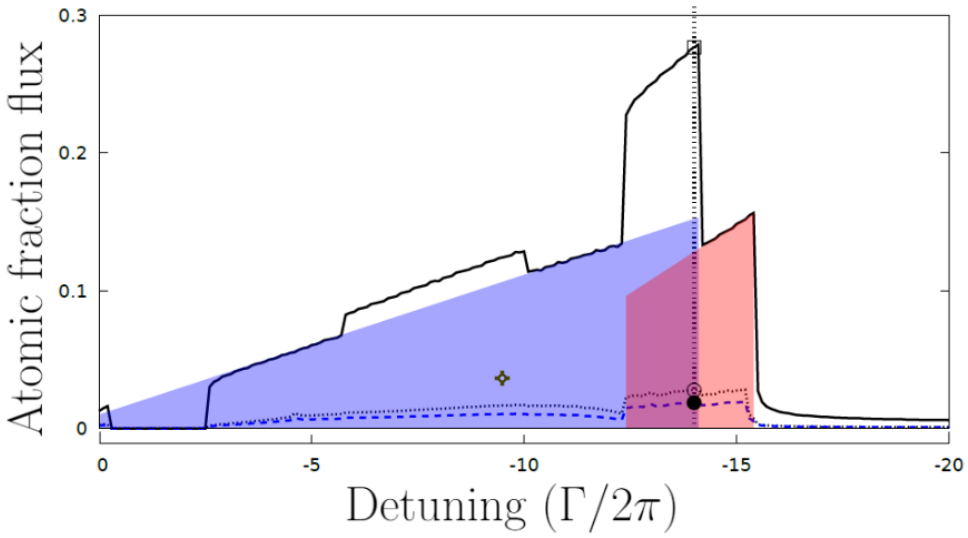


Figure 4.6: Capture efficiency of a single Zeeman Slower. The fraction of atomic flux captured by the 2D-MOT is calculated as a function of the detuning of the Zeeman Slower beam. In solid line, the fraction of atomic flux calculated considering a problem in one dimension where the atomic trajectories have three output: to be pushed back toward the oven, to be captured by the 2D-MOT and to end up on the sapphire window. In dotted black, the same simulation but having introduced the losses caused by the expansion of the atomic cloud and in dashed blue the losses caused by the cloud expansion together with the radiative loss. The surfaces in blue and in red highlight the contributions of the $\sigma^+$ transition and the $\sigma^-$ transition respectively.

To have both $\sigma^+$ and $\sigma^-$ polarization on the atoms, the magnetic field's orientation must be linear and orthogonal to the optical polarization of the Zeeman Slower beam. In such a configuration, the linear polarization can be decomposed into two circular polarizations, the right-handed circular polarization interacting with the atoms on the $\sigma^+$ transition and the left-handed circular polarization interacting with the atoms on the $\sigma^-$ transition. As a result, only half of the overall power of the Zeeman Slower beam is dedicated to the interaction with each type of transition.

This scheme already goes beyond what has been demonstrated so far, using simultaneously more than on region.

As represented in Figure 4.7, a Zeeman Slower shifted by -14 $\Gamma/(2\pi)$ with respect to the blue cooling transition slows down atoms in regions ①, ② and ③.

The $\sigma^+$ polarization decelerate atoms in regions ② and ③ to produce a slow atomic beam after having passed through the 2D-MOT region. As they are to fast to be trapped, these

slow atoms are travelling in region ④ and undergo deceleration via radiation pressure to be ultimately pushed back to the 2D-MOT. In the most optimized configuration, the atoms reach their inversion point (position where the atoms are motionless on the z axis) just before the sapphire window.

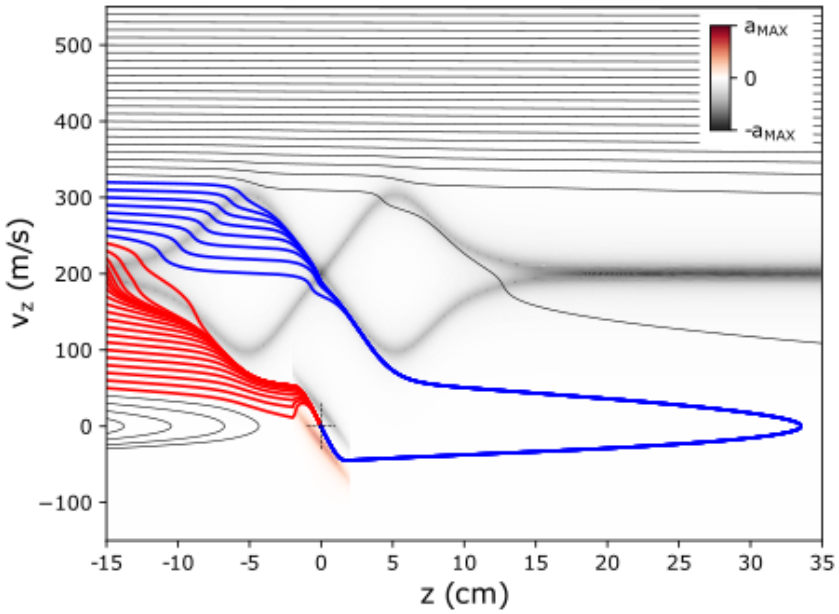


Figure 4.7: Action of a single Zeeman Slower at -14 Γ and s = 1.4 on each velocity class and for each position. At this detuning, the atoms are travelling during 29 ms in a long trajectory nearly reaching the sapphire window.

This configuration would trap atoms up to 320 m/s at the output of the oven, corresponding to 27.6% of the Maxwell Boltzmann distribution. For the sake of comparison, the 2D-MOT without Zeeman Slower traps 0.41% of the Maxwell Boltzmann distribution.

### 4.2.2 Cloud expansion model

The previous description of the cloud evolution is made only along the z axis, axis along which are aligned the oven, the 2D-MOT and the sapphire window. An accurate model of the situation should take into account the cloud expansion in the transversal plan (x-y).

Indeed, each atom leaving the oven does not follow the same orientation. With the distance, the cloud is expanding in the transversal plan. This effect induces important limitations to the Zeeman Slower's efficiency and is taken into account in the simulation.

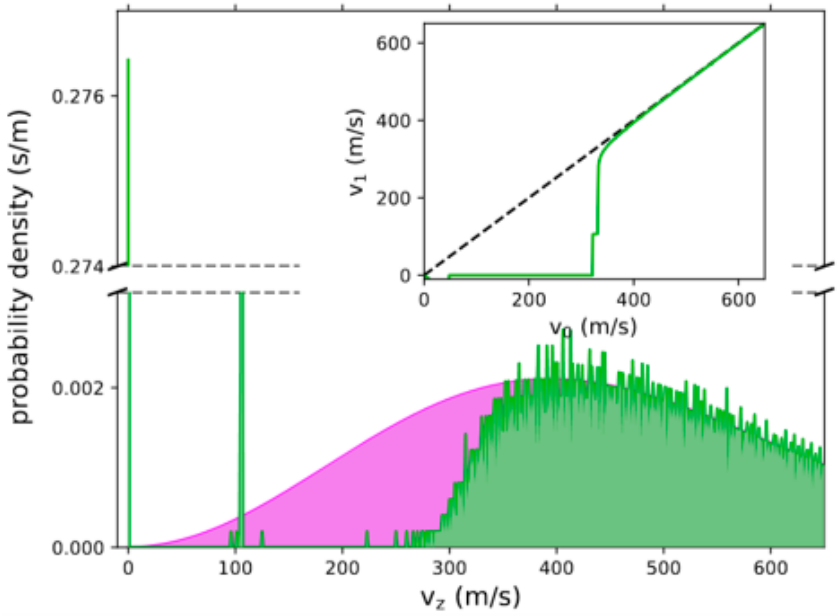


Figure 4.8: Probability density versus velocity of atoms emitted by the oven at 550°C (pink), and when both the Zeeman Slower and the 2D MOT are operating (green). Such configuration traps theoretically 27.6% of the atoms.

**Transverse heating**

An atom undergoing a Zeeman Slower absorbs an re-emits $N$ photons while slowing down from a velocity $v_i$ to a velocity $v_f$ according to the formula

$$N = \frac{\Delta v}{v_{rec}} \tag{4.19}$$

where $\Delta v = v_i - v_f$ and $v_{rec}$ denotes the recoil velocity.

During the phenomenon of spontaneous emission, the direction of emission of the photon is random. Therefore, each photon scattered by an atom during the slowing process has a probability of inducing a movement of the atom in the transverse plane.

From equation 4.19 can be derived the transverse RMS velocity for a given transition as a function of the number of photons absorbed [126]

$$(v_{\perp}^{RMS})^2 = \alpha \frac{v_{rec}^2}{3} N \tag{4.20}$$

where $\alpha = \frac{9}{10}$ is a term due to the dipole pattern.

For a $^{88}$Sr atom cooled down via the blue cooling transition along 10 cm from 200 m/s to 50 m/s, this RMS transverse velocity corresponds to $v_{\perp}^{RMS} = 75$ cm/s for $N = 21\,400$ cycles. Assuming a mean velocity of 150 m/s, it means a cloud expansion of 0.7 mm in average, thus

much less than the beam diameter. Therefore, this effect will be neglected in our model of the cloud expansion.

**Transversal velocity distribution**

Let's consider an oven with a circular slit of diameter $a$, placed at a distance $L$ from a second slit of diameter $a$ as well employed to collimate the atomic beam.

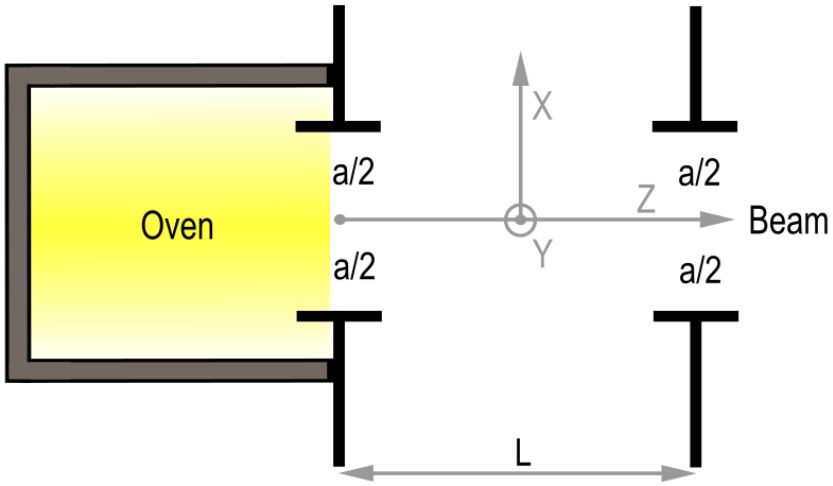


Figure 4.9: Schematic of the symmetric collimating slits at the output of the oven.

In our setup, micro-tubes are used to collimate the atomic beam along a distance of 9 mm with a slit diameter of 0.4 mm. This configuration has been proven to be preferable to the pinhole configuration where all the atoms are leaving the oven from a unique point [98].

In polar coordinates, the probability density function at a position $y$ to find an atom at the velocity $v$ with an angle $\theta$ from the beam axis can be written as

$$P(x,\theta,v)dxd\theta dv = Nv^3 \exp\left(-\frac{v^2}{2\sigma^2}\right)\cos\theta dxd\theta dv \tag{4.21}$$

where $N$ is a normalisation constant unused in the final result and $\sigma = \sqrt{\frac{k_B T}{m}}$ is the standard deviation of the velocity distribution.

Applied to our case of a two slits collimation of equal sizes, this probability can be reduced to

$$P(v_\perp) = \frac{|v| \exp\left(\frac{-v_\perp^2}{2\sigma^2}\right)\Gamma\left(-\frac{1}{2}, \frac{v_\perp^2 L^2}{2\sigma^2 a^2}\right)}{4\sqrt{\pi\sigma^2\left(1+\frac{a^2}{L^2}\right)^{1/2}}} \tag{4.22}$$

where $v_\perp$ denotes the velocity normal to the beam direction and $\Gamma(s,z) = \int_z^\infty t^{s-1}e^{-t}dt$ the

incomplete gamma function.

**Integration over each velocity class**

Given a velocity class $v$ at the output of the oven, the atomic trajectory is calculated using a fourth-order Runge-Kutta method. Three output are possibles: the atom goes back to the oven, the atom hits the sapphire window located 35 cm away from the 2D-MOT chamber and the atom is trapped in the 2D-MOT.

Supposing a constant radial expansion given by equation 4.22, the proportion of atoms leaving the Zeeman Slower beam (or the overlap of the two in the case of the combined Zeeman Slower, see section 4.3.4) and thus not influenced anymore by the Zeeman Slower can be computed. The number of atoms effectively captured in the 2D-MOT is derived by adding the losses due to radial expansion to the losses resulting from atoms hitting the sapphire window and those pushed back into the oven.

This expansion has a non-negligible impact on the atom number effectively trapped in the 2D-MOT but it can be compensated. Focusing the Zeeman beam on the oven output is a first idea to provide a transverse component to the $\vec{k}$ vector but is rather ineffective.

The most efficient way would still be to add one or several two-dimensional optical molasses inside the slower [126, 131]. To achieve this, generating the magnetic field orthogonal to the thermal beam using permanent magnets is preferable, as using a coil could potentially hinder a transverse slowing beam and limit the transverse expansion, thereby necessitating a more complex design.

### 4.2.3 Implementation of an asymmetric magnetic field

The radial expansion is the most important factor limiting the efficiency of the slowing process. A lossless single Zeeman Slower at -14 $\Gamma/(2\pi)$ captures atoms up to 320 m/s, corresponding to 27.6% of the thermal distribution. Nevertheless, introducing the cloud expansion of the atomic beam, this quantity is reduced to 2.79%. For comparison purposes, the 2D-MOT alone is expected to trap 0.41% of the atoms without Zeeman Slower and 0.11% if the radial losses are taken into account. Those losses are particularly important for long trajectories (in blue in Figure 4.7) because the atoms spend a longer time at slow velocity and thus, are more

subject to the cloud expansion. A travel of this kind lasts approximately 29 ms.

A solution to circumvent this issue is to reduce the duration of the trajectories. To this aim, an asymmetric magnetic field is introduced adding magnets on the stack on the side of the sapphire window (higher z). Therefore, the unmodified stack is composed of 9 permanent magnets (Eclipse Magnetics Ltd, model N750-RB) while the other is now composed of 14 magnets. The modified magnetic field generated increases the magnetic field "barrier" and shortens the duration of the atomic trajectories down to 7 ms, thus reducing the losses due to radial expansion. This configuration should capture 4.56% of the thermal distribution (including radial losses), thus 1.6 time more atoms than in the case of the symmetric magnetic field.

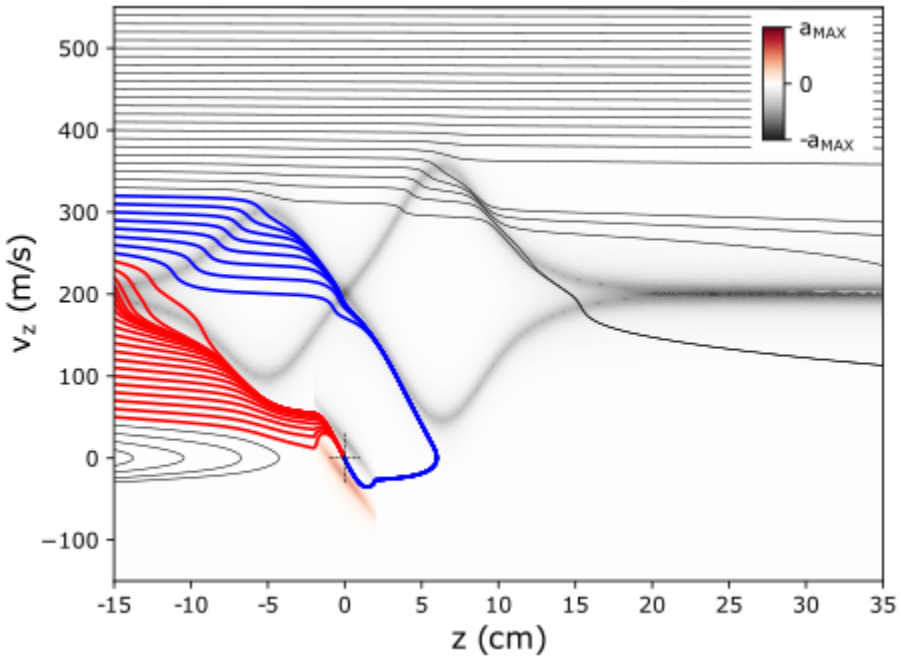


Figure 4.10: The Zeeman Slower acting with a modified magnetic field to damp the trajectories, reducing the travel time of the atoms to 7 ms and mitigating the effect of the cloud expansion on the atomic number trapped in the 2D-MOT.

Using such a modified configuration changes the magnetic field, and most notably shifts the position where it vanishes. To maintain the same MOT location the modified magnet stack is moved by a calculated distance of 1.23 cm. In this way the trapping axis of the 2D MOT remains aligned with the hole maintaining the differential vacuum between the two chambers.

### 4.2.4 Measurement process

**Camera acquisition**

The evaluation of the Zeeman Slower efficiency is done by measuring the flux of atoms captured by the 2D MOT. To this aim, the push beam (aligned along the y axis) is blocked and a mirror placed in the region initially reserved for the push beam redirects the image of the 2D-MOT in the plan of the beams toward the camera (ORCA-Fusion BT Digital CMOS camera, Hamamatsu).

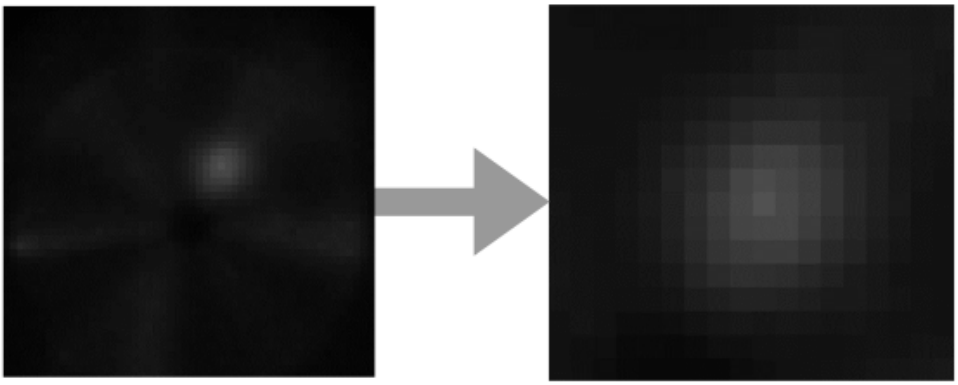

Figure 4.11: Fluorescence of the 2D-MOT taken using a CMOS camera aligned along the y-axis. The picture is cropped around the 2D-MOT for analysis purpose and the exposure time of the camera has been adjusted to avoid saturation.

The efficiency of the Zeeman Slower is evaluated by comparing the atomic flux trapped by the 2D-MOT with the reference value obtained with the 2D-MOT beams only. The atom number can be deduced from the picture of the 2D-MOT taken in the plan of the MOT beams. Indeed, the picture's intensity can be fitted with a 2D Gaussian function whose integral value is proportional to the atom number.

Nevertheless some care has is required to avoid systematic errors in this analysis. First, the background signal, that is to say any information not related to the 2D-MOT, has to be removed. Therefore, the picture is cropped around the MOT before the fitting process. This step is crucial as cropping too much the picture will distort the fit by the Gaussian function and result in an incorrect estimation of the atom number. On the other side, not cropping enough the picture will add to much information from the background. Once a region has been selected to be the region of interest, it has to be kept for all measurements, with or

without Zeeman Slower.

To analyse the Zeeman Slower efficiency, this measurement process is applied to a picture with the 2D-MOT alone and to a picture with the Zeeman Slower active. The ratio between the integral value calculated for the picture with the Zeeman Slower and the picture without yields the atomic flux gain generated by the Zeeman Slower.

### 4.2.5 Experimental result of the enhanced Zeeman Slower

The Zeeman Slower of this measurement consists of a beam of 200 mW frequency shifted by -14$\Gamma/(2\pi)$ and with a saturation parameter of 1.7 on each polarization. Such a configuration traps 19.80 times more atoms using a symmetric magnetic field and 32.15 times more atoms using the modified magnetic field.

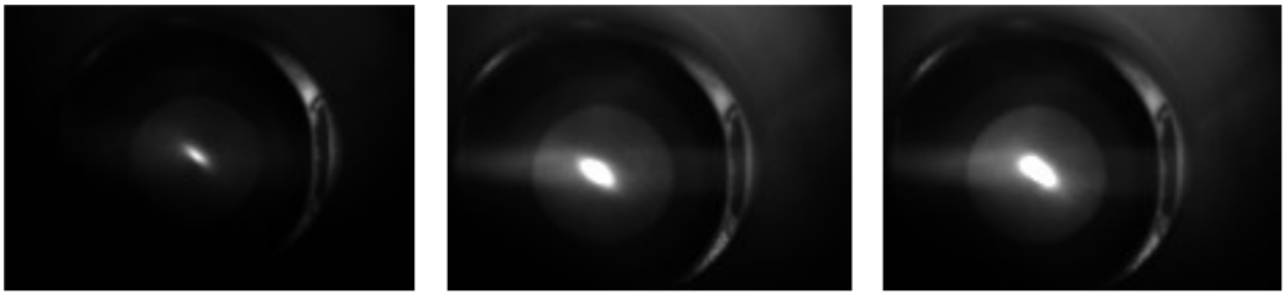

Figure 4.12: Picture of the 2D-MOT. From left to right: without Zeeman Slower; with 200 mW of a Zeeman Slower beam at -14 $\Gamma$, s = 1.7 and with a symmetric magnetic field; with the same Zeeman Slower beam but with the modified magnetic field to mitigate the impact of cloud expansion. The pictures are saturating for illustration purpose (but taken in the same conditions) while the measurements are done at a shorter exposure time.

If these measurements reveal that the shape of the magnetic field has an impact on the atom number in the 2D-MOT, it is important to consider that with a Zeeman Slower beam of this diameter, there are atoms originating from the oven outside of the beam's radius. Consequently, these atoms do not interact with the Zeeman Slower beam.

If the results are in good qualitative agreement with the predicted values, discrepancies can be observed for both magnetic field configurations. These discrepancies are primarily caused by uncertainties in the laser beam size, leading to uncertainties in the saturation parameter. Furthermore, the numerical simulation estimates cloud expansion from a sin-

| Atomic Gain | **B** symmetric | **B** modified |
|---|---|---|
| Theory | 25.90 | 39.09 |
| Measured | 19.80 | 32.15 |

Table 4.1: Comparative table of the impact of the magnetic field on the atomic gain of the Zeeman Slower. The value exposed represents the ratio between the number of atoms trapped in the 2D-MOT with the Zeeman Slower and the number of atoms trapped without Zeeman Slower.

gle microtube, whereas the oven output consists of an array of microtubes. Section 4.4 is dedicated to a discussion of the experimental results.

## 4.3 Double frequency Zeeman Slower

The Zeeman Slower previously described has the double feature of mitigating the effect of the thermal beam expansion on the atomic number trapped in the 2D-MOT by the choice of its magnetic field and of interacting with a wide range of velocity classes by the choice of its laser frequency. However, the maximum velocity effectively trapped thanks to the Zeeman Slower can be increased adding another frequency to the Zeeman Slower, that is to say to overlap two Zeeman Slower beams with different frequencies.

### 4.3.1 The cascade effect

This effect occurs when an atom is interacting successively with two Zeeman Slower beams at different detuning. It is used in this work to extends the maximum velocity class trapped by the 2D-MOT.

The Zeeman Slower beam of the previous section, shifted by -14 $\Gamma/(2\pi)$, is involved in the double Zeeman Slower. It will be denoted ZS1. The Zeeman Slower beam whose detuning is larger than ZS1 and interacting with the atoms in region ① will be denoted ZS2.

ZS1 slows down atoms whose velocity at the output of the oven is up to 320 m/s, to a velocity class trapped by the 2D-MOT beams. ZS2 shifted by -29 $\Gamma/(2\pi)$ will slow down faster atoms, up to 450 m/s, but at the end of the magnetic field's slope they will be too fast to reach a velocity that can be trapped by the 2D-MOT. This is where the idea to use two laser beams

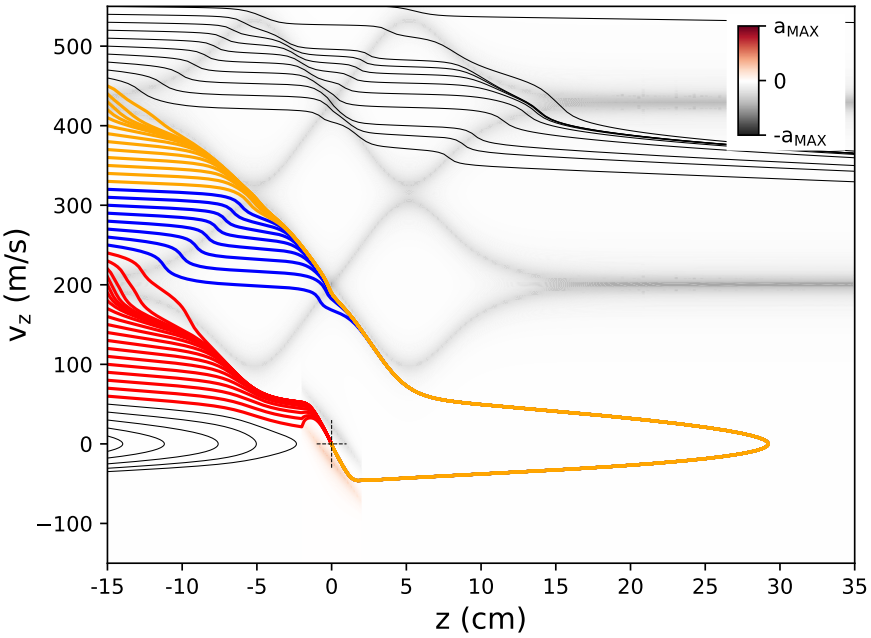


Figure 4.13: Phase space plot representing the cascade effect, where atoms with velocities up to 450 m/s are decelerated by the first Zeeman Slower (depicted by yellow trajectories) to reach a sufficiently slow velocity (approximately 320 m/s) for interaction with the second Zeeman Slower. The horizontal axis represents atomic positions along the thermal beam propagation direction, with the 2D-MOT located at 0 cm, while the vertical axis represents atomic velocities at the oven's output. The plot also shows the acceleration experienced by a velocity class interacting with a Zeeman Slower beam at a specific position, which is indicated by the colorbar.

at different detuning comes from. ZS2 slows down fast atoms from 450 m/s down to 320 m/s in region ①, then ZS1 slows down these atoms ② in addition to those below 300 m/s at the output of the oven.

Given the Maxwell-Boltzmann distribution of an oven at 550°C, extending the maximum capture velocity from 320 m/s to 450 m/s increases the number of atoms trapped in the 2D-MOT from 27.50% to 54.12%, so almost twice the atomic flux.

**Transitions addressed**

Let us consider a decreasing magnetic slope in the MOT region, resulting in a positive magnetic field between the oven and the 2D-MOT. In accordance with the formula of the Zeeman effect (Equation 4.8), a positive value of $m_j$ (associated with a $\sigma^+$ transition) corresponds to a

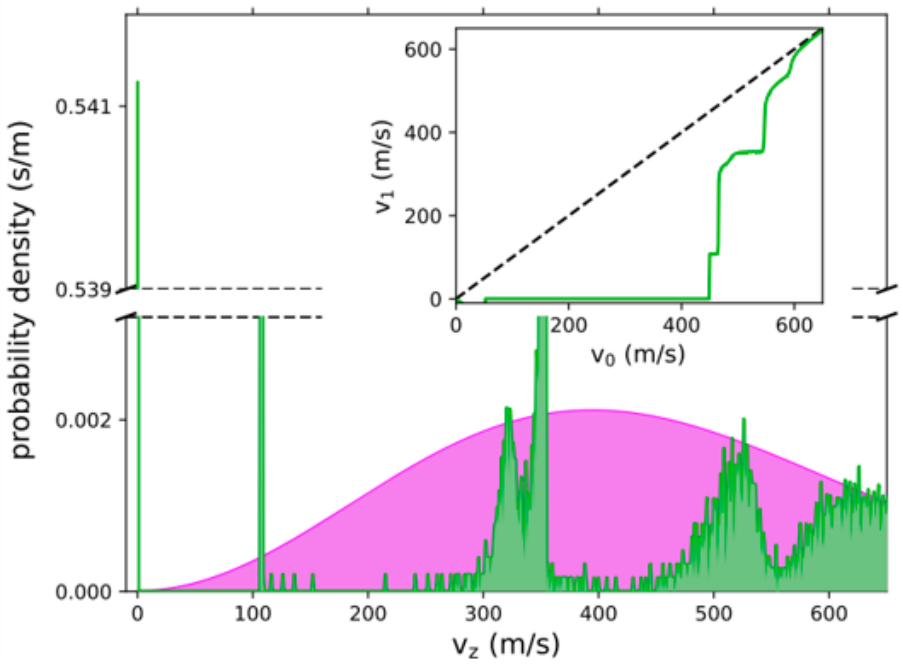


Figure 4.14: Probability density versus atomic velocity. In pink the Maxwell-Boltzmann distribution from an oven at 550°C and in green the theoretical distribution with both Zeeman Slowers on.

larger energy difference, while a negative value of $m_j$ (related to a $\sigma^-$ transition) corresponds to a smaller energy difference.

The experimental setup takes full advantage of the magnetic field introduced by the permanent magnets. Indeed, using a single Zeeman Slower, atoms will be slowed down either on a slope via a $\sigma^-$ transition, either on the other via $\sigma^+$ transition. In this double frequencies scheme, fast atoms are interacting via a $\sigma^-$ transition in region ① and via a $\sigma^+$ transition in region ② (the regions are labeled in Figure 4.3).

Given the light polarization, the atoms can interacts with the cooling beam on both transitions. The Doppler shift makes one more probable than the other. If the magnetic field's direction is orthogonal to the atomic beam orientation, a linearly polarized Zeeman beam co-linear to the magnetic field will address a $\pi$ transition. At the opposite, a linearly polarized Zeeman beam orthogonal to the magnetic field can be decomposed into two circularly polarized beams circulating around the $\vec{B}$ orientation, thus inducing at the same time a $\sigma^+$ and a $\sigma^-$ transition. Any polarization is a composition of two orthogonal linear polarizations, hence it is not possible to address a $\sigma^+$ transition independently from a $\sigma^-$ transition. Corol-

lary, half of the laser power is lost on an unused transition while shining a linearly polarized Zeeman Slower orthogonal to the magnetic field's orientation.

**Multi-detuned cascade scheme**

A Zeeman Slower based on strontium slowing atoms coming from an oven at 550°C does not benefit from a laser beam at a third frequency. Indeed, supposing that a third Zeeman Slower beam manages to slow down atoms and puch them back to the 2D-MOT region, those atoms will be too fast to be trapped by the MOT.

Moreover, the atoms will spend a non negligible time at slow velocity an thus be more subject to cloud expansion (see section 4.2.2). Finally, given the Maxwell-Boltzmann distribution at 550°C (see Fig 4.14), trapping atoms up to 450 m/s already addresses a consistent portion of the atom distribution, making the use of an additional Zeeman Slower beam at a different detuning less interesting.

**Hybrid Zeeman Slower**

Another scheme of a Zeeman Slower involving two detuning has been investigated by Jianing Li *et al.*. in 2022 [132], work to which I collaborated as concerning the conception.

In this setup, ZS2 is shifted by -380 MHz and addresses a $\sigma^-$ transition while ZS1 is set to address a $\pi$ transition shifted by -180 MHz from the transition. This $\pi$ transition is used to slow down atoms throughout the atomic beam's path via radiation pressure, thus increasing the number of atoms slowed down by the classic Zeeman slower on the $\sigma^-$ transition.

This configuration make use of all the available laser power, however it results less efficient because it is a non resonant process, slowing down atoms via radiation pressure is less effective than using a $\sigma$ transition.

### 4.3.2 The choice of the second frequency

The frequency of ZS1 is identical as described in section 4.2, with a detuning of -14 $\Gamma/(2\pi)$. ZS2, the cooling beam with a large frequency detuning, does not add any atom to the 2D-MOT if employed alone; its role, however, is to slow down vary fast atoms at the output of the oven, so as to have them within the capture range of the ZS1 beam by addressing the $\sigma^-$ transition.

Thus, to slow atoms down to 320 m/s 5cm away from the 2D-MOT chamber given the magnetic slope generated by the permanent magnets, a detuning of maximum -29 $\Gamma(/2\pi)$ can be implemented for ZS2. It yields a maximum capture velocity of $\sim$ 450 m/s.

A larger detuning would slow down atoms of a higher velocity class but to a final velocity too fast to be captured by ZS1.

A smaller detuning would engage the cascade effect but as a result, less velocity classes would be interrogated. Depending on the laser power available, the saturation parameter could be too low and thus, reducing the detuning could still be an option.

### 4.3.3 The influence of the saturation parameter

The magnetic slope profile and the detuning are not the only parameters to decelerate the atoms. This section discusses the laser intensity's impact on the Zeeman Slower efficiency.

**Low saturation parameter**

From equation 4.10, a non sufficient saturation parameter would result in a too weak force experienced by the atoms to maintain the resonance condition along the Zeeman Slower slope and hence end up trapped in the 2D-MOT. One cycle in the slowing process requires a succession of absorption and spontaneous emission. The latter presents a Lorentzian form, thus the average time at which the atom will re-emit the photon previously absorbed is the inverse of the natural linewidth $\Gamma$.

The shorter the re-emission time and the better is the atomic deceleration, thanks to the fact that the atoms will be able to cycle faster on the cooling transition

The shorter is this re-emission time and the better is the atomic deceleration, thanks to the fact that the atoms will be able to cycle faster on the cooling transition. With its natural linewidth of 30.5 MHz [84], the blue cooling transition in $^{88}$Sr is an excellent candidate for a Zeeman Slower, the atoms re-emitting the photons 5 ns after absorption.

If the saturation parameter is high enough to slow down the atoms from a velocity $v_0$ to a velocity $v_f$, it means the force $F_{ZS}$ undergone by the atoms from the Zeeman beam is superior to the minimum force $m \times a_{min}$ required to slow down the atoms along the distance $d$:

$$F_{ZS} \geqslant m \times a_{min}$$

Using equation 4.10, the threshold saturation parameter $s_{thresh}$ can be written as

$$s_{thresh} = \frac{2ma_{min}}{\hbar k\Gamma - 2ma_{min}} \left(1 + \left(\frac{2\delta_{ZS}}{\Gamma}\right)^2\right) \tag{4.23}$$

With $\Delta v = v_f - v_0$, $a_{min}$ can be expressed in term of the time of flight $t$ as $a_{min} = \frac{\Delta v}{t}$.

As $a_{min}$ is constant, $t$ is

$$t = \frac{v_0(1 + \sqrt{1 - \frac{2a_{min}d}{v_0^2}})}{a_{min}}$$

Using this expression of the time of flight in $a_{min} = \frac{\Delta v}{t}$, it yields an expression of $a_{min}$

$$a_{min} = \frac{{v_0}^2}{2d} \left(1 - \left(\frac{\Delta v}{v_0} - 1\right)^2\right) \tag{4.24}$$

In our experimental configuration, the effective slowing distance for the Zeeman Slower beam spans approximately 10 cm. Given an initial atom velocity of 450 m/s and a velocity alteration of 150 m/s, the minimum acceleration $a_{\text{min}}$ corresponds to approximately $5.6 \times 10^5$ m/s$^2$.

Assuming a perfect Zeeman Slower where $\delta_{ZS} = 0$ at any position in equation 4.23, $s_{tresh}$ is of the order of s = 1.5 for this example. In practical settings, the saturation intensity of the Zeeman Slower beam must be maintained above this threshold as much as possible.

This deceleration can be expressed in term of the magnetic field gradient $B_{grad} = \frac{\Delta B}{d}$. Using equation 4.14, a velocity variation of $\Delta v$ corresponds to a magnetic field variation of $\Delta v = \frac{\alpha_j}{k}\Delta B$ where $\alpha_j = \frac{\mu_B m_j g}{\hbar}$ as in equation 4.16. Hence, the expression 4.24 can be written

$$a_{min} = \frac{v_0^2}{2d} \left(1 - \left(\frac{\alpha_j d}{v_0 k} B_{grad} - 1\right)^2\right) \tag{4.25}$$

**High saturation parameter**

Theoretically, the higher the intensity is, the better will be the Zeeman Slower efficiency. Let's assume an infinite laser power, then the absorption can be assumed to be instantaneous. Thus, the time of a cycle is limited by the time before spontaneous emission $t^{-1} = \Gamma$. From the de Broglie equation

$$\Delta p = \hbar k = m\Delta v$$

can be derived the recoil velocity, that is to say the velocity variation due to a single photon absorption

$$\Delta v = \frac{\hbar k}{m}$$

Given $a = \frac{\Delta v}{t}$, considering $t = \frac{1}{\Gamma}$, it is possible to find again formula 4.11

$$a_{max} = \frac{\hbar k}{mt} = \hbar k \frac{\Gamma}{2m}$$

In practical settings, for a given magnetic field gradient, it is useless to exceed the threshold. Once the atoms can be trapped by the 2D-MOT, decreasing their velocity even more will bring to the same result. Especially while interacting with the atoms via the blue cooling transitions, high powers can be difficult to obtain and one would prefer, for a given laser intensity, to stay near the threshold and to enlarge the beam diameter to interact with more atoms and to decrease the impact of the thermal beam expansion.

Finally, the atoms scatter photons off-resonance. The negative effect of the off-resonance scattering is stronger for slow atoms, which have more time to interact with the laser beam. In the conditions of our experiment, atoms slower than 50 m/s are pushed back toward the oven before reaching the 2D-MOT due to off-resonance scattering (see Figure 4.13). This portion of the Maxwell-Boltzmann distribution consists of velocity classes with a smaller atomic fraction with respect to the velocity classes trapped in the 2D MOT, thus the Zeeman Slower effectively add atoms to the 2D-MOT. Nevertheless, increasing the intensity would also increase the scattering of off-resonance photons and as a result repel more atoms toward the oven.

### 4.3.4 The combined Zeeman Slower

For the sake of clarity, in the previous section the double frequency Zeeman Slower adopted a symmetric magnetic field. In this section we consider instead the magnetic field described in section 4.2 for the double Zeeman Slower to mitigate the effect of the cloud expansion on the atom number in the 2D-MOT.

The alignment of the two Zeeman Slower beams is particularly critical as each atom has to interact with both laser beams along its trajectory. To ensure this condition, the two Zeeman

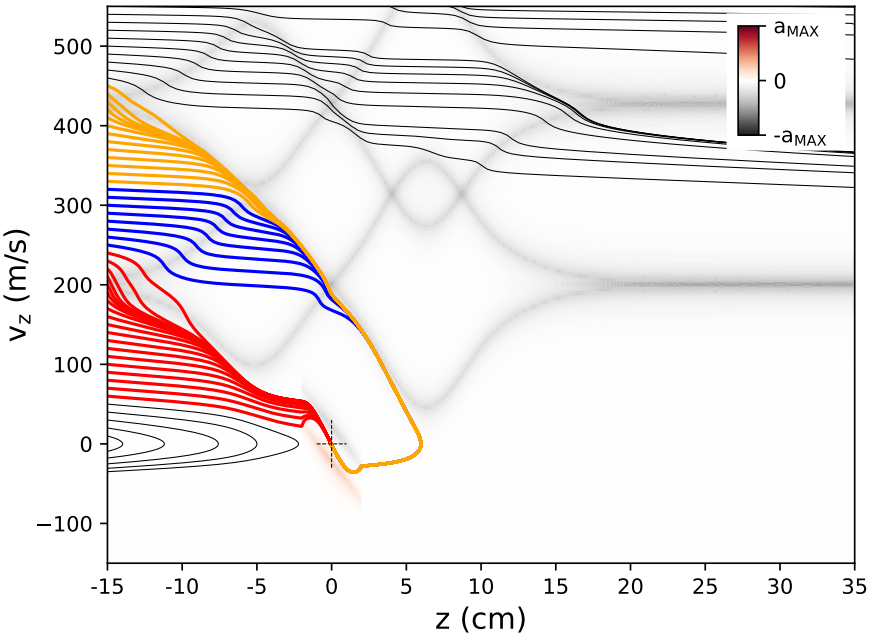


Figure 4.15: Action of the combined Zeeman Slower on each velocity class. Two laser beams, ZS1 and ZS2, shifted by -14 $\Gamma(/2\pi)$ and 29 $\Gamma(/2\pi)$ respectively are decelerating atoms in cascade up to 450 m/s (velocity classes in yellow). ZS1 also interacts alone with atoms either via the $\sigma^+$ transition (velocity classes in blue) or via the $\sigma^-$ transition (velocity classes in red). The asymmetric magnetic field is employed to mitigate the impact of the cloud expansion on the atomic flux.

Slower beams are overlapped using a 50:50 beam splitter (BS) cube far upstream the MOT despite of the fact half of the power is lost.

The minimum saturation parameter required for each beam of the combined Zeeman Slower can be computed using equation 4.23. Decelerating atoms from 450 m/s to 320 m/s over 10 cm, the saturation intensity of ZS2 has to be above 1.14. Similarly, decelerating atoms from 320 m/s to 50 m/s along 10 cm yields a minimum saturation parameter of 1.27 for ZS1.

In practical settings, the first Zeeman Slower beam (ZS1) is at -14 $\Gamma$ and 80 mW on 0.80 cm$^2$, so s = 1.17 on each polarisation. The second Zeeman Slower beam (ZS2) is at -24 $\Gamma$ and 150 mW on 0.96 cm$^2$, so s = 1.84 on each polarisation. Because ZS2 does not add atoms to the 2D-MOT when interacting alone with the atoms, its beam size can be reduced to be as large as 0.80 cm$^2$, the surface of ZS1.

The saturation parameter of ZS1 is below the minimum saturation parameter required to slow down atoms from 320 m/s to 50 m/s along 10 cm. In order to engage the cascade effect despite of this saturation parameter, the detuning of ZS2 has been shifted closer to the atomic transition from - 29 $\Gamma(/2\pi)$ to - 24 $\Gamma(/2\pi)$.

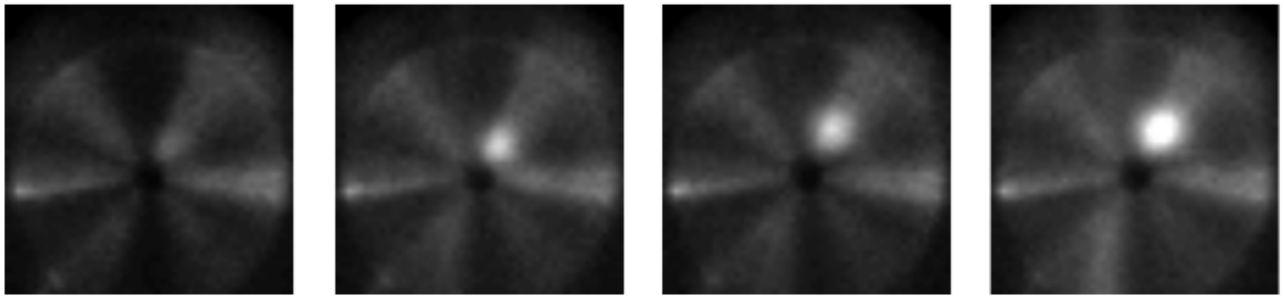

Figure 4.16: Picture of the 2D-MOT. From left to right: No Zeeman Slower; with a Zeeman Slower at -14 $\Gamma$ and s = 1.17 using a symmetric magnetic field; with the same Zeeman Slower beam using the modified magnetic field; still using the modified magnetic field but with the introduction of a second Zeeman Slower beam at -24 $\Gamma$ and s = 1.84. The central aperture measures a diameter of 2.7 mm.

ZS1 is shifted by -24 $\Gamma(/2\pi)$. Such a laser does not add any atom to the 2D-MOT when interacting alone with atoms. Therefore, observing a gain of atoms in the 2D-MOT while shining ZS2 and ZS1 is a signature of the cascade effect.

Nevertheless there is a discrepancy with the theoretical values, mainly imputable to the lack of power introduced by the BS. The simulation estimates s = 1.4 while in practice, s = 1.17 for the Zeeman Slower at the lowest detuning. As mentioned previously, the alignment is critical: ZS2 has to perfectly overlap ZS1. Motivated by the attempt to make use of all the available optical power, tests have been made with ZS2 and ZS1 not overlapped on a BS but coming from two different mirrors far upstream the MOT chamber, producing a small angle between the two beams. The cascade effect was not observed in this configuration.

| | MOT alone | 1 ZS and **B** symmetric | 1 ZS and **B** modified | 2 ZS and **B** modified |
|---|---|---|---|---|
| Theory | 1 | 17.1(5) | 26.5(7) | 33.0(8) |
| Measured | 1 | 14.2(16) | 21.3(26) | 35.4(28) |

Table 4.2: Comparative table of the impact of the magnetic field on the combined Zeeman Slower's efficiency. The theoretical error bars are taken assuming an uncertainty of $\pm$5% on the laser beam diameter.

The measurements closely align with the numerical predictions, signifying an improved evaluation of beam size and saturation parameter estimations in this subsequent experiment. The most optimal configuration shows to trap up to 35 times more atoms than the 2D-MOT alone. The ensuing section expounds upon the constraints inherent to this Zeeman Slower and elucidates potential methodologies for surmounting them.

## 4.4 Limitations and possible improvements

The most significant losses experienced in this setup are caused by the cloud expansion of the atomic beam. This issue can be circumvented by using frequency shifted beams to slow down the atoms at the output of the oven in the transversal plane of the atomic beam [126, 131]. For such a design, using permanent magnets producing a magnetic field orthogonal to the thermal beam emanating from the oven instead of coils is advantageous because the magnetic field source does not introduce barriers to the laser field.

### 4.4.1 The serrodyne technique

To have the best atomic flux, the most critical aspect is to ensure that ZS2 and ZS1 are both interacting with the atoms leaving the oven. While the alignment can be efficiently adjusted using a BS at the cost of losing half of the power, the beam profile of ZS2 may not necessarily match the one of ZS1. Consequently, the cascade effect may not be engaged at some locations of the beam profile, thus reducing the efficiency of the combined Zeeman Slower.

A method that can address both the alignment issue and the mode matching issue between ZS2 and ZS1 is to employ the serrodyne technique [133, 134]. This technique involves frequency modulation achieved by ramping the phase of an optical wave with a sawtooth signal. With this approach, a frequency shift from 200 MHz to 1.6 GHz can be induced and its efficiency can reach up to 80%. To overcome the lack of wideband EOM in the blue domain, the serrodyne technique can be applied to a laser field at 922 nm before being frequency-doubled via a crystal in a second harmonic generation (SHG) scheme.

### 4.4.2 Light induced ablation

An effect that has been observed in our setup, but not mentioned until now, is the ablating effect produced by each Zeeman Slower beam [99, 100]. This observation is supported by the inspection of the pressure in the 2D-MOT chamber increasing by an order of magnitude.

Nevertheless, even though this effect makes the evaluation of the Zeeman slower performance more difficult, light-induced ablation can be effectively utilized to load more atoms into a MOT.

### 4.4.3 Repumper for Zeeman Slower

Another aspect to discuss is the atomic leakage from the blue cooling transition, and most notably form the upper level $^1P_1$. However, it is taken into account in the theroretical atomic gain presented in tables 4.1 and 4.2. As mentioned in chapter 2, an atom interacting with a laser field on the blue cooling transition has a probability $\eta = \frac{1}{49194}$ to decay to $^1D_2$. Given the time it takes to decay via the other transitions before going back to $^1S_0$, the atoms will not interact with the Zeeman Slower again and can thus be considered lost.

Using equation 4.19, the probability for an atom to be lost during the slowing process can be expressed as

$$P_{lost} = 1 - (1 - \eta)^N \tag{4.26}$$

For 320 m/s, the highest velocity of the first Zeeman Slower, it corresponds to 49% of the atoms lost and for 450 m/s, the highest velocity of the second Zeeman Slower, it is 57%.

Thus, this loss cannot be neglected in an optimized combined Zeeman Slower and atoms decaying to $^1D_2$ have to be repumped as quickly as possible, to maintain the resonance condition with the Zeeman Slower beam, which depends on the atom position and velocity. Only one repumper could verify the requirements of this scheme: a repumper at 448 nm between $5s4d\,^1D_2$ and $5s8p\,^1P_1$ with a linewidth of 3.0 MHz. Then, the majority of the atoms decay back to the ground state in less than a $\mu$s [135].

| Path | Probability [%] | Lifetime [ns] |
|---|---|---|
| $5s8p\,^1\mathrm{P}_1 \rightarrow 5s7s\,^1\mathrm{S}_0 \rightarrow 5s5p\,^1\mathrm{P}_1 \rightarrow 5s^2\,^1\mathrm{S}_0$ | 1.23 | 1377 |
| $5s8p\,^1\mathrm{P}_1 \rightarrow 5s6s\,^1\mathrm{S}_0 \rightarrow 5s5p\,^1\mathrm{P}_1 \rightarrow 5s^2\,^1\mathrm{S}_0$ | 7.15 | 434 |
| $5s8p\,^1\mathrm{P}_1 \rightarrow 5s^2\,^1\mathrm{S}_0$ | 40.05 | 67 |
| $5s8p\,^1\mathrm{P}_1 \rightarrow 5s4d\,^1\mathrm{D}_2$ | 47.85 | 56 |

Figure 4.17: List of the four decaying paths with the highest probability and their corresponding lifetime. Credit: [135].

### 4.4.4 Other alkaline-earth-like candidates

We consider here which other atomic species could profit from an atomic source similar to what we propose in this chapter.

**Ytterbium**

Ytterbium is another alkaline-earth-like element widely adopted by the cold atom community. From the BEC perspective, the most abundant isotope, $^{174}Yb$, presents a scattering length that is very well adapted for evaporative cooling. BECs up to 150,000 atoms have been achieved [136]. In addition to the qualities of every alkaline-earth-like element, Ytterbium presents two clock transitions [137, 136], can be cooled down to approximately 10 $\mu$K in a single cooling stage, and is one of the heaviest alkaline-earth-like elements, making Yb a key candidate for experiments where the atomic number significantly influences the observed phenomenon [90, 91].

The Yb atom exhibits a first cooling stage comparable to Sr with a transition at 399 nm and a linewidth of 29 MHz. Therefore, a combined Zeeman Slower acting on this transition would give similar results but over a longer distance, as the recoil velocity is twice lower for Yb than for Sr.

Moreover, Yb has the particular property of having the $^1D_2$ state at a higher energy level than $^1P_1$. The only decay path is directly to $^3D_{1,2}$ [85]. As a result, the leakage from $^1P_1$ is as low as $1/10^7$ and no repumper has to be employed in this scheme. Thus, the combined Zeeman Slower would work particularly well for this atom.

**Cadmium**

As mentioned in chapter 1, the level structure of Cd is somewhat similar to Sr, dividing the

wavelengths by a factor of two. Concerning the first cooling transition at 229 nm, it exhibits a linewidth of 91 MHz, which is three times larger than the one of Sr on the blue cooling transition. Given that the recoil velocity is not very different between these atoms, cadmium would also be a good candidate for this type of Zeeman Slower.

**Calcium**

The first cooling transition of calcium at 423 nm exhibits a linewidth of 35 MHz and a branching ratio of $1/10^5$ to $^1D_2$. With an atomic number of Z = 20, this atom will be of similar interest with regard to the combined Zeeman Slower. Nonetheless, as each property of calcium is better for Zeeman cooling, it can be calculated that slowing atoms from 450 m/s to 50 m/s would introduce a loss of only 16% of the initial thermal distribution, making a repumper not necessarily relevant for this atom.

# Chapter 5

# Coherent Electromagnetic Manipulation for Atomic Interferometry

This chapter encompasses an exploration of two distinct facets within the realm of atomic physics. The initial segment is devoted to the compelling advantages exhibited by $^{88}$Sr in comparison to other atomic candidates, particularly concerning its suitability for atomic interferometry. Subsequently, the chapter delves into the technical underpinnings that underscore the implementation of atomic interferometers within cavities. These dual perspectives culminate in an insightful analysis of a novel scheme: a cavity-based atomic interferometer leveraging the unique attributes of $^{88}$Sr.

In Section 5.1, an examination unfolds regarding the adoption of the isotope $^{88}$Sr within the optical clock community, underscored by its suitability as a paramount candidate for atomic interferometry due to its favorable decoherence characteristics. Building on this, Section 5.2 elucidates the pivotal theoretical insights governing the manipulation of coherence in bosonic alkaline-earth-like atoms. The discourse is enriched in Section 5.3 that expounds upon the merits intrinsic to cavity-based atomic interferometers, interwoven with an exploration of the potential integration of $^{88}$Sr into such a configuration.

## Contents



## 5.1 $^{88}$Sr, a prime candidate for atomic physics research

Until recently, the clock transition of $^{88}$Sr had not found practical applications due to its remarkably long lifetime of $\Gamma_{\text{clock}} = 5.5 \times 10^{-12}\ s^{-1}$ [80]. However, at the beginning of the millennium, the atomic clock community proposed several innovative methods to interact with the atoms, enabling the effective utilization of the clock transition.

### 5.1.1 Optical clocks based on $^{88}$Sr

Built upon the theoretical work accomplished by Taichenachev *et al.* in 2006 [138], the first optical lattice clock based on bosonic atomic isotope was demonstrated at NIST using $^{174}$Yb [139]. In this experiment, a static magnetic field of approximately 1 mT excited the

forbidden clock transition at 578.42 nm of $^{174}$Yb, resulting in a linewidth of 20 Hz. Shortly after, Baillard *et al.* from the SYRTE conducted a similar experiment on $^{88}$Sr [140].

The next section (5.2) is dedicated to the theoretical foundation of such excitation by an external field on the atom.

Those pioneering experiments on bosonic alkaline-earth-like atoms inspired laboratories around the world to adopt the same approach for their atomic clocks, as demonstrated by the Tokyo group [141] and the JILA [142]. This preference within the atomic clock community is motivated by the unique challenges and implications associated with utilizing fermionic alkaline-earth-like atoms.

Indeed, for fermionic alkaline-earth-like atoms, fluctuations in the lattice light polarization may result in significant frequency shifts, as large as 10 Hz, due to the hyperfine structure [143]. Additionally, fermionic atoms possess a non-zero nuclear spin (I = 9/2 for $^{87}$Sr), leading to a non-negligible sensitivity to magnetic fields. To overcome these disadvantages, bosonic species are often chosen, although this necessitates a precise manipulation of an external magnetic field.

### 5.1.2 Factors limiting the coherence time of neutral atoms

In atomic interferometry, the phase of the atomic wavefunction plays a central role, governing interference through quantum superposition of distinct states. The coherence time represents the duration of coherence in the quantum system (e.g., neutral atoms). A shorter coherence time increases uncertainty in the relative phase between states, resulting in weaker interferometric signals and higher susceptibility to noise, thereby limiting measurement precision.

**Spontaneous emission**

The most widely recognized source of decoherence in neutral quantum systems is spontaneous emission [15]. When a photon is emitted through this phenomenon during the Rabi evolution, it causes the wavefunction to collapse to a lower energy state, disrupting the phase evolution.

The time-energy Heisenberg inequality relates the lifetime of the excited state to the linewidth of the transition, which can be computed using the transition moment integral.

When constructing an atomic interferometer, the chosen transition must have a linewidth that does not lead to rapid decoherence compared to the phenomenon probed by the interferometer.

**Laser beam quality**

The direct imprinting of optical phase onto the phase of the atomic wavefunction [144, 145] establishes a crucial link between the laser's phase stability and the coherence of atomic states. Consequently, fluctuations in the laser's phase used for probing the atomic sample can have a profound impact on coherence. Thus, the wavefront quality directly influences the overall coherence of the atomic system. Additionally, any imperfections regarding the optics present in the experimental setup introduce unwanted phase shifts that can detrimentally affect the interferometric measurements.

**Interactions with parasitic fields**

An external electromagnetic field can lead to the formation of a dressed state, altering the level structure of the atom and causing it to differ from that of the unperturbed atom. For instance, a magnetic field induces the Zeeman effect on the level structure, while an electric field induces the Stark effect. These fields may arise as stray fields from the experiment's environment or be deliberately introduced, such as in the case of a laser field used for trapping atoms in an optical lattice. Interactions with electric or magnetic fields can perturb the phase evolution of the atomic sample, leading to decoherence during its interaction with the interferometric laser.

Depending on the phenomenon being probed by the interferometer, fluctuations in the gravitational field are regarded as parasitic fields, leading to undesired phase shifts in the interference pattern. In this context, seismic fields, ocean tides, and more broadly, Newtonian noise can be classified as parasitic fields.

**Atomic collisions**

Collisions among the constituents of the atomic sample or between atoms and external entities, such as a buffer gas, disrupt the wavefunction of the system. Consequently, the coherence of the colliding atoms is lost, leading to a reduction in the fringe contrast.

At low temperatures, the interaction between two particles can be characterized by the

s-wave scattering length, denoted as "a". This parameter pertains to a type of scattering that involves no angular momentum in the initial or final state, occurring through the s-wave channel. The scattering length "a" can take positive, negative, or zero values, which respectively indicate repulsive, attractive, or resonance-enhanced interactions between the particles. In cases where the scattering length is positive, the particles tend to repel each other, whereas a negative scattering length implies an attractive interaction.

In the case of alkali atoms, the scattering length can be readily adjusted using a magnetic field in the vicinity of a Feshbach resonance [146]. However, due to the absence of total angular momentum in the ground state of alkaline-earth-like atoms, this approach becomes impracticable for them.

**Other sources of decoherence**

Among the various stray electromagnetic fields, the black-body radiation (BBR) produced by the laboratory environment is a significant factor. While the scattering force of BBR on the atoms can generally be disregarded at room temperature, the atoms still experience coherent interactions with this field [147]. Typically, in atomic interferometry, the influence of BBR is not taken into consideration, but in the context of optical atomic clock experiments, it has gained paramount importance.

Another source of decoherence that may be considered is the presence of surfaces in proximity to the atoms probed [148]. However, in this current work, the effect of surface interactions is neglected as the atomic sample is assumed to be perfectly isolated in a vacuum environment.

### 5.1.3 Relevant properties of $^{88}$Sr for atomic interferometry

Considering the aforementioned conditions, $^{88}$Sr emerges as an ideal candidate for atomic interferometry. That this isotope is prevalence in natural Sr, constituting approximately 82.5% of the total, is merely a fortuitous coincidence.

**Clock transition**

As described in Chapter 2, the transition $^1S_0 \rightarrow {}^3P_0$ state is doubly forbidden. While in the case of $^{87}$Sr, this transition is weakly dipole allowed due to hyperfine mixing, for $^{88}$Sr, its

decay rate $\Gamma_{clock}$ is extremely small, with a value of $5.5 \times 10^{-12}\ s^{-1}$ [80], and is thus considered effectively null in practical settings.

**Stray fields dependency**

As with all bosonic alkaline-earth-like atoms, $^{88}$Sr possesses no nuclear spin, resulting in the absence of hyperfine structure. Consequently, in its ground state $^1S_0$, this isotope has zero orbital, spin, and nuclear angular momentum. This characteristic renders $^{88}$Sr particularly resilient to the influence of stray electric and magnetic fields [51].

**Atomic cross section**

As the most abundant isotope of strontium is a boson, $^{88}$Sr was initially considered as a potential candidate for Bose-Einstein condensation (BEC) production. However, it was soon discovered that the scattering length of this isotope, concerning $^{88}$Sr-$^{88}$Sr collisions, rendered evaporative cooling on this isotopic species technically infeasible [149, 150].

| | $^{84}$Sr | $^{86}$Sr | $^{87}$Sr | $^{88}$Sr |
|---|---|---|---|---|
| $^{84}$Sr | 124 | 32 | -56 | 1800 |
| $^{86}$Sr | 32 | 830 | 164 | 98 |
| $^{87}$Sr | -56 | 164 | 97 | 55 |
| $^{88}$Sr | 1800 | 98 | 55 | **-1** |

Table 5.1: The scattering lengths between the natural isotopes of strontium are typically presented in units of the Bohr radius ($a_0$ = 5.3 $\times 10^{-11}$ m) [151, 152]. While $^{88}$Sr-$^{88}$Sr collisions have scattering lengths of the order of the Bohr radius, this is not the case for interactions involving $^{88}$Sr with the other isotopes.

However, the fact that $^{88}$Sr is immune to decoherence induced by collisions is advantageous for atomic interferometry, especially in environments where this isotope constitutes the sole entity of the atomic cloud. While $^{88}$Sr-$^{88}$Sr collisions can be neglected, interactions between $^{88}$Sr and the other isotopes must be considered. To mitigate this, experimental setups often employ techniques to deflect the atomic thermal beam from the oven to the 3D-MOT chamber, bypassing the collisions with other isotopes thanks to a 2D-MOT.

However, in practice, few experiments can fully benefit from these properties, primarily due to the extremely narrow linewidth of the clock transition, which remains unattainable in its natural state. Therefore, it becomes imperative to devise a strategy that enables an

initially forbidden transition to be rendered allowed, thus unlocking the potential of $^{88}$Sr for atomic interferometry applications.

## 5.2 Theory of coherence manipulation through external fields in atomic systems

The methods discussed in this section primarily revolve around the interaction between $^{88}$Sr and a magnetic field. However, it is important to note that similar calculations can be extended to an electric field by adapting the Hamiltonian accordingly. The detailed derivations for the field's interactions using perturbation theory are provided in the appendix. For the sake of brevity, this section will only present the key results and conclusions derived from these calculations.

### 5.2.1 Coherence manipulation using a static magnetic field

The method introduced by Taichenachev *et al.* in 2006 employs a static magnetic field to induce mixing between two states: $|2\rangle$, which corresponds to the excited state $^3P_0$ of the transition at 698 nm (called the clock transition), and $|r\rangle$, the excited state $^3P_1$ of the transition at 689 nm (called the red cooling transition) [138]. Although the notation used at this stage may seem abstruse, it has been chosen to ensure clarity and avoid any ambiguity in comparison to the upcoming section (5.2.2). In this manuscript, this method has been adapted for $^{88}$Sr, but it can be similarly applied to most alkaline-earth-like atoms [139].

**The dressed state**

With $\hat{\mu}$ the magnetic-dipole operator, the coupling matrix element between those states via a magnetic field **B** is

$$\Omega_B = \frac{\langle 2|\, \hat{\mu} \cdot \mathbf{B}\, |r\rangle}{\hbar} \tag{5.1}$$

An expression of the dressed state emerging from the interaction between $|2\rangle$ and $|r\rangle$ can be derived in the framework of the perturbation theory. With respect to $\left|\frac{\Omega_B}{\Delta}\right|$

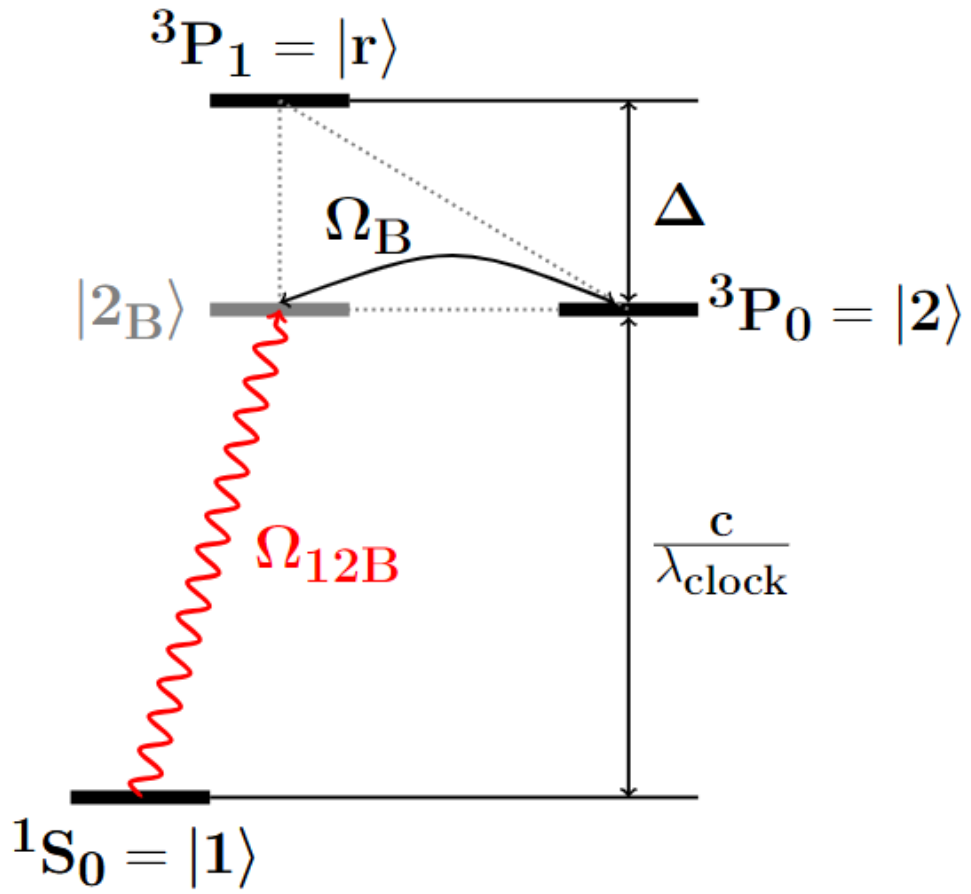


Figure 5.1: Level structure of strontium where a magnetic coupling generates a dressed state at resonance with the usual clock transition at $\lambda_{\text{clock}}$ = 698 nm. States $|1\rangle$ and $|2\rangle$ are the states of the clock transition, $|r\rangle$ the excited state of the red cooling transition and $|2_B\rangle$ the dressed state outcome of the admixture of $|r\rangle$ into $|2\rangle$. This coupling is at the Rabi frequency $\Omega_B$ and the interferometric laser (in red) couples $|2\rangle$ and the dressed state at the Rabi frequency $\Omega_{12B}$.

$$|2_B\rangle = |2\rangle + \frac{\Omega_B}{\Delta}|r\rangle \tag{5.2}$$

where $\Delta$ denotes the frequency split between $|2\rangle$ and $|r\rangle$. $\Delta = 2\pi\times$ 5.6 THz in the case of $^{88}$Sr [138].

Let us denote $|1\rangle$ as the ground state of the clock transition $^1S_0$. Although the direct transition $|1\rangle \rightarrow |2\rangle$ is strictly forbidden, by introducing an admixture of $|r\rangle$ in $|2\rangle$, an optical field can interact with the dressed state via the electric-dipole transition $|1\rangle \rightarrow |r\rangle$. The Rabi frequency of this transition is given by:

$$\Omega_r = \frac{\langle r|\, \hat{d} \cdot \mathbf{E}\, |1\rangle}{\hbar} \tag{5.3}$$

where $\hat{d}$ represents the electric-dipole operator, and **E** is the amplitude of the optical field driving the transition. For $^{88}$Sr, this transition occurs at 689 nm with a linewidth of $\Gamma_r = 2\pi \times 7.4$ kHz.

**Rabi frequency**

The frequency at which a resonance occurs while addressing the transition between the ground state and the dressed state with a laser field can be inferred by comparing the situation to a two-photon resonance. As the frequency of the magnetic field is zero, the frequency of the laser field driving $|1\rangle \rightarrow |2_B\rangle$ should be close to the frequency of $|1\rangle \rightarrow |2\rangle$, which corresponds to the usual clock transition at $\lambda_{\text{clock}} = 698$ nm. Given equations 5.2, 5.3 and considering the transition $^1S_0 \rightarrow {}^3P_0$ to be strictly forbidden, the Rabi frequency between the ground state and the dressed state can be written

$$\Omega_{12B} = \frac{\langle 2_B|\, \hat{d} \cdot \mathbf{E}\, |1\rangle}{\hbar} = \frac{\Omega_r \Omega_B}{\Delta} \tag{5.4}$$

This equation can be modified to yield an expression of the Rabi frequency in term of the experimentally pertinent parameters which are the laser intensity and the amplitude of the magnetic field

$$\Omega_{12B} = \alpha \sqrt{I} |B| \cos\theta \tag{5.5}$$

where $I$ denotes the laser intensity, $\theta$ the angle between **E** and **B** linearly polarized and the constant $\alpha$ equal to $2\pi \times 198$ Hz/(TmW$^{1/2}$cm$^{-1}$) for $^{88}$Sr [153].

Therefore, theoretically a Rabi frequency of $\Omega_{12B} = 2\pi \times 1$ kHz can be achieved with a laser intensity of I = 20 W/cm$^2$ and a magnetic field of 360 G. Experimentally, a Rabi frequency of $\Omega_{12B} = 2\pi \times 753$ Hz was observed with a laser intensity of I = 20 W/cm$^2$ and a magnetic field of 330 G [154].

**Effective linewidth**

As the probability of decaying from $|2\rangle$ to $|1\rangle$ is virtually zero, the linewidth of the dressed

state can be reduced to the linewidth of the transition $|1\rangle \rightarrow |r\rangle$ weighted by the probability $|\langle r|2_B\rangle|^2$ of finding an atom in $|r\rangle$ from the dressed state. Therefore, the linewidth of the dressed state $\Gamma_{2B}$ can be written as

$$\Gamma_{2B} = \Gamma_r |\langle r|2_B\rangle|^2 = \Gamma_r \left|\frac{\Omega_B}{\Delta}\right|^2 \tag{5.6}$$

Power broadening is neglected here.

Using equations 5.6, it is possible to achieve a natural linewidth of $2\pi\times$ 1 mHz, which is equivalent to the linewidth of the clock transition of $^{87}$Sr, by applying a magnetic field of 2 kG on $^{88}$Sr. This calculation relies on the assumption that $\langle 2|\,\hat{\mu}\,|r\rangle = \sqrt{2/3}\mu_B$, which is the case for bosonic alkaline-earth-like elements [138].

### 5.2.2 Coherence manipulation using an electromagnetic field

The concept of dressing a bosonic alkaline-earth-like atom with a laser field to interact with its clock transition was proposed before the method involving a magnetic field [155]. However, the latter method was favored by the atomic clock community because of its stability and simplicity.

Nevertheless, utilizing a laser field to address a sample of bosonic alkaline-earth-like atoms allows us to take advantage of its rapid switching capability. This feature is particularly beneficial in experiments where precise and controlled manipulation of the atomic states is required.

The approach presented in this work is not the sole method available for addressing the clock transition of even alkaline-earth-like atoms using a laser field. In 2007, Ovsiannikov *et al.* proposed an alternative technique involving a circularly polarized laser beam tuned at the "magic" wavelength to mix $^3P_0$ and $^3P_1$ states [156]. However, the focus of this section will be on the method described by Santra *et al.* in their work [155].

#### The dressed state

The primary theoretical distinction between dressing with a laser and dressing with a magnetic field lies in the nature of the interaction. The method proposed here utilizes a laser field, whose frequency is tuned to address a transition in a resonant process, allowing for

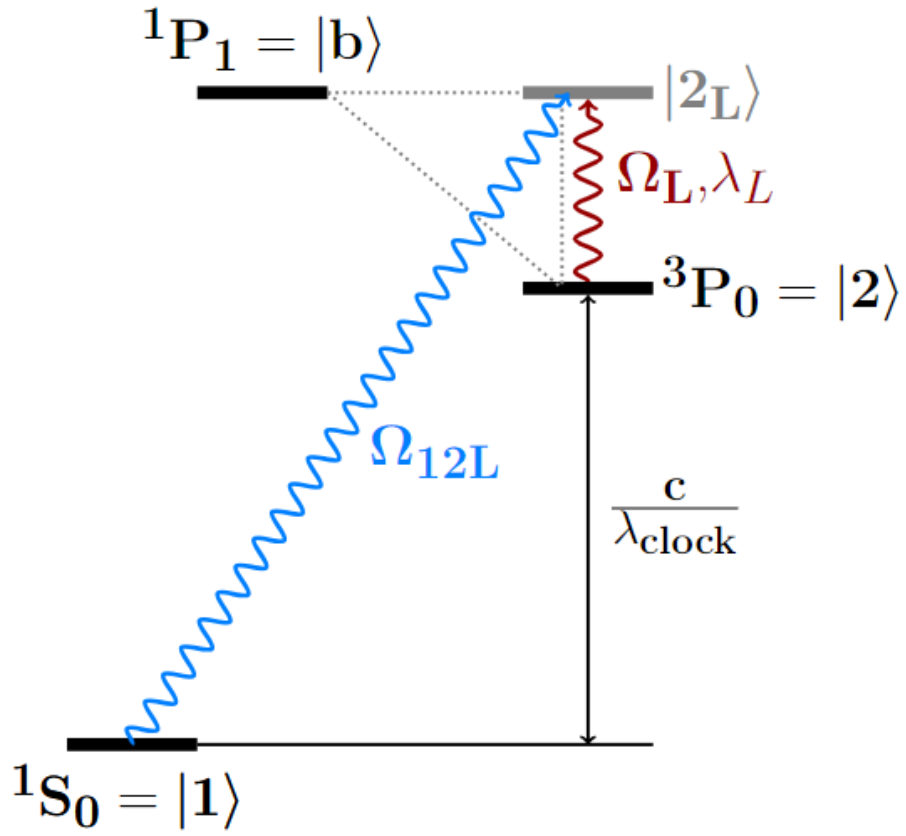


Figure 5.2: Level structure of strontium where a laser coupling generates a dressed state at resonance with the blue transition at 451 nm. States $|1\rangle$ and $|2\rangle$ are the levels of the clock transition, $|b\rangle$ the excited level of the blue cooling transition and $|2_L\rangle$ the dressed state outcome of the admixture of $|b\rangle$ into $|2\rangle$. This coupling at the wavelength 1354 nm is at the Rabi frequency $\Omega_L$ and the interferometric laser (in blue) couples $|2\rangle$ and the dressed state at the Rabi frequency $\Omega_{12B}$.

a more flexible choice of intermediate states. In contrast, when dressing with a magnetic field, the process is not resonant, and the frequency difference between states becomes a critical consideration. Dressing using a laser field, as long as the laser frequency is technically feasible, the frequency difference between states is no longer a limiting factor.

Hence, the excited state of the blue cooling transition $^1P_1$ can be effectively employed due to its relatively larger natural linewidth compared to the red cooling transition, denoted as $\Gamma_b = 2\pi \times 30.5$ MHz. This state will be referred to as $|b\rangle$, and the laser coupling $|2\rangle$ with $|b\rangle$ is achieved using a wavelength of $\lambda_L = 1354$ nm.

The atomic sample interacts with the electromagnetic field via the magnetic component whose amplitude is denoted $\mathcal{B}_0$. Therefore the Rabi frequency between $|2\rangle$ and $|b\rangle$ is written

$$\Omega_L = \frac{\langle b| M_0 |2\rangle \mathcal{B}_0}{\hbar} \tag{5.7}$$

where $M_0$, the magnetic dipole, verifies $|\langle b| M_0 |2\rangle| = 0.022\mu_B$ [155].

In terms of notation, when referring to dressing with a static magnetic field, it is denoted as B, whereas dressing with an electromagnetic field is represented by L. This distinction helps to differentiate between the two methods in discussions and equations.

In contrast to the previous section (5.2.1), the dressing process in this case is resonant. As a result, the frequency detuning cannot be used in perturbation theory. Instead, the calculations are performed with respect to the parameter $\frac{\Omega_L}{\Gamma_b}$, considering the large linewidth of $|1\rangle \rightarrow |b\rangle$. This leads to a dressed state given by the following expression

$$|2_L\rangle = |2\rangle + \frac{\Omega_L}{\Gamma_b} |b\rangle \tag{5.8}$$

No detuning is assumed in this section but a more precise description can be found in the appendix.

We introduce the Rabi frequency of the blue cooling transition

$$\Omega_b = \frac{\langle b| D_0 |1\rangle \mathcal{E}_0}{\hbar} \tag{5.9}$$

$D_0$ is the electric-dipole coupling $|1\rangle$ and $|b\rangle$ and $\mathcal{E}_0$ the amplitude of the electric field.

**Rabi frequency**

A similar reasoning as the one presented in section 5.2.1 can be applied to determine the resonance frequency between the ground states and the dressed state. By adding the frequency of a photon at 698 nm to the frequency of a photon at 1354 nm, we obtain a resonance at 461 nm, which corresponds to the frequency of the blue cooling transition.

The Rabi frequency coupling the ground state and the dressed state is then

$$\Omega_{12L} = \frac{\langle 2_L| D_0 |1\rangle \mathcal{E}_0}{\hbar} = \frac{\Omega_b \Omega_L}{\Gamma_b} \tag{5.10}$$

Expressed in terms of experimentally relevant quantities, the dressed state can be represented as

$$\Omega_{12L} = \beta\sqrt{I_b}\sqrt{I_L} \tag{5.11}$$

where $I_b$ and $I_L$ are the intensities of the interferometric laser and the dressing laser respectively. The constant $\beta$ is equal to $2\pi\times5.25\times10^{-2}$ Hz/(W.m$^{-2}$). Assuming both laser intensities to be equal to 20 W/cm$^2$, the resulting Rabi frequency is approximately $2\pi\times$ 10 kHz.

**Effective linewidth**

The method used in the previous section (5.2.1) to estimate the linewidth of the dressed state remains applicable here. The linewidth of the transition $|1\rangle \rightarrow |b\rangle$, weighted by the probability $|\langle b|2_L\rangle|^2$ of finding an atom in $|b\rangle$ from the dressed state, is given by

$$\Gamma_{2L} = \Gamma_b|\langle b|2_L\rangle|^2 = \frac{\Omega_L^2}{\Gamma_b} \tag{5.12}$$

For comparison purposes, a linewidth of $2\pi\times$ 1 mHz, which is the natural linewidth of the clock transition of $^{87}$Sr, can be achieved with a dressing laser intensity of 1.3 W/cm$^2$.

### 5.2.3 Applications for atomic physics

As mentioned in the previous section, the method involving a static magnetic field has been favored by the atomic clock community due to its stability and simplicity. With this method, only the amplitude of a static magnetic field needs to be controlled. On the other hand, stabilizing a laser requires the control of multiple parameters, such as its intensity, frequency, phase, and polarization.

However, modifying the coherence of transitions has broader implications across various fields. In the context of quantum computing, where the lifetime of qubits is of utmost importance [157], dynamically interacting with an atomic state thanks to an effective linewidth created on a specific transition can significantly enhance the coherence of the system. The version employing a laser field is particularly well-suited for this application due to its rapid switching capability.

The pioneering atomic interferometer based on $^{88}$Sr was successfully demonstrated in

2017 by Hu *et al.* [154]. In this experiment, an ensemble of approximately $10^4$ atoms was subjected to a $\pi/2$ - $\pi$ - $\pi/2$ interferometric sequence whose laser intensity is 20 W/cm$^2$ and dressed with a static magnetic field of 330 G. Notably, a Rabi frequency of $2\pi\times753$ Hz was observed for a total interferometer time of approximately 10 ms. The realization of this interferometer marks the first atomic interferometer using $^{88}$Sr. The concept presented in the following sections of this chapter is also based on this isotope but involves a laser induced dressed state. Such a scheme also circumvents some issues inherent to cavity based intererometers.

## 5.3 Atomic interferometry in a cavity

In a two mirrors optical cavity the resonant photons of the intra-cavity laser field undergo constructive interference, resulting in a standing wave pattern. The relationship governing the wavelength $\lambda$ of this standing wave is dictated by the condition of resonance, expressed as:

$$\lambda = \frac{2L}{n} \tag{5.13}$$

where $L$ is the cavity length and $n$ the integer referring to the mode number.

The motivations to build atomic interferometers in cavities stem from the properties of these standing waves.

### 5.3.1 Motivations for cavity based atomic interferometer

From a fundamental standpoint, the phase of the laser field significantly influences the phase of the atomic wavefunction [144, 145]. By employing an optical cavity, the phase imprinting is no longer governed by the laser fluctuations; instead, it becomes contingent on the precise positioning of the mirrors. As a result, this approach offers meticulous control over the characteristics of the atomic wavefunction.

Nevertheless, today, cavities are used in atomic interferometry for the technical advantage they generate.

**Mode cleaning**

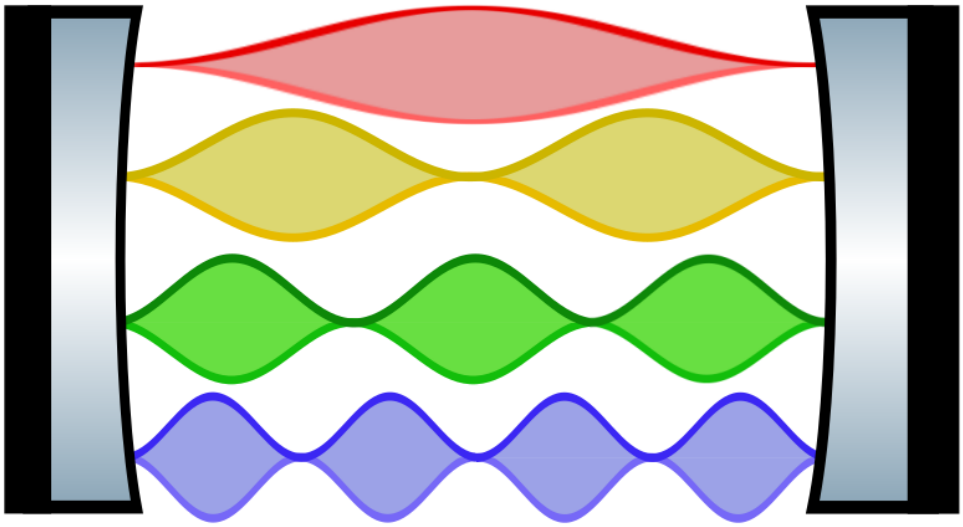

Figure 5.3: The Fabry-Perot resonance condition selects specific modes and enhances the intensity of the laser field within the cavity, while the other modes vanish due to destructive interference. The figure displays the first four spectral modes of a Fabry-Perot cavity.

In each round trip within the cavity, the laser field undergoes self-interference, leading to the emergence of a pure single mode. Undesired frequencies that are non-resonant with the cavity are efficiently filtered out through destructive interference. Consequently, achieving a higher finesse for the cavity allows for superior mode cleaning while preserving essential field properties such as polarization or wave vector [158].

As any undesirable fluctuations in the amplitude or phase of the laser can adversely affect the interferometer's contrast, employing an optical cavity offers the advantage of filtering the interferometric beam mode and generating a clean, well-defined wavefront [159] determined by the cavity's properties [160].

In various interferometric schemes, multiple laser beams are involved, necessitating precise control over their relative alignment. Utilizing the multiple spatial modes of an optical cavity enables self-alignment of the laser beams, simplifying the setup and reducing alignment-related challenges [161].

The coupling between the atomic sample and the intracavity laser mode has been harnessed to enhance the detection sensitivity of an atomic interferometer beyond the shot noise limit [162].

**Power enhancement**

The power confined inside the cavity is given by the expression

$$P_{\text{intra}} = P_{\text{in}} \frac{(1 - r_1^2)}{(1 - r_1 r_2)^2} \tag{5.14}$$

where $P_{\text{in}}$ represents the input power, and $r_1$ and $r_2$ denote the reflectivity of the two mirrors of the cavity [163].

Hence, even with an input power as low as 100 $\mu$W and a cavity with a finesse $\mathcal{F} = 1000$, the power confined inside the cavity can reach 16 mW. This substantial increase in power within the cavity facilitates various applications, such as enhancing the sensitivity of atomic interferometry and enabling more precise measurements in experiments utilizing high-finesse optical cavities.

In multi-photon Bragg interferometry, the contrast of the interferometer can be significantly improved, as demonstrated in previous works [164, 165]. The phase measured by the interferometer is enhanced by a factor of n$\hbar$k, where n represents the number of photons and k is the wave vector of the laser field. However, this improvement comes at the cost of requiring a high laser power, which may not always be readily available in certain experimental setups [166].

The use of an optical cavity provides a solution to this issue by substantially enhancing the power of the laser confined inside the cavity. This allows for the implementation of a multi-photon Bragg interferometer intra-cavity, enabling improved contrast and sensitivity without the need for prohibitively high laser powers [158].

### 5.3.2 The MIGA project

The historic detection of gravitational waves (GWs) in September 2015 by the laser-based interferometers of the Laser Interferometer Gravitational-Wave Observatory (LIGO) represented a groundbreaking moment in scientific exploration. It opened up an entirely new frontier in physics, with GW detectors providing unparalleled potential to reveal previously unexplored facets of massive astrophysical objects. This includes gaining profound insights into the intricate properties and dynamic behaviors of celestial entities like neutron stars,

black holes, and other enigmatic astronomical phenomena.

The operational bandwidth of the LIGO interferometer is confined to a specific frequency range of 10 Hz to 10 kHz. Consequently, this restricts the sensitivity to only a fraction of the gravitational waves emitted by celestial sources. To address this limitation, researchers are exploring low-frequency detectors. These detectors are capable of capturing and identifying signals originating from such sources well before they enter the bandwidth range of ground-based optical detectors. More importantly, these low-frequency detectors can also identify signals that would not be detectable by LIGO-like detectors. This distinct advantage grants the opportunity for early observation and in-depth study of the phenomena under investigation.

The Matter wave-laser based Interferometer Gravitation Antenna (MIGA) project, established jointly between the LP2N (Laboratoire Photonique, Numérique et Nanosciences) in Bordeaux, France, and the LSBB (Laboratoire Souterrain à Bas Bruit) in Rustrel, France, endeavors to validate and showcase the capability of a GW detector operating within the frequency range of 100 mHz to a few Hz. This ambitious project relies on the implementation of atomic interferometry techniques within a long baseline optical cavity to achieve precise and sensitive measurements of GW signals [167].

**The interferometer**

The MIGA setup comprises three atomic sensors, each designed to interact with resonant laser pulses while situated within a long stable optical cavity. The primary goal of this configuration is to detect and analyze potential gravitational waves that might alter the local inertial forces experienced by the atoms. Consequently, the interferometer's response is affected, and through the utilization of multiple atomic sensors, the correlations between their respective measurements under the influence of such gravitational perturbations can be precisely determined. MIGA will exhibit a sensitivity six orders of magnitude away from what is required for GW detection, but it is a demonstrator for the proposed method [53, 168].

The gravitational antenna, in this research project, is constructed around an optical resonator with a length L of 200 meters, exhibiting a finesse of $\mathcal{F} = 100$. This innovative setup involves three distinct clouds of rubidium (Rb) atoms, which are subjected to Rabi evolution at a frequency of 10 kHz, employing the $D_2$ line at 780 nm. The entire interferometric

process spans a total time of 2T = 500 milliseconds. This PhD project is primarily focused on exploring the possibility of replacing the rubidium atoms with strontium (Sr) atoms in a future version of the gravitational antenna, potentially yielding enhanced performance and contributing to future advancements in this domain.

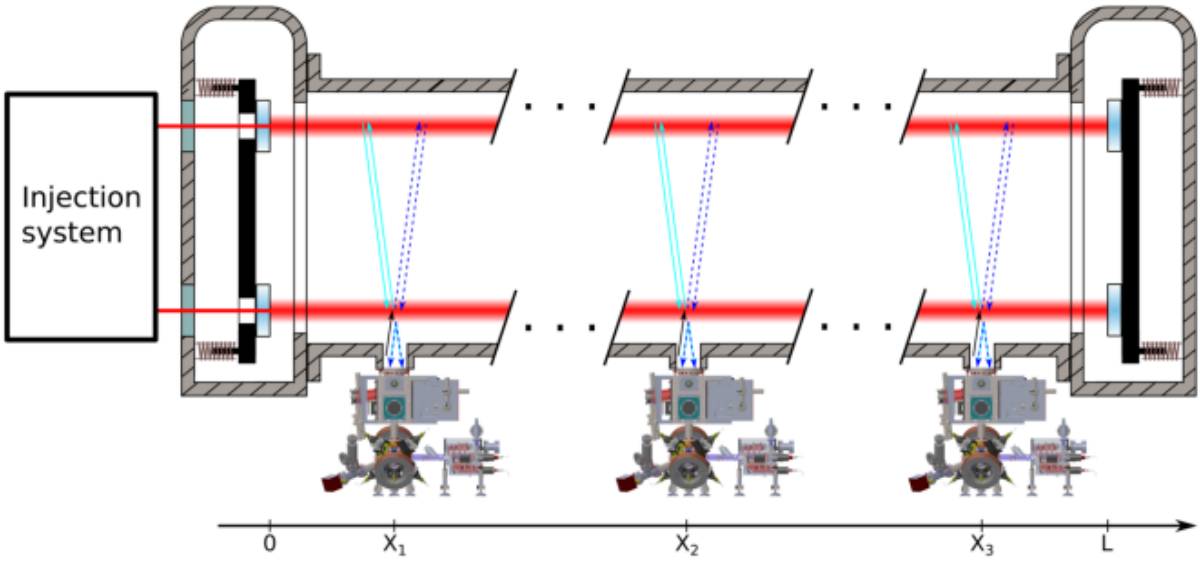


Figure 5.4: Overview of the MIGA instrument. Three atomic heads generate a flux of cold Rb atoms undergoing a Bragg interferometric sequence via the laser field coupled in two different cavities. The lower cavity interacts via $\pi/2$ pulse and the upper cavity via a $\pi$ pulse [158].

The gravitational antenna serves not only as a tool for GW detection but also as a promising instrument in the field of geoscience [169]. By utilizing atomic interferometry, this setup provides an opportunity to accurately map the distribution of mass in the vicinity of the detector. This capability opens up avenues for probing and understanding the underlying geological structures and variations in the Earth's gravitational field, which can significantly contribute to advancements in geophysical research and exploration [170].

**The cavity**

Indeed, the intricate setup of the MIGA project consists not of a single cavity, but two parallel, vertically displaced optical cavities, each spanning a length of 150 m. The operation of this system relies on an orchestrated $\pi/2$ - $\pi$ - $\pi/2$ Bragg sequence, which effectively interacts with the atomic clouds. The fundamental principle guiding this sequence involves a series of steps: first, the lower cavity splits the atomic wave packet through a $\pi/2$ pulse; subsequently,

the upper cavity redirects the wave packets using a $\pi$ pulse; and finally, the $\pi/2$ pulse in the lower cavity recombines the separated wave packets. The vertical separation of the cavity (30 cm) determines the time interval between the pulses.

Within each of the cavities, the atoms are coupled with the laser field, ensuring that the interaction occurs precisely on the fundamental transverse mode $TEM_{00}$. Pulses of the appropriate duration are emitted as the atom clouds traverse the center of the resonators. This strategic coupling of the atomic clouds with the laser field within the two cavities is pivotal to the successful operation of the interferometer, allowing for precise manipulation and control of the atomic wave packets and enabling high-precision measurements.

The imprinting of the optical phase on the atomic wavefunction, renders the atoms highly susceptible to variations in the positions of the mirrors. Consequently, any vibrational noise that perturbs the positions of the mirrors also impacts the response of the interferometer. However, this perturbation can be attenuated in a gravity-gradiometer configuration. This susceptibility to mechanical perturbations poses a significant challenge in maintaining the required stability and precision of the interferometric measurements.

Moreover, in the context of high finesse cavities, shorter linewidths are associated with longer temporal responses. This relationship poses limitations on the overall efficiency of the interferometer [158].

### 5.3.3 Residual field induced by cavity finesse on clock laser pulses

In an optical cavity, a higher finesse leads to a more pronounced interference of the laser field with itself. Consequently, an increased finesse of the cavity corresponds to a broader distribution of the laser pulse.

The time required for the laser intensity to decrease by a factor of 1/e inside the cavity is given by $\tau = \dfrac{L\mathcal{F}}{\pi c}$ [159].

Regardless of how quickly the injection cavity is switched on or off, the pulse duration inside the cavity is determined by the characteristics of the cavity itself. This means that the cavity imposes a specific timescale for the laser pulse.

The pulse deformation operated by the optical resonator is the reason why, despite the

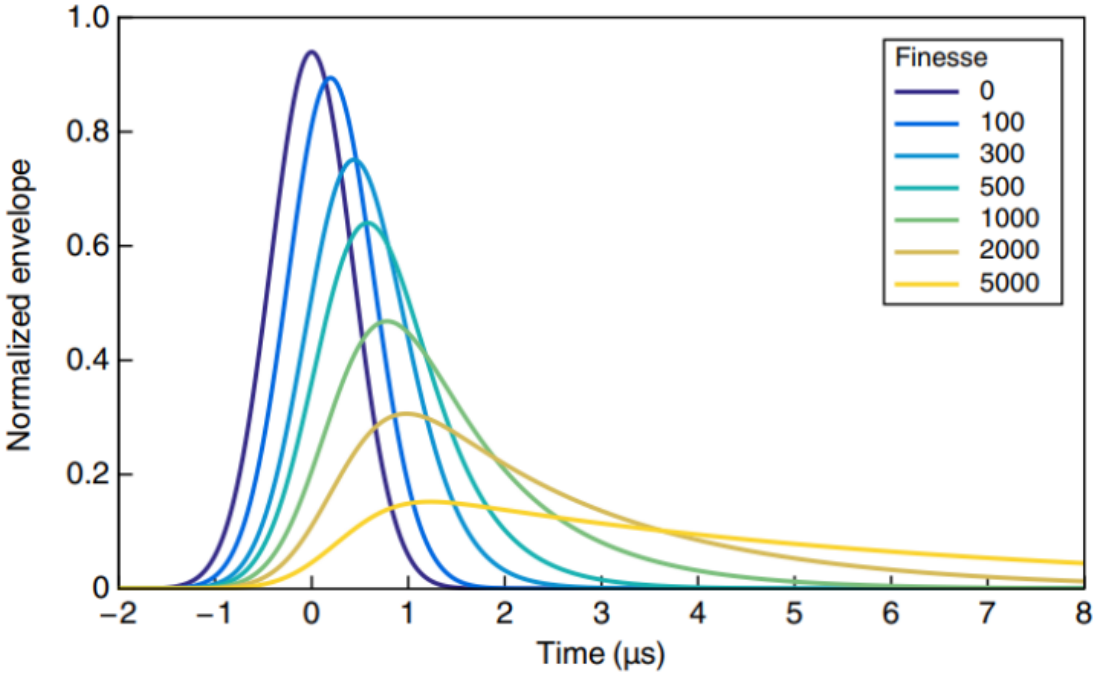


Figure 5.5: Deformation of a $\mu$s pulse induced by a cavity of a 1 m long for various finesse values. The areas are normalized to the input pulse. Extracted from [159].

significant advantages offered by the use of a high finesse cavity for atomic interferometry, only a limited beam splitting of up to $8\hbar$k has been experimentally demonstrated [158].

Until recently, the beam splitting limitation in a high finesse cavity for atomic interferometry has been considered a fundamental constraint. However, a recent proposition in 2021 by our research group presented a method to overcome this issue [171]. In order to prevent pulse distortion caused by the cavity, we opted a different approach where the interferometric laser is maintained at a constant intensity without pulsed operation. Instead, an external laser field is utilized to dress the atoms, altering their resonance condition with the atomic ensemble. The wavelength of this external laser field was systematically investigated within the range of 380 nm to 740 nm to achieve an AC Stark shift on the clock transition [171]. This technique shows great potential for enhancing the capabilities of atomic interferometry with high finesse cavities. Another method has been proposed by Nourshargh *et al.* employing a circulating pulse cavity, promising a splitting of up to $10^4\hbar$k [172].

The scheme we proposed offers the advantage of fully exploiting the benefits provided by the cavity without the need to relock the interferometric laser beam to the cavity. No-

tably, although the scheme is currently based on the isotope $^{87}$Sr, its versatility allows for adaptation to various other atomic elements. The potential applicability to different isotopes broadens the scope of its usage and opens up new opportunities for advancements in atomic interferometry.

Nevertheless, the proposed scheme utilizing the AC stark effect for dressing the atomic ensemble requires a candidate isotope with a clock transition that is already sufficiently large to effectively interact with a laser field. Unfortunately, the isotope $^{88}$Sr does not fulfill this requirement, as the linewidth of its clock transition is too narrow to interact with the dressing laser. Consequently, $^{88}$Sr all related properties cannot be employed in this type of dressing scheme.

In the subsequent section, we shall leverage the insights described in Section 5.2 to integrate $^{88}$Sr into a cavity based interferometer.

### 5.3.4 The first $^{88}$Sr based atomic interferometer in a high finesse cavity

The proposed approach bears some resemblance to the methodology presented in [171]; however, it entails manipulating the coherence of $^{88}$Sr's clock transition differently. Instead of relying on the AC Stark effect to shift the atomic levels out of resonance with the interferometric beam, we introduce a combination of the $^1P_1$ state and the upper state of the clock transition, denoted as $|2\rangle$, through the application of a dressing laser at 1354 nm [155]. This novel strategy seeks to investigate the viability and implications of utilizing $^{88}$Sr in the interferometer setup.

**Principle**

In this scheme, the interferometric laser is always resonant with the atoms, and its intensity remains constant over time. The manipulation of atomic wave functions through $\pi$ and $\pi/2$ pulses is achieved by switching the dressing laser field on and off. Consequently, the atoms experience pulses as short as those observed in an interferometer without a cavity. The utilization of the cavity does not distort the pulse duration, and this feature allows us to take full advantage of the benefits provided by the high finesse cavity without the need to relock the interferometric laser beam to the cavity.

In this setup, the dressing laser interacts with the atomic wave packet through its magnetic component, contributing one M1 (magnetic dipole) photon to the transition. On the other hand, the interferometric laser adds one E1 (electric dipole) photon via its electric component. To ensure proper interaction, the polarizations of the two laser fields need to be adjusted such that the electric component of the interferometric laser aligns with the magnetic component of the dressing laser. The interferometric laser is coupled to the cavity, and the dressing laser can be aligned freely, as long as the polarization condition is satisfied. It can be aligned to the interferometric laser beam (thus not coupled to the cavity) or orthogonal to the axis of the cavity. By controlling the polarizations, the dressing laser effectively manipulates the atomic wave functions without introducing pulse distortions due to the cavity, as described earlier.

**Rabi frequency**

With the interferometric laser field resonant with the clock transition, the dressing laser field solely impacts the Rabi frequency of the clock transition. When the dressing laser is on, the Rabi frequency is governed by equation 5.11, allowing coherent manipulation of the atomic wavefunction. However, when the dressing laser is turned off, the Rabi frequency becomes virtually zero, effectively leaving the atomic wavefunction unchanged. This selective control of the Rabi frequency allows a precise and efficient manipulation of the atomic coherence in the interferometer.

Supposing equal intensities of both lasers, a Rabi frequency of $2\pi \times 10$ kHz can be achieved with 20 W/cm$^2$ for each laser beam. While this Rabi frequency is sufficient for many applications, increasing the laser intensity significantly to achieve a higher Rabi frequency would indeed present some challenges, particularly in the blue domain as the transition between the ground state and the dressed state is at 461 nm.

However, addressing the transition between the ground state and the dressed state at resonance presents a significant drawback of also addressing the blue cooling transition. This phenomenon leads to the heating of the atomic cloud on the order of millikelvins (the temperature of a blue MOT).

This issue can be circumvented by detuning both laser frequencies, a common approach used for Raman transitions. In this context, if the wavelength of the interferometric laser $\lambda_i$

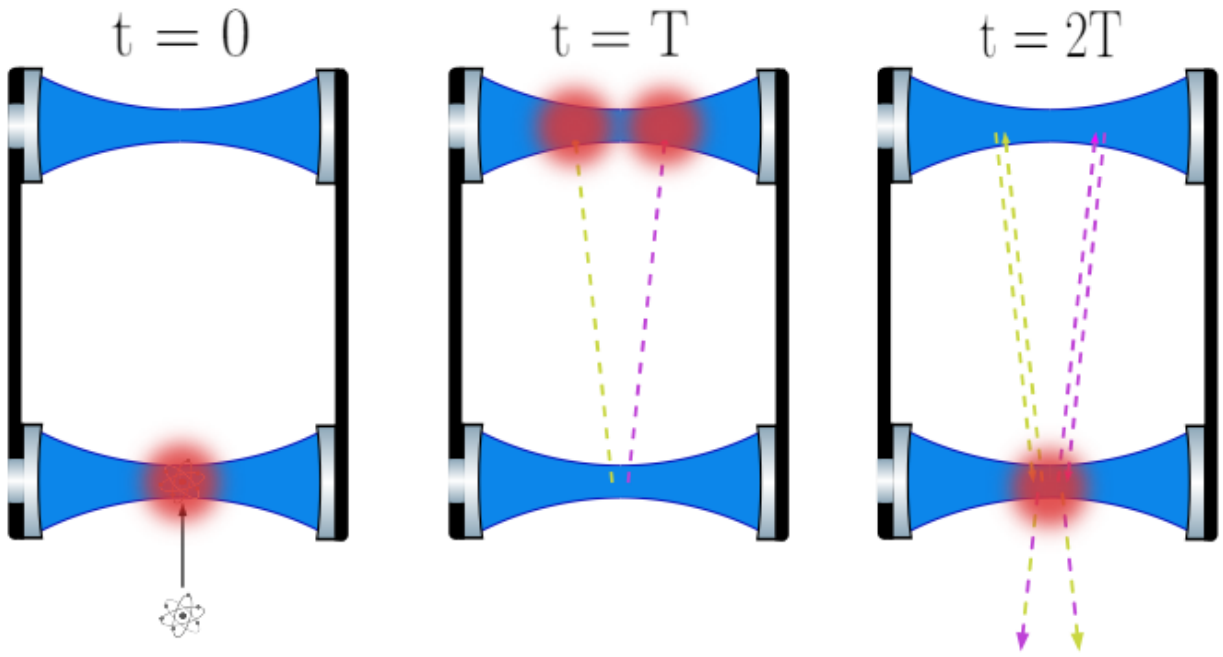


Figure 5.6: Scheme comprising two cavities separated (along the y-axis in his figure) to embrace the three interferometric stages. At t = 0, the sample of $^{88}$Sr initially in state $|1\rangle$ does not interact with the laser field intra-cavity at 461 nm (represented in blue). A dressing laser at 1354 nm (in red) is directed onto the atomic cloud in the lower cavity to enable the interaction between the atoms and the interferometric laser. The dressing laser is switched on and off, producing a $\pi/2$ pulse that splits the wave packet into two paths (one in yellow, the other in purple). At t = T a similar scheme is implemented in the upper cavity to generate a $\pi$ pulse that reverses the atomic paths, directing them back towards the lower cavity. At t = 2T, in the lower cavity, the dressing laser is again switched on and off a last time to produce a final $\pi/2$ pulse, resulting in the recombination of the wave packets.

continues to satisfy the relationship

$$\frac{1}{\lambda_i} = \frac{1}{\lambda_L} + \frac{1}{\lambda_{\text{clock}}} \tag{5.15}$$

where $\lambda_L$ is the wavelength of the dressing laser and $\lambda_{\text{clock}}$ is the wavelength of the clock laser, then the coherent process between states $|1\rangle$ and $|2\rangle$ can still be achieved while mitigating the interaction with the blue cooling transition.

The Rabi frequency between $|1\rangle$ and $|2_L\rangle$ becomes

$$\Omega_{12L} = \frac{\Omega_L \Omega_b}{\sqrt{4\delta^2 + \Gamma_b^2}} \tag{5.16}$$

where $\delta$ represents the detuning between the laser frequency and state $|b\rangle$ (assumed to be

identical for both lasers).

The maximum transition probability for an atom to be in the excited state $|b\rangle$ from the initial state $|1\rangle$ is given by [15]

$$P_{1\to b} = \frac{\Omega_{12L}^2}{\Omega_{12L}^2 + \delta^2}. \tag{5.17}$$

Due to the dependence of the Rabi frequency with $1/\delta$ and the fact that the probability of interaction with the excited state varies as $1/\delta^2$, allowing for a trade-off to be achieved.

With a detuning of $\delta = 3 \times 10^{10}$ Hz, the maximum transition probability is only 1%. However, this detuning causes the Rabi frequency to decrease significantly, reaching as low as 200 Hz. Other configurations, such as varying the balance between the intensities of the beams or involving other three-level systems, will be investigated.

It is worth noting that an alternative method exists, which employs not two, but three photons in the process [173]. This particular scheme, centered around a resonance at the frequency of the red cooling transition, does not permit the introduction of a detuning between the laser frequencies and the atomic states, as described above.

# Conclusion

In this manuscript, an exploration of atomic interferometry and the motivations behind the selection of alkaline-earth-like atoms for experimental investigations has been elucidated in **Chapter 1**.

Subsequent to an exposition of strontium and its manifold applications within the scientific community, **Chapter 2** delineated an elaborate account of its atomic characteristics and the methodologies employed in harnessing them for the creation of cold atomic ensembles.

**Chapter 3** was dedicated to the exposition of the experimental setup. This encompassed a depiction of the laser systems and electronic components deployed, alongside the procedures employed to ensure laser frequency stabilization and the generation of magnetic fields essential for the realization of magneto-optical traps centered around strontium.

**Chapter 4** was dedicated to an exposition of the newly developed Zeeman Slower. Following an introduction to the fundamental concept of atom deceleration through the utilization of the Zeeman effect, the chapter delved into a depiction of a Zeeman Slower interacting with a wide range of atomic velocity classes. Notably, an upgraded version of the Zeeman Slower, incorporating the use of dual laser frequencies, was analyzed.

Conclusively, **Chapter 5** undertook an investigation into the salient attributes of strontium's isotope 88, particularly in the context of atomic interferometry. Furthermore, the chapter expounded upon the potential advantages presented by optical cavities for atomic interferometric, while also delving into their inherent limitations. Notably, the final section of this chapter introduced an innovative scheme for a cavity-based atomic interferometer, harnessing the unique qualities of $^{88}$Sr while circumventing the challenges associated with cavity-based systems.

# Appendix

## I Toolbox

### Perturbation theory

This section aims to provide the fundamental elements necessary to quantitatively determine the decomposition of a dressed state onto the eigenstate basis. A more complete treatment of the subject can be found in [15].

We consider a 2-level system coupled by a monochromatic electromagnetic field. The system is described by the Hamiltonian

$$\hat{H} = \hat{H}_0 + \hat{H}_1(t) \tag{18}$$

$\hat{H}_0$ is the Hamiltonian independent of the perturbation

$$\hat{H}_0 |n\rangle = E_n |n\rangle \tag{19}$$

and $\hat{H}_1$ the interaction Hamiltonian whose terms are considered to be small compare to the energy difference of the system. Therefore, it can be written

$$\hat{H}_1 = \lambda \hat{H}_1' \tag{20}$$

where $\lambda$ is a real scalar such that $\lambda \ll 1$. Thus, $\hat{H}_0$ and $\hat{H}_1'$ are of the same order of magnitude.

This expression of $\hat{H}$ in the Schrödinger equation yields

$$i\hbar \frac{d}{dt} |\psi(t)\rangle = (\hat{H}_0 + \lambda \hat{H}_1'(t)) |\psi(t)\rangle \tag{21}$$

Using the basis of eigenstates of $\hat{H}_0$ and by decoupling the amplitude of probability $c_n$ to the Feynman propagators, the state $|\psi(t)\rangle$ can be expressed as

$$|\psi(t)\rangle = \sum_n c_n(t) e^{-iE_n t/\hbar} |n\rangle \tag{22}$$

This expression of the wave function in (21) yields $\forall k \in \mathbb{N}$

$$i\hbar \frac{d}{dt} c_k(t) = \lambda \sum_n \langle k| \hat{H}_1'(t) |n\rangle e^{i(E_k - E_n)t/\hbar} c_n(t) \tag{23}$$

No approximation has been made until now. The principle of the perturbation theory is to expand each amplitude of probability with respect to $\lambda$

$$c_k(t) = c_k^{(0)}(t) + \lambda c_k^{(1)}(t) + \lambda^2 c_k^{(2)}(t) + ... \tag{24}$$

A term to term comparison yields

- to order 0

$$i\hbar \frac{d}{dt} c_k^{(0)}(t) = 0 \tag{25}$$

- to order 1

$$i\hbar \frac{d}{dt} c_k^{(1)}(t) = \sum_n \langle k| \hat{H}_1' |n\rangle e^{i(E_k - E_n)t/\hbar} c_n^{(0)}(t) \tag{26}$$

- to order r

$$i\hbar \frac{d}{dt} c_k^{(r)}(t) = \sum_n \langle k| \hat{H}_1' |n\rangle e^{i(E_k - E_n)t/\hbar} c_n^{(r-1)}(t) \tag{27}$$

The $0^{th}$ order is a constant in this formalism and thus, is fully determined by the initial conditions. It can be used to determine the $1^{st}$ order that can be used to determine the $2^{nd}$ order ect... Thereby, iteratively, every term of the decomposition can be computed. As far as the assumption $\lambda \ll 1$ is verified, a solution of the wavefunction can be computed.

## The Feynman propagator

In the Schrödinger representation, one can describe a particle as $|\psi(t)\rangle$ following the Schrödinger equation

$$i\hbar \frac{d}{dt} |\psi(t)\rangle = \hat{H} |\psi(t)\rangle \tag{28}$$

Assuming $\hat{H}$ independent of time and starting from a time $t_0$, for $t > t_0$ the wave-function can be written as

$$|\psi(t)\rangle = e^{-i\hat{H}*(t-t_0)/\hbar} |\psi(t_0)\rangle \tag{29}$$

The product symbol $'*'$ will be used in this subsection and it shall not be confused with the Hamiltonian evaluated at the time $t - t_0$: $H(t - t_0)$ to the constant Hamiltonian $H$ multiplied by $t - t_0$: $H * (t - t_0)$

In the basis of positions

$$\langle r|\psi(t)\rangle = \langle r| e^{-i\hat{H}*(t-t_0)/\hbar} |\psi(t_0)\rangle \tag{30}$$

and using the closure relation

$$\int |r_0\rangle \langle r_0| dr_0 = 1 \tag{31}$$

the quantity $\langle r|\psi(t)\rangle$ can be written as

$$\langle r|\psi(t)\rangle = \int \langle r| e^{-i\hat{H}*(t-t_0)/\hbar} |r_0\rangle \langle r_0|\psi(t_0)\rangle dr_0 \tag{32}$$

This relation can be expressed with $\psi(r,t) = \langle r|\psi(t)\rangle$

$$\psi(r,t) = \int \langle r| e^{-i\hat{H}*(t-t_0)/\hbar} |r_0\rangle \psi(r_0,t_0) dr_0 \tag{33}$$

Therefore, $\langle r| e^{-i\hat{H}*(t-t_0)/\hbar} |r_0\rangle$ can be seen as the quantity guiding $\psi(r_0,t_0)$ to $\psi(r,t)$ and thus we define the propagator of the Schrödinger equation

$$K(r,t|r_0,t_0) = \langle r| e^{-i\hat{H}*(t-t_0)/\hbar} |r_0\rangle \tag{34}$$

such as

$$\psi(r,t) = \int K(r,t|r_0,t_0)\psi(r_0,t_0) dr_0 \tag{35}$$

We introduce the operator $\hat{U} = e^{-i\hat{H}*(t-t_0)/\hbar}$, which represents the time-dependent part of the propagator. Therefore, $K(r,t|r_0,t_0) = \langle r| \hat{U}(t,t_0) |r_0\rangle$, or more generally, $K = \langle Final| \hat{U} |Initial\rangle$.

With a time dependant Hamiltonian the relation must be adapted. Applying the propagator for short duration compared to the evolution of the system, $\hat{H}$ can be considered constant during $\delta$ and the operator takes the form

$$U(t+\delta,t) = e^{-i\hat{H}(t)*t/\hbar} \tag{36}$$

Then, the wavefunction becomes

$$|\psi(t)\rangle = \prod_n e^{-i\hat{H}(t_0+n\delta)*(t_0+n\delta)/\hbar} |\psi(t_0)\rangle \tag{37}$$

When $\delta \to 0$, it can be proved the product turns into an integral, leading to

$$U(t,t_0) = \exp\left\{-i\int_{t_0}^{t} \frac{\hat{H}(t)}{\hbar} dt\right\} \tag{38}$$

# II Coherence manipulation via a magnetic field

In this appendix, $|2\rangle$ corresponds to the excited state $^3P_0$ of the clock transition and $|r\rangle$ to the excited state $^3P_1$ of the red cooling transition. As the transition $|1\rangle \to |2\rangle$ is strictly forbidden, decaying from $|2\rangle$ to the ground state cannot be achieved without an external field. In this section, we consider a static magnetic field coupling $|2\rangle$ and $|r\rangle$. The results of this section can be found in [138].

The linewidth of the clock transition is estimated to be $5.5 \times 10^{-12} s^{-1}$ for $^{88}Sr$ [80], which is practically zero from the experimental point of view. The state effectively addressed is the state $|2_B\rangle$, outcome of the admixture of $|r\rangle$ in $|2\rangle$ via the magnetic field **B**. The frequency split between $|r\rangle$ and $|2\rangle$ is

$\Delta = 2\pi \times 5.6$ THz and their coupling represented by a matrix element

$$\Omega_B = \frac{\langle 2| \hat{\boldsymbol{\mu}} \cdot \mathbf{B} |r\rangle}{\hbar} \tag{39}$$

where $\hat{\mu}$ is the magnetic-dipole operator.

## The dressed state

The dressed state is derived applying the perturbation theory to the system being initially in state $|2\rangle$ under the influence of the magnetic coupling. Then the interaction between states $|1\rangle$ and $|2_B\rangle$ under an electromagnetic field is analysed.

Let's compute an order of magnitude of $\Omega_B$. Taking $|\mathbf{B}| = 35$mT and $\hat{\mu} = \mu_B = 9.3 \times 10^{-24}$ JT$^{-1}$ the Bohr magneton, $\Omega_B \approx \mu_B B/\hbar = 3.3 \times 10^9$ s$^{-1}$. The ratio $\dfrac{\Omega_B}{\Delta}$ is approximately

$$\lambda \equiv \frac{\Omega_B}{\Delta} \approx 10^{-4} \tag{40}$$

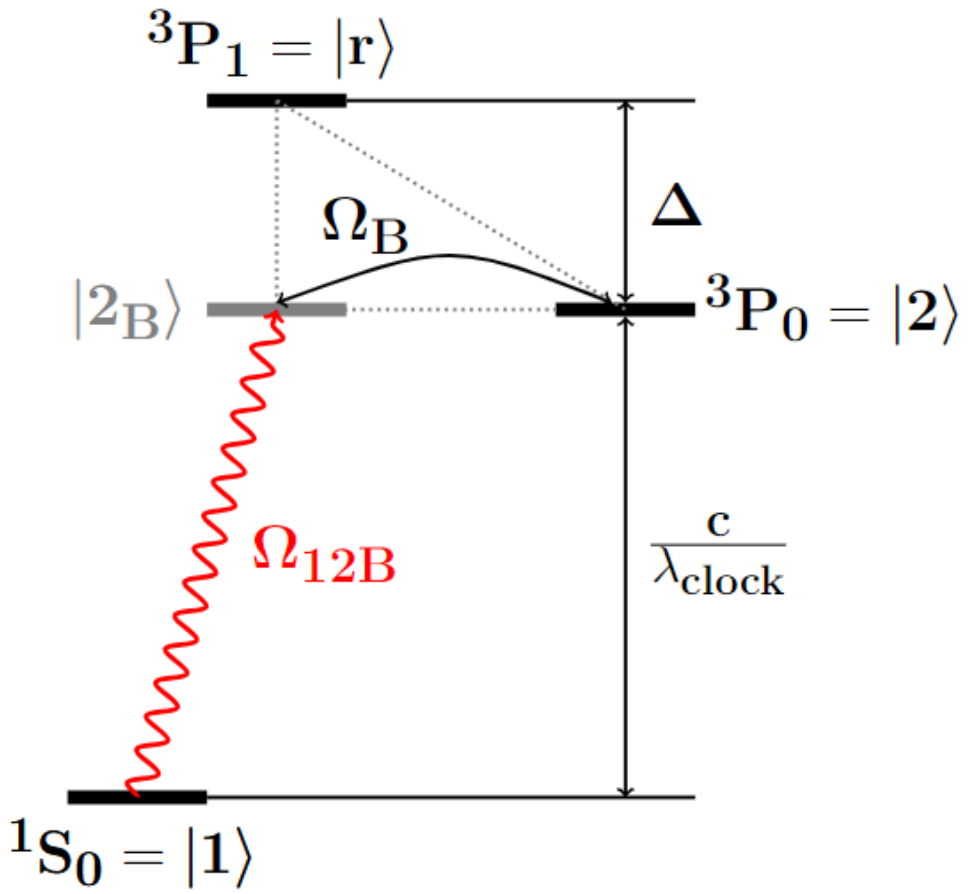


Figure 7: Level structure of $^{88}$Sr where a magnetic coupling generates a dressed state at resonance with the usual clock transition at $\lambda_{\text{clock}}$ = 698 nm. States $|1\rangle$ and $|2\rangle$ are the states of the clock transition, $|r\rangle$ the excited state of the red cooling transition and $|2_B\rangle$ the dressed state outcome of the admixture of $|r\rangle$ into $|2\rangle$. This coupling is at the Rabi frequency $\Omega_B$ and the interferometric laser (in red) couples $|2\rangle$ and the dressed state at the Rabi frequency $\Omega_{12B}$. The scheme can be extended to other alkaline-earth-like atoms by adjusting the values of their respective transitions.

$\lambda$ verifying $\lambda \ll 1$, we can apply the perturbation theory with respect to this quantity.

Let's write $|2_B\rangle$ as

$$|2_B\rangle = c_2 |2\rangle + c_r |r\rangle \tag{41}$$

Only the absolute value of the Rabi frequency is the quantity of interest. Therefore, the propagators of the two states will be neglected as well as the propagator of the coupled state.

Likewise, any component adding a phase to the state will be neglected.

With this choice of $\lambda$, the two contributions to the Hamiltonian are

$$\hat{H}_0 = \hbar \begin{pmatrix} \omega_{21} & 0 \\ 0 & \omega_{r1} - i\Gamma_r/2 \end{pmatrix} \tag{42}$$

and

$$\hat{H}'_1 = \hbar \begin{pmatrix} 0 & \Delta \\ \Delta & 0 \end{pmatrix} \tag{43}$$

with $\omega_{r1}$ and $\omega_{21}$ the frequency difference between states $|1\rangle$ and $|r\rangle$ and the frequency difference between states $|1\rangle$ and $|2\rangle$ respectively.

In the framework of the perturbation theory, the amplitudes of probabilities are

$$c_2(t) = c_2^{(0)}(t) + \lambda c_2^{(1)}(t) \tag{44}$$

and

$$c_r(t) = c_r^{(0)}(t) + \lambda c_r^{(1)}(t) \tag{45}$$

At $t = 0$ the system is in state $|2\rangle$, therefore the zeroth order terms are

$$\begin{cases} c_2^{(0)} = & c_2(0) & = & 1 \\ c_r^{(0)} = & c_r(0) & = & 0 \end{cases} \tag{46}$$

At the first order

$$\begin{cases} i\hbar \frac{d}{dt} c_2^{(1)}(t) & = & \langle 2| \hat{H}'_1 |2\rangle c_2^{(0)} + \langle 2| \hat{H}'_1 |r\rangle e^{i(\omega_{21} - \omega_{r1} + i\Gamma_r/2)t} c_r^{(0)} \\ i\hbar \frac{d}{dt} c_r^{(1)}(t) & = & \langle r| \hat{H}'_1 |2\rangle e^{i(\omega_{r1} - i\Gamma_r/2 - \omega_{21})t} c_2^{(0)} + \langle r| \hat{H}'_1 |r\rangle c_r^{(0)} \end{cases}$$

Given the initial conditions and the elements of $\hat{H}'_1$

$$\begin{cases} \frac{d}{dt} c_2^{(1)}(t) & = & 0 \\ i\hbar \frac{d}{dt} c_r^{(1)}(t) & = & \hbar\Delta e^{i(\Delta - i\Gamma_r/2)t} \end{cases}$$

Integrating the previous system over time and given the conditions of (46), the system becomes

$$\begin{cases} c_2 & = & 1 \\ c_r & = & \frac{\Omega_B}{\Delta}(1 - e^{i\Delta t}) \end{cases}$$

Due to $\left|\frac{i\Gamma_r/2}{\Delta}\right| \ll 1$, the terms $i\Gamma_r/2$ are neglected and we take the time average value of the

the oscillating term $e^{i\Delta t}$ to be zero.

Thus, from (41), $|2_B\rangle$ can be expressed as

$$|2_B\rangle = |2\rangle + \frac{\Omega_B}{\Delta}|r\rangle \tag{47}$$

## Rabi frequency

The Rabi frequency of the coupling between the ground state and the dressed state is

$$\Omega_{12B} = \frac{\langle 1|\,\hat{d}\cdot\mathbf{E}\,|2_B\rangle}{\hbar} \tag{48}$$

Using the expression of the dressed state,

$$\Omega_{12B} = \frac{\Omega_B}{\Delta\hbar}\langle 1|\,\hat{d}\cdot\mathbf{E}\,|r\rangle$$

$$\Omega_{12B} = \frac{\Omega_B\Omega_r}{\Delta} \tag{49}$$

For alkaline-earth-like atoms, $\langle 2|\,\hat{\mu}\,|r\rangle = \sqrt{\frac{2}{3}}\mu_B$, thus

$$\Omega_B = \sqrt{\frac{2}{3}}\frac{\mu_B}{\hbar}B \tag{50}$$

and the Rabi frequency with respect to $|1\rangle$ and $|r\rangle$ can be expressed as any Rabi frequency driving a two-level system with a laser field

$$\Omega_r = \Gamma_r\sqrt{\frac{I}{2I_{sat}}} \tag{51}$$

Thus, the Rabi frequency between the ground state and the dressed can be expressed in the form

$$\Omega_{12B} = \alpha\sqrt{I}B \tag{52}$$

with

$$\alpha = \sqrt{\frac{1}{3I_{sat}}}\frac{\mu_B\Gamma_r}{\Delta\hbar}$$

so approximately $2\pi\times198$ Hz/(T$\sqrt{\mathrm{mWcm}^{-2}}$) for strontium [153]. In the original paper, Taichenachev *et al.* proposed a value for $\alpha$ which for Sr is not correct [138].

### Linewidth

The linewidth of the dressed state with respect to the ground state is the linewidth of the red cooling transition weighted by the portion of admixture of $|r\rangle$ in the dressed state

$$\Gamma_B = \Gamma_r |\langle r|2_B\rangle|^2$$

$$\Gamma_B = \Gamma_r \left|\frac{\Omega_B}{\Delta}\right|^2 \tag{53}$$

For alkaline-earth-like atoms, $\langle 2|\,\hat{\mu}\,|r\rangle = \sqrt{\frac{2}{3}}\mu_B$. Therefore,

$$\Gamma_B = \Gamma_r \frac{2}{3}\left(\frac{\mu_B}{\hbar\Delta}\right)^2 B^2$$

and the magnetic field required to produce a dressed state of linewidth $\Gamma_B$ is

$$B = \sqrt{\frac{3\Gamma_B}{2\Gamma_r}}\frac{\hbar\Delta}{\mu_B} \tag{54}$$

A linewidth comparable to that of the clock transition of $^{87}$Sr is attained using a static magnetic field of $\sim$200 mT.

## III Coherence manipulation via a laser field

We consider a laser field coupling $|2\rangle$ and $|b\rangle$. The results of this section can be found in [155].

In this scheme, the dressed state is the outcome of the admixture of $|b\rangle$ in $|2\rangle$, coupled at the Rabi frequency

$$\Omega_L = \frac{\langle 2|\,M_0\cdot\mathcal{B}_0\,|b\rangle}{\hbar} \tag{55}$$

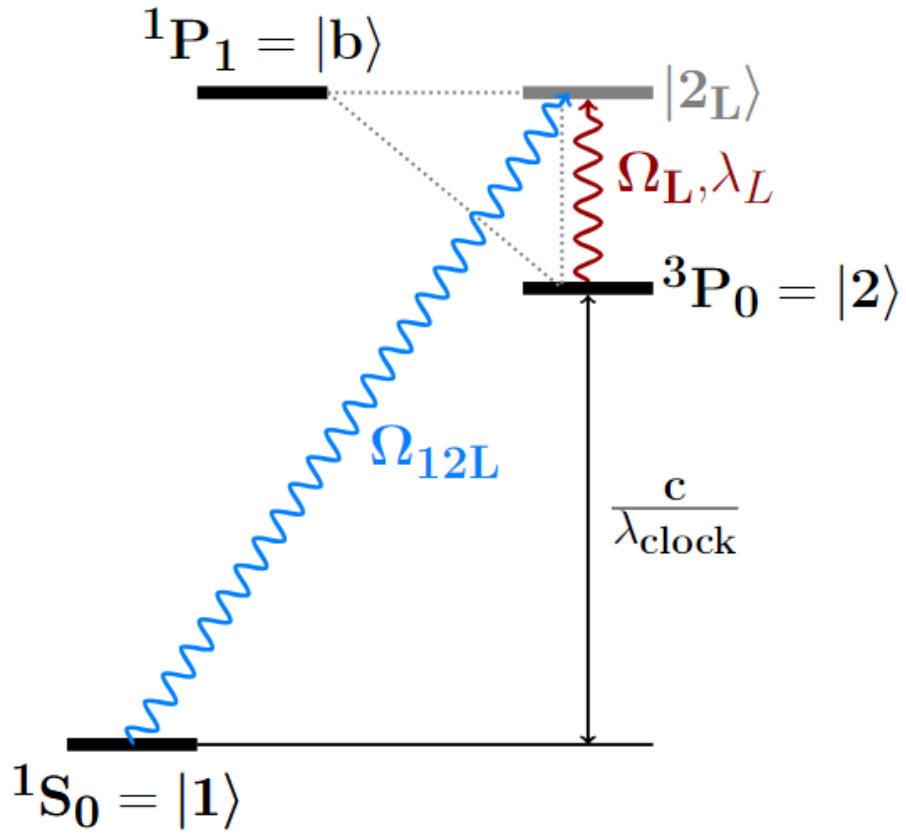


Figure 8: Level structure of $^{88}$Sr where a laser coupling generates a dressed state at resonance with the blue transition at 461 nm. States $|1\rangle$ and $|2\rangle$ are the states of the clock transition, $|b\rangle$ the excited state of the blue cooling transition and $|2_L\rangle$ the dressed state outcome of the admixture of $|b\rangle$ into $|2\rangle$. This coupling at the wavelength 1354 nm is at the Rabi frequency $\Omega_L$ and the interferometric laser (in blue) couples $|2\rangle$ and the dressed state at the Rabi frequency $\Omega_{12B}$. The scheme can be extended to other alkaline-earth-like atoms by adjusting the values of their respective transitions.

For alkaline-earth-like atoms, the matrix element $\langle 2| M_0 \cdot \mathcal{B} |b\rangle$ is approximately $0.022\mu_B$ [80].

Moreover the magnetic component of the dressing field $\mathcal{B}$ can be related to its laser intensity $I_d$

$$I_d = \frac{\mathcal{E}_0^2}{2} = \frac{c^2 \mathcal{B}_0^2}{2} \tag{56}$$

Therefore, the Rabi frequency of the coupling between $|2\rangle$ and $|b\rangle$ can be written

$$\Omega_L = \frac{0.022\sqrt{2}\mu_B}{\hbar c}\sqrt{I_d} \tag{57}$$

## The dressed state

Similarly to the previous section, the dressed state is derived applying the perturbation theory to the system being initially in state $|2\rangle$ under the influence of the laser field at 1354 nm. Then the interaction between states $|1\rangle$ and $|2_L\rangle$ under an electromagnetic field is analysed.

With $I_d$ = 20 W/cm$^2$, $\Omega_L$ is of the order of 4 kHz. As the coupling via the dressing laser is resonant, the energy difference between $|2\rangle$ and $|b\rangle$ is not a relevant quantity to choose the lambda factor. The quantity playing this role is the linewidth of the blue cooling transition $\Gamma_b$ = $2\pi\times$30.5 MHz. The lambda factor of this scheme in the perturbation theory is then

$$\lambda \equiv \frac{\Omega_L}{\Gamma_b} \approx 10^{-5} \tag{58}$$

$\lambda$ verifying $\lambda \ll 1$, we can apply the perturbation theory with respect to this quantity.

the state $|2_L\rangle$ is written

$$|2_L\rangle = c_2\,|2\rangle + c_b\,|b\rangle \tag{59}$$

With this choice of $\lambda$, the two contributions to the Hamiltonian are

$$\hat{H}_0 = \hbar \begin{pmatrix} \omega_{21} & 0 \\ 0 & \omega_{b1} - i\Gamma_b/2 \end{pmatrix} \tag{60}$$

and

$$\hat{H}'_1 = \hbar \begin{pmatrix} 0 & \Gamma_b \cos(\omega_d t) \\ \Gamma_b \cos(\omega_d t) & 0 \end{pmatrix} \tag{61}$$

with $\omega_{b1}$ the frequency difference between states $|1\rangle$ and $|b\rangle$ and $\omega_d$ the frequency of the dressing laser.

In the framework of the perturbation theory, the amplitudes of probabilities are

$$c_2(t) = c_2^{(0)}(t) + \lambda c_2^{(1)}(t) \tag{62}$$

and

$$c_b(t) = c_b^{(0)}(t) + \lambda c_b^{(1)}(t) \tag{63}$$

At $t = 0$ the system is in state $|2\rangle$, therefore the zeroth order terms are

$$\begin{cases} c_2^{(0)} = & c_2(0) & = & 1 \\ c_b^{(0)} = & c_b(0) & = & 0 \end{cases} \tag{64}$$

At the first order

$$\begin{cases} i\hbar \frac{d}{dt} c_2^{(1)}(t) & = & \langle 2| \hat{H}_1' |2\rangle c_2^{(0)} + \langle 2| \hat{H}_1' |b\rangle e^{i(\omega_{21} - \omega_{b1} + i\Gamma_b/2)t} c_b^{(0)} \\ i\hbar \frac{d}{dt} c_b^{(1)}(t) & = & \langle b| \hat{H}_1' |2\rangle e^{i(\omega_{b1} - i\Gamma_b/2 - \omega_{21})t} c_2^{(0)} + \langle b| \hat{H}_1' |b\rangle c_b^{(0)} \end{cases}$$

Given the initial conditions and the elements of $\hat{H}_1'$

$$\begin{cases} \frac{d}{dt} c_2^{(1)}(t) & = & 0 \\ i\hbar \frac{d}{dt} c_b^{(1)}(t) & = & \hbar\Gamma_b \cos(\omega_d t) e^{i(\omega_{b1} - i\Gamma_b/2 - \omega_{21})t} \end{cases}$$

Applying the rotating wave approximation on the component at $-\omega_d - \omega_{b1} + \omega_{21}$ and decomposing the cosine with the Euler formula

$$\begin{cases} \frac{d}{dt} c_2^{(1)}(t) & = & 0 \\ i\hbar \frac{d}{dt} c_b^{(1)}(t) & = & \frac{\hbar\Gamma_b}{2} e^{-i(\delta + i\Gamma_b/2)t} \end{cases}$$

We introduce the detuning of the dressing laser $\delta = \omega_d - (\omega_{b1} - \omega_{21})$. Integrating the previous system over time and given the conditions of (64), the system becomes

$$\begin{cases} c_2^{(1)} & = & 0 \\ c_b^{(1)} & = & \frac{\Gamma_b}{2(\delta + i\Gamma_b/2)} (e^{-i(\delta + i\Gamma_b/2)t} - 1) \end{cases}$$

Neglecting the phase components, the amplitudes of probability are

$$\begin{cases} c_2 & = & 1 \\ c_b & = & \frac{\Omega_L}{2(\delta + i\Gamma_b/2)} (e^{-i(\delta + i\Gamma_b/2)t} - 1) \end{cases}$$

We take the time average value of the oscillating term to be zero and we assume no detuning (or negligible compare to the linewidth of the blue cooling transition)

$$\begin{cases} c_2 &= 1 \\ c_b &= \frac{\Omega_L}{\Gamma_b} \end{cases}$$

Thus, from (59), $|2_L\rangle$ can be expressed as

$$|2_L\rangle = |2\rangle + \frac{\Omega_L}{\Gamma_b}|b\rangle \tag{65}$$

If the detuning is not assumed to be zero, the dressed state takes the form

$$|2_L\rangle = |2\rangle + \frac{\Omega_L}{\sqrt{4\delta^2 + \Gamma_b^2}}|b\rangle \tag{66}$$

## Rabi frequency

The Rabi frequency of the coupling between the ground state and the dressed state is

$$\Omega_{12L} = \frac{\langle 1|\, \hat{d}\cdot\mathbf{E}\,|2_L\rangle}{\hbar} \tag{67}$$

Using the expression of the dressed state,

$$\Omega_{12L} = \frac{\Omega_L}{\Gamma_b\hbar}\langle 1|\, \hat{d}\cdot\mathbf{E}\,|b\rangle$$

$$\Omega_{12L} = \frac{\Omega_L\Omega_b}{\Gamma_b} \tag{68}$$

The Rabi frequency with respect to $|1\rangle$ and $|b\rangle$ can be expressed as any Rabi frequency driving a two-level system with a laser field

$$\Omega_b = \Gamma_b\sqrt{\frac{I_i}{2I_{sat}}} \tag{69}$$

where $I_i$ is the intensity of the interferometric laser.

Thus, using (57)

$$\Omega_{12L} = \beta\sqrt{I_i}\sqrt{I_d} \tag{70}$$

with

$$\beta = \frac{0.022\mu_B}{\hbar c\sqrt{I_{sat}}}$$

so approximately $2\pi\times0.166$ Hz/(mWcm$^{-2}$) for strontium. In this context, $I_{\text{sat}}$ = 425 W/m$^2$ represents the saturation intensity of the blue cooling transition. It should be distinguished from the previous part where it denotes the saturation intensity of the red cooling transition.

## Linewidth

The linewidth of the dressed state with respect to the ground state is the linewidth of the blue cooling transition weighted by the portion of admixture of $|\text{b}\rangle$ in the dressed state

$$\Gamma_L = \Gamma_b |\langle b|2_L\rangle|^2$$

$$\Gamma_L = \frac{\Omega_L^2}{\Gamma_b} \tag{71}$$

Given the expression of $\Omega_L$ in equation (57)

$$\Gamma_L = \left(\frac{0.022\mu_B}{\hbar c}\right)^2 \frac{2I_d}{\Gamma_b}$$

and

$$I_d = \frac{\Gamma_L\Gamma_b}{2}\left(\frac{\hbar c}{0.022\mu_B}\right)^2 \tag{72}$$

A linewidth comparable to that of the clock transition of $^{87}$Sr is attained using a laser intensity of approximately 1.5 W/cm$^2$.

## Other expression

A more precise expression for the dressed state can be found in [155]. If the Feynman propagator are taken into account, the dressed state takes the form

$$\left|\tilde{2}\right\rangle = (|2\rangle\, e^{-i\omega_2 t} + b\,|3\rangle\, e^{-i(\omega_3+\delta_d)t})e^{-i\beta t} \tag{73}$$

with $\beta = \frac{1}{4}\frac{\Omega_d^2}{\delta_d + i\gamma/2}$ and $b = \frac{\Omega_d}{2(\delta_d + i\gamma/2)}$.

The issue in [155] is that the quantity $\gamma_b$ is used instead of $\Gamma_b$. As a result, a factor of $2\pi$ is missing, and the linewidth of the dressed state becomes

$$\Gamma_L = \frac{\Omega_L^2}{\gamma_b} \tag{74}$$

However, even with this corrected formula, [155] still misses a factor of 10, resulting in a dressing laser intensity of 3.9 mW/cm$^2$ instead of the correct value of 39 mW/cm$^2$.

# Scientific production

## Peer reviewed articles

1. C.-H. Feng, S. Vidal, P. Robert, P. Bouyer, B. Desruelle, M. Prevedelli, J. Boullet, G. Santarelli, and A. Bertoldi. High power continuous laser at 461 nm based on a compact and high-efficiency frequency-doubling linear cavity. *Optics Express*, 29(17):27760, August 2021. doi:10.1364/oe.433179. URL https://doi.org/10.1364/oe.433179.

2. Jianing Li, Kelvin Lim, Swarup Das, Thomas Zanon-Willette, Chen-Hao Feng, Paul Robert, Andrea Bertoldi, Philippe Bouyer, Chang Chi Kwong, Shau-Yu Lan, and David Wilkowski. Bi-color atomic beam slower and magnetic field compensation for ultracold gases. *AVS Quantum Science*, 4(4):046801, December 2022. doi:10.1116/5.0126745. URL https://doi.org/10.1116/5.0126745.

## Article submitted

1. C. H. Feng, P. Robert, P. Bouyer, B. Canuel, J. Li, S. Das, C. C. Kwong, D. Wilkowski, M. Prevedelli, and A. Bertoldi. Compact and high flux strontium atom source, 2023. URL https://arxiv.org/abs/2310.00657.

# Bibliography


[1] A. Einstein. Über die von der molekularkinetischen theorie der wärme geforderte bewegung von in ruhenden flüssigkeiten suspendierten teilchen. *Annalen der Physik*, 322(8):549–560, 1905. doi:10.1002/andp.19053220806. URL https://doi.org/10.1002/andp.19053220806.

[2] T. H. MAIMAN. Stimulated optical radiation in ruby. *Nature*, 187(4736):493–494, August 1960. doi:10.1038/187493a0. URL https://doi.org/10.1038/187493a0.

[3] Claude N. Cohen-Tannoudji. Nobel lecture: Manipulating atoms with photons. *Reviews of Modern Physics*, 70(3):707–719, July 1998. doi:10.1103/revmodphys.70.707. URL https://doi.org/10.1103/revmodphys.70.707.

[4] Mark Kasevich and Steven Chu. Atomic interferometry using stimulated raman transitions. *Physical Review Letters*, 67(2):181–184, July 1991. doi:10.1103/physrevlett.67.181. URL https://doi.org/10.1103/physrevlett.67.181.

[5] David W. Keith, Christopher R. Ekstrom, Quentin A. Turchette, and David E. Pritchard. An interferometer for atoms. *Physical Review Letters*, 66(21):2693–2696, May 1991. doi:10.1103/physrevlett.66.2693. URL https://doi.org/10.1103/physrevlett.66.2693.

[6] O. Carnal and J. Mlynek. Young's double-slit experiment with atoms: A simple atom interferometer. *Physical Review Letters*, 66(21):2689–2692, May 1991. doi:10.1103/physrevlett.66.2689. URL https://doi.org/10.1103/physrevlett.66.2689.

[7] M. H. Anderson, J. R. Ensher, M. R. Matthews, C. E. Wieman, and E. A. Cornell. Observation of bose-einstein condensation in a dilute atomic vapor. *Science*, 269(5221):198–201, July 1995. doi:10.1126/science.269.5221.198. URL https://doi.org/10.1126/science.269.5221.198.

[8] K. B. Davis, M. O. Mewes, M. R. Andrews, N. J. van Druten, D. S. Durfee, D. M. Kurn, and W. Ketterle. Bose-einstein condensation in a gas of sodium atoms. *Physical Review Letters*, 75(22):3969–3973, November 1995. doi:10.1103/physrevlett.75.3969. URL https://doi.org/10.1103/physrevlett.75.3969.

[9] L. ESSEN and J. V. L. PARRY. An atomic standard of frequency and time interval: A cæsium resonator. *Nature*, 176(4476):280–282, August 1955. doi:10.1038/176280a0. URL https://doi.org/10.1038/176280a0.

[10] B. Canuel, A. Bertoldi, L. Amand, E. P. Di Borgo, T. Chantrait, C. Danquigny, M. D. Álvarez, B. Fang, A. Freise, R. Geiger, et al. Exploring gravity with the miga large scale atom interferometer. *Scientific Reports*, 8(1):1–23, 2018. doi:10.1038/s41598-018-32165-z.

[11] P. Lebedev. Experimental examination of light pressure. *Nuovo Cimento*, 15(195):195, 1883. URL http://if.pw.edu.pl/~wierzba/zajecia/ed15/lebedev.pdf.

[12] Ernest Fox Nichols and Gordon Ferrie Hull. A preliminary communication on the pressure of heat and light radiation. *Physical Review (Series I)*, 13(5):307, 1901. doi:10.1103/PhysRevSeriesI.13.307.

[13] William D. Phillips and Harold Metcalf. Laser deceleration of an atomic beam. *Physical Review Letters*, 48(9):596–599, March 1982. doi:10.1103/physrevlett.48.596. URL https://doi.org/10.1103/physrevlett.48.596.

[14] S. Chu, L. Hollberg, J. E. Bjorkholm, A. Cable, and A. Ashkin. Three-dimensional viscous confinement and cooling of atoms by resonance radiation pressure. *Physical Review Letters*, 55(1):48, 1985. doi:10.1103/PhysRevLett.55.48.

[15] G. Grynberg, A. Aspect, and C. Fabre. *Introduction to Quantum Optics - From the Semi-classical Approach to Quantized Light*. Cambridge University Press, 2010.

[16] T. Berrada, S. van Frank, R. Bücker, T. Schumm, J.-F. Schaff, and J Schmiedmayer. Integrated mach–zehnder interferometer for bose–einstein condensates. *Nature Communications*, 4(1), June 2013. doi:10.1038/ncomms3077. URL https://doi.org/10.1038/ncomms3077.

[17] M. Kasevich and S. Chu. Measurement of the gravitational acceleration of an atom with a light-pulse atom interferometer. *Applied Physics B Photophysics and Laser Chemistry*, 54(5):321–332, May 1992. doi:10.1007/bf00325375. URL https://doi.org/10.1007/bf00325375.

[18] T. L. Gustavson, P. Bouyer, and M. A. Kasevich. Precision rotation measurements with an atom interferometer gyroscope. *Physical Review Letters*, 78(11):2046–2049, March 1997. doi:10.1103/physrevlett.78.2046. URL https://doi.org/10.1103/physrevlett.78.2046.

[19] C. J. Davisson and L. H. Germer. Reflection of electrons by a crystal of nickel. *Phys. Rev.*, 14:317, April 1928. doi:https://doi.org/10.1073/pnas.14.4.317.

[20] Estermann I. and Stern O. Beugung von molekularstrahlen. *Z. Physik*, 61:95–125, 1930. doi:https://doi.org/10.1007/BF01340293.

[21] S. Templier, P. Cheiney, Q. D'Armagnac De Castanet, B. Gouraud, H. Porte, F. Napolino, P. Bouyer, B. Battelier, and B. Barrett. Tracking the vector acceleration with a hybrid quantum accelerometer triad+. *Science Advances*, 8, 2022. doi:10.1126/sciadv.add3854.

[22] Royal Institution of Great Britain. Notices of the proceedings. *William Clowes and Sons, Limited, Stamford Street and Charing Cross*, 14:355, 1896. URL https://books.google.fr/books?id=ZrloHemOmUEC&pg=PA355&redir_esc=y#v=onepage&q&f=false.

[23] J. B. Fixler, G. T. Foster, J. M. McGuirk, and M. A. Kasevich. Atom interferometer measurement of the newtonian constant of gravity. *Science*, 315(5808):74–77, January 2007. doi:10.1126/science.1135459. URL https://doi.org/10.1126/science.1135459.

[24] G. Lamporesi, A. Bertoldi, L. Cacciapuoti, M. Prevedelli, and G. M. Tino. Determination of the newtonian gravitational constant using atom interferometry. *Physical Review Letters*, 100(5), February 2008. doi:10.1103/physrevlett.100.050801. URL https://doi.org/10.1103/physrevlett.100.050801.

[25] Peter J. Mohr, David B. Newell, and Barry N. Taylor. CODATA recommended values of the fundamental physical constants: 2014. *Reviews of Modern Physics*, 88(3), September 2016. doi:10.1103/revmodphys.88.035009. URL https://doi.org/10.1103/revmodphys.88.035009.

[26] URL https://www.physics.nist.gov/cgi-bin/cuu/Value?bg.

[27] G. Rosi, F. Sorrentino, L. Cacciapuoti, M. Prevedelli, and G. M. Tino. Precision measurement of the newtonian gravitational constant using cold atoms. *Nature*, 510 (7506):518–521, June 2014. doi:10.1038/nature13433. URL https://doi.org/10.1038/nature13433.

[28] L. Morel, Z. Yao, P. Cladé, and S. Guellati-Khélifa. Determination of the fine-structure constant with an accuracy of 81 parts per trillion. *Nature*, 588:61–65, December 2020. doi:https://doi.org/10.1038/s41586-020-2964-7.

[29] Liang Liu, De-Sheng Lü, Wei-Biao Chen, Tang Li, Qiu-Zhi Qu, Bin Wang, Lin Li, Wei Ren, Zuo-Ren Dong, Jian-Bo Zhao, Wen-Bing Xia, Xin Zhao, Jing-Wei Ji, Mei-Feng Ye, Yan-Guang Sun, Yuan-Yuan Yao, Dan Song, Zhao-Gang Liang, Shan-Jiang Hu, Dun-He Yu, Xia Hou, Wei Shi, Hua-Guo Zang, Jing-Feng Xiang, Xiang-Kai Peng, and Yu-Zhu Wang. In-orbit operation of an atomic clock based on laser-cooled 87rb atoms. *Nature Communications*, 9(1), July 2018. doi:10.1038/s41467-018-05219-z. URL https://doi.org/10.1038/s41467-018-05219-z.

[30] URL https://pharao.cnes.fr/en/PHARAO/GP_platform_aces.htm.

[31] Ethan R. Elliott, Markus C. Krutzik, Jason R. Williams, Robert J. Thompson, and David C. Aveline. Nasa's cold atom lab (cal): system development and ground test status. *npj Microgravity*, 4, 2018. doi:https://doi.org/10.1038/s41526-018-0049-9.

[32] T. Lévèque, C. Fallet, J. Lefebve, A. Piquereau, A. Gauguet, B. Battelier, P. Bouyer, N. Gaaloul, M. Lachmann, B. Piest, E. Rasel, J. Müller, C. Schubert, Q. Beaufils, and F. Pereira Dos Santos. Carioqa: Definition of a quantum pathfinder mission, 2022. URL https://arxiv.org/abs/2211.01215.

[33] Pierre Touboul et al. Microscope mission: Final results of the test of the equivalence principle. *PRL*, 129, September 2022. doi:https://doi.org/10.1103/PhysRevLett.129.121102.

[34] URL https://science.nasa.gov/astrophysics/focus-areas/what-is-dark-energy.

[35] G. Bertone, D. Hooper, and J. Silk. Particle dark matter: Evidence, candidates and constraints. *Physics Reports*, 405, 2005. doi:https://doi.org/10.1016/j.physrep.2004.08.031.

[36] N. Aghanim et al. Planck 2018 results: Vi. cosmological parameters. *Journal Astronomy Astrophysics*, 641, September 2020. doi:https://doi.org/10.1051/0004-6361/201833910e.

[37] Y. Abou El-Neaj, C. Alpigiani, S. Amairi-Pyka, H. Araújo, A. Balaž, A. Bassi, L. Bathe-Peters, B. Battelier, A. Belić, E. Bentine, et al. AEDGE: Atomic experiment for dark matter and gravity exploration in space. *EPJ Quantum Technology*, 7(1):1–27, 2020. doi:10.1140/epjqt/s40507-020-0080-0.

[38] M. Coleman Miller and Nicolás Yunes. The new frontier of gravitational waves. *Nature*, 568:469–476, 2019. doi:https://doi.org/10.1038/s41586-019-1129-z.

[39] B.P. Abbott et al. Observation of gravitational waves from a binary black hole merger. *PRL*, 116, February 2016. doi:https://doi.org/10.1038/s41586-019-1129-z.

[40] C. J. Moore, R. H. Cole, and C. P. L. Berry. Gravitational-wave sensitivity curves. *Classical and Quantum Gravity*, 32(1):015014, 2014. doi:10.1088/0264-9381/32/1/015014.

[41] gwplotter: gwplotter.com/.

[42] Don Colladay and V. Alan Kostelecký. Cpt violation and the standard model. *Phys. Rev. D*, 55, June 1997. doi:https://doi.org/10.1103/PhysRevD.55.6760.

[43] A. Peters, K. Y. Chung, and S. Chu. High-precision gravity measurements using atom interferometry. *Metrologia*, 38(1):25, 2001. doi:10.1088/0026-1394/38/1/4.

[44] B. Barrett et al. Testing the universality of free fall using correlated 39k–87rb atom interferometers. *AVS Quantum Sci.*, 4, 2022. doi:https://doi.org/10.1116/5.0076502.

[45] P. Asenbaum, C. Overstreet, M. Kim, J. Curti, and Mark A. Kasevich. Atom-interferometric test of the equivalence principle at the 1012 level. *PRL*, 125, 2020. doi:https://doi.org/10.1103/PhysRevLett.125.191101.

[46] D.O. Sabulsky, I. Dutta, E.A. Hinds, B. Elder, C. Burrage, and Edmund J. Copeland. Experiment to detect dark energy forces using atom interferometry. *PRL*, 123, August 2019. doi:https://doi.org/10.1103/PhysRevLett.123.061102.

[47] David M. Giltner, Roger W. McGowan, and Siu Au Lee. Theoretical and experimental study of the bragg scattering of atoms from a standing light wave. *PRA*, 52, November 1995. doi:https://doi.org/10.1103/PhysRevA.52.3966.

[48] Norman F. Ramsey. A molecular beam resonance method with separated oscillating fields. *Physical Review*, 78(6):695–699, June 1950. doi:10.1103/physrev.78.695. URL https://doi.org/10.1103/physrev.78.695.

[49] Ch. J. Bordé, Ch. Salomon, S. Avrillier, A. van Lerberghe, Ch. Bréant, D. Bassi, and G. Scoles. Optical ramsey fringes with traveling waves. *PRA*, 30, October 1984. doi:https://doi.org/10.1103/PhysRevA.30.1836.

[50] J. Olson et al. Ramsey-bordé matter-wave interferometry for laser frequency stabilization at 10 16 frequency instability and below. *PRL*, 123, 2019. doi:10.1103/PhysRevLett.123.073202.

[51] G. Ferrari, N. Poli, F. Sorrentino, and G. M. Tino. Long-lived bloch oscillations with bosonic sr atoms and application to gravity measurement at the micrometer scale. *Physical Review Letters*, 97(6), August 2006. doi:10.1103/physrevlett.97.060402. URL https://doi.org/10.1103/physrevlett.97.060402.

[52] B. Prasanna Venkatesh and D. H. J. O'Dell. Bloch oscillations of cold atoms in a cavity: Effects of quantum noise. *PRA*, 88, July 2013. doi:https://doi.org/10.1103/PhysRevA.88.013848.

[53] S. Dimopoulos, P. W. Graham, J. M. Hogan, M. A. Kasevich, and S. Rajendran. Atomic gravitational wave interferometric sensor. *Physical Review D*, 78(12):122002, 2008. doi:10.1103/PhysRevD.78.122002.

[54] N. Yu and M. Tinto. Gravitational wave detection with single-laser atom interferometers. *General Relativity and Gravitation*, 43(7):1943–1952, jul 2010. doi:10.1007/s10714-010-1055-8.

[55] P. W. Graham, J. M. Hogan, M. A. Kasevich, and S. Rajendran. New method for gravitational wave detection with atomic sensors. *Physical Review Letters*, 110(17): 171102, apr 2013. doi:10.1103/physrevlett.110.171102.

[56] Andrew D. Ludlow, Martin M. Boyd, E. Peik Jun Ye, and P.O. Schmidt. Optical atomic clocks. *Rev. Mod. Phys*, 87, June 2015. doi:https://doi.org/10.1103/RevModPhys.87.637.

[57] A. V. Davydov. Experimental studies of the gamma resonances of

long-lived nuclear isomers. *Phys. Part. Nuclei*, 43, March 2012. doi:https://doi.org/10.1134/S1063779612020037.

[58] G. D. Cole, W. Zhang, M. J. Martin, Jun Ye, and M. Aspelmeyer. Tenfold reduction of brownian noise in high-reflectivity optical coatings. *Nature Photonics*, 7:644–650, 2013. doi:https://doi.org/10.1038/nphoton.2013.174.

[59] D. G. Matei, T. Legero, S. Häfner, C. Grebing, R. Weyrich, W. Zhang, L. Sonderhouse, J. M. Robinson, J. Ye, F. Riehle, and U. Sterr. 1.5 $\mu$m lasers with sub-10 mhz linewidth. *Physical Review Letters*, 118(26), June 2017. doi:10.1103/physrevlett.118.263202. URL https://doi.org/10.1103/physrevlett.118.263202.

[60] Simon Stellmer, Meng Khoon Tey, Bo Huang, Rudolf Grimm, and Florian Schreck. Bose-einstein condensation of strontium. *Physical Review Letters*, 103(20), November 2009. doi:10.1103/physrevlett.103.200401. URL https://doi.org/10.1103/physrevlett.103.200401.

[61] Simon Stellmer, Rudolf Grimm, and Florian Schreck. Production of quantum-degenerate strontium gases. *Physical Review A*, 87(1), January 2013. doi:10.1103/physreva.87.013611. URL https://doi.org/10.1103/physreva.87.013611.

[62] Y. N. Martinez de Escobar, P. G. Mickelson, M. Yan, B. J. DeSalvo, S. B. Nagel, and T. C. Killian. Bose-einstein condensation of 84sr. *Physical Review Letters*, 103(20), November 2009. doi:10.1103/physrevlett.103.200402. URL https://doi.org/10.1103/physrevlett.103.200402.

[63] Chun-Chia Chen, Rodrigo González Escudero, Jiří Minář, Benjamin Pasquiou, Shayne Bennetts, and Florian Schreck. Continuous bose–einstein condensation. *Nature*, 606 (7915):683–687, June 2022. doi:10.1038/s41586-022-04731-z. URL https://doi.org/10.1038/s41586-022-04731-z.

[64] S. L. Campbell, R. B. Hutson, G. E. Marti, A. Goban, N. Darkwah Oppong, R. L. McNally, L. Sonderhouse, J. M. Robinson, W. Zhang, B. J. Bloom, and J. Ye. A fermi-

degenerate three-dimensional optical lattice clock. *Science*, 358(6359):90–94, October 2017. doi:10.1126/science.aam5538. URL https://doi.org/10.1126/science.aam5538.

[65] A Crawford. On the medicinal properties of the muriated barytes. *Medical Communications, London*, 2:301–359, 1790. URL https://books.google.fr/books?id=bHI_AAAAcAAJ&pg=P301&redir_esc=y#v=onepage&q&f=false.

[66] Thomas Charles Hope. Account of a mineral from strontian, and of a peculiar species of earth which it contains. *Transactions of the Royal Society of Edinburgh*, 4(2): 3–39, 1798. doi:10.1017/s0080456800030726. URL https://doi.org/10.1017/s0080456800030726.

[67] H Davy. Electro-chemical researches, on the decomposition of the earths with observations on the metals obtained from the alkaline earths, and on the amalgam procured from ammonia. *Philosophical Transactions of the Royal Society of London*, 98:333–370, December 1808. doi:10.1098/rstl.1808.0023. URL https://doi.org/10.1098/rstl.1808.0023.

[68] J. Paul MacMillan, Jai Won Park, Rolf Gerstenberg, Heinz Wagner, Karl Köhler, and Peter Wallbrecht. Strontium and strontium compounds, June 2000. URL https://doi.org/10.1002/14356007.a25_321.

[69] A. M. Helmenstine. Chemistry of firework colors – how fireworks are colored, 2012. URL https://www.thoughtco.com/chemistry-of-firework-colors-607341.

[70] T. Douglas Price, Margaret J. Schoeninger, and George J. Armelagos. Bone chemistry and past behavior: an overview. *Journal of Human Evolution*, 14(5):419–447, July 1985. doi:10.1016/s0047-2484(85)80022-1. URL https://doi.org/10.1016/s0047-2484(85)80022-1.

[71] Luville T. Steadman, Finn Brudevold, and Frank A. Smith. Distribution of strontium in teeth from different geographic areas. *The Journal of the American Dental Association*,

57(3):340–344, September 1958. doi:10.14219/jada.archive.1958.0161. URL https://doi.org/10.14219/jada.archive.1958.0161.

[72] Matthew Mike Schweissing and Gisela Grupe. Stable strontium isotopes in human teeth and bone: a key to migration events of the late roman period in bavaria. *Journal of Archaeological Science*, 30(11):1373–1383, November 2003. doi:10.1016/s0305-4403(03)00025-6. URL https://doi.org/10.1016/s0305-4403(03)00025-6.

[73] Larry Benson, Linda Cordell, Kirk Vincent, Howard Taylor, John Stein, G. Lang Farmer, and Kiyoto Futa. Ancient maize from chacoan great houses: Where was it grown? *Proceedings of the National Academy of Sciences*, 100(22):13111–13115, October 2003. doi:10.1073/pnas.2135068100. URL https://doi.org/10.1073/pnas.2135068100.

[74] Rachel Barnett-Johnson, Churchill B Grimes, Chantell F Royer, and Christopher J Donohoe. Identifying the contribution of wild and hatchery chinook salmon (ioncorhynchus tshawytscha/i) to the ocean fishery using otolith microstructure as natural tags. *Canadian Journal of Fisheries and Aquatic Sciences*, 64(12):1683–1692, December 2007. doi:10.1139/f07-129. URL https://doi.org/10.1139/f07-129.

[75] Gary S. Hahn. Strontium is a potent and selective inhibitor of sensory irritation. *Dermatologic Surgery*, 25(9):689–694, September 1999. doi:10.1046/j.1524-4725.1999.99099.x. URL https://doi.org/10.1046/j.1524-4725.1999.99099.x.

[76] J. E. Sansonetti and G. Nave. Wavelengths, transition probabilities, and energy levels for the spectrum of neutral strontium (Sr I). *Journal of Physical and Chemical Reference Data*, 39(3):033103, 2010. doi:10.1063/1.3449176.

[77] NIST. 17. spectral lines: Selection rules, intensities, transition probabilities, values, and line strengths. URL https://www.nist.gov/pml/atomic-spectroscopy-compendium-basic-ideas-notation-data-and-formulas/atomic-spectroscopy.

[78] L. R. Hunter, W. A. Walker, and D. S. Weiss. Observation of an atomic stark–

electric-quadrupole interference. *Physical Review Letters*, 56:823–826, Feb 1986. doi:10.1103/PhysRevLett.56.823.

[79] P H Moriya, M O Araújo, F Todão, M Hemmerling, H Keßler, R F Shiozaki, R Celistrino Teixeira, and Ph W Courteille. Comparison between 403 nm and 497 nm repumping schemes for strontium magneto-optical traps. *Journal of Physics Communications*, 2 (12):125008, December 2018. doi:10.1088/2399-6528/aaf662. URL https://doi.org/10.1088/2399-6528/aaf662.

[80] Robin Santra, Kevin V. Christ, and Chris H. Greene. Properties of metastable alkaline-earth-metal atoms calculated using an accurate effective core potential. *Physical Review A*, 69(4), April 2004. doi:10.1103/physreva.69.042510. URL https://doi.org/10.1103/physreva.69.042510.

[81] S. Loriani, D. Schlippert, C. Schubert, S. Abend, H. Ahlers, W. Ertmer, J. Rudolph, J. M. Hogan, M. A. Kasevich, E. M. Rasel, et al. Atomic source selection in space-borne gravitational wave detection. *New Journal of Physics*, 21(6):063030, 2019. doi:10.1088/1367-2630/ab22d0/meta.

[82] Juan A. Muniz, Dylan J. Young, Julia R. K. Cline, and James K. Thompson. Cavity-qed measurements of the 87sr millihertz optical clock transition and determination of its natural linewidth. *Physical Review Research*, 3(2), May 2021. doi:10.1103/physrevresearch.3.023152. URL https://doi.org/10.1103/physrevresearch.3.023152.

[83] Marcin Bober, Piotr Morzyński, Agata Cygan, Daniel Lisak, Piotr Masłowski, Mateusz Prymaczek, Piotr Wcisło, Piotr Ablewski, Mariusz Piwiński, Szymon Wójtewicz, Katarzyna Bielska, Dobrosława Bartoszek-Bober, Ryszard S Trawiński, Michał Zawada, Roman Ciuryło, Jerzy Zachorowski, Marcin Piotrowski, Wojciech Gawlik, Filip Ozimek, and Czesław Radzewicz. Strontium optical lattice clocks for practical realization of the metre and secondary representation of the second. *Measurement Science and Technology*, 26(7):075201, June 2015. doi:10.1088/0957-0233/26/7/075201. URL https://doi.org/10.1088/0957-0233/26/7/075201.

[84] The National Institute of Standards and Technology (NIST) database. available at http://www.nist.gov/pml/data.

[85] S. Stellmer. *Degenerate quantum gases of strontium*. PhD thesis, University of Innsbruck, 2013.

[86] K. Sengstock, U. Sterr, J. H. Mller, V. Rieger, D. Bettermann, and W. Ertmer. Optical ramsey spectroscopy on laser-trapped and thermal mg atoms. *Applied Physics B Lasers and Optics*, 59(2):99–115, August 1994. doi:10.1007/bf01081160. URL https://doi.org/10.1007/bf01081160.

[87] A. Witte, Th. Kisters, F. Riehle, and J. Helmcke. Laser cooling and deflection of a calcium atomic beam. *Journal of the Optical Society of America B*, 9(7):1030, July 1992. doi:10.1364/josab.9.001030. URL https://doi.org/10.1364/josab.9.001030.

[88] T. Binnewies, G. Wilpers, U. Sterr, F. Riehle, J. Helmcke, T. E. Mehlstäubler, E. M. Rasel, and W. Ertmer. Doppler cooling and trapping on forbidden transitions. *Physical Review Letters*, 87(12), August 2001. doi:10.1103/physrevlett.87.123002. URL https://doi.org/10.1103/physrevlett.87.123002.

[89] H. Hachisu, K. Miyagishi, S. G. Porsev, A. Derevianko, V. D. Ovsiannikov, V. G. Pal'chikov, M. Takamoto, and H. Katori. Trapping of neutral mercury atoms and prospects for optical lattice clocks. *Physical Review Letters*, 100(5), February 2008. doi:10.1103/physrevlett.100.053001. URL https://doi.org/10.1103/physrevlett.100.053001.

[90] M. A. Bouchiat and C. Bouchiat. I. parity violation induced by weak neutral currents in atomic physics. *Journal de Physique*, 35(12):899–927, 1974. doi:10.1051/jphys:019740035012089900. URL https://doi.org/10.1051/jphys:019740035012089900.

[91] Boris Ravaine, M. G. Kozlov, and Andrei Derevianko. Atomic cp-violating polarizability. *Physical Review A*, 72(1), July 2005. doi:10.1103/physreva.72.012101. URL https://doi.org/10.1103/physreva.72.012101.

[92] L. Yi, S. Mejri, J. J. McFerran, Y. Le Coq, and S. Bize. Optical lattice trapping of 199hg and determination of the magic wavelength for the ultraviolet 1s03p0 clock transition. *Physical Review Letters*, 106(7), February 2011. doi:10.1103/physrevlett.106.073005. URL https://doi.org/10.1103/physrevlett.106.073005.

[93] Jonathan N. Tinsley, Satvika Bandarupally, Jussi-Pekka Penttinen, Shamaila Manzoor, Sanna Ranta, Leonardo Salvi, Mircea Guina, and Nicola Poli. Watt-level blue light for precision spectroscopy, laser cooling and trapping of strontium and cadmium atoms. *Optics Express*, 29(16):25462, July 2021. doi:10.1364/oe.429898. URL https://doi.org/10.1364/oe.429898.

[94] Jonathan N. Tinsley, Satvika Bandarupally, Mauro Chiarotti, Shamaila Manzoor, Leonardo Salvi, and Nicola Poli. Prospects for a simultaneous atom interferometer with ultracold cadmium and strontium for fundamental physics tests. In Jacob Scheuer and Selim M. Shahriar, editors, *Optical and Quantum Sensing and Precision Metrology II*, volume 12016, page 1201602. International Society for Optics and Photonics, SPIE, 2022. doi:10.1117/12.2616918. URL https://doi.org/10.1117/12.2616918.

[95] Christian Hofrichter. Probing the su(n) fermi-hubbard model with ytterbium atoms in an optical lattice. 2016.

[96] I. Nosske, L. Couturier, F. Hu, C. Tan, C. Qiao, J. Blume, Y. H. Jiang, P. Chen, and M. Weidemüller. Two-dimensional magneto-optical trap as a source for cold strontium atoms. *Physical Review A*, 96(5):053415, 2017. doi:10.1103/PhysRevA.96.053415.

[97] G. Lamporesi, S. Donadello, S. Serafini, and G. Ferrari. Compact high-flux source of cold sodium atoms. *Review of Scientific Instruments*, 84(6):063102, June 2013. doi:10.1063/1.4808375. URL https://doi.org/10.1063/1.4808375.

[98] P T Greenland, M A Lauder, and D J H Wort. Atomic beam velocity distributions. *J. Phys. D*, 18(7):1223–1232, July 1985. doi:10.1088/0022-3727/18/7/009. URL https://doi.org/10.1088/0022-3727/18/7/009.

[99] Ole Kock, Wei He, Dariusz Świerad, Lyndsie Smith, Joshua Hughes, Kai Bongs, and Yeshpal Singh. Laser controlled atom source for optical clocks. *Sci. Rep.*, 6(1): 37321, November 2016. doi:10.1038/srep37321. URL https://doi.org/10.1038/srep37321.

[100] Chung Chuan Hsu, Rémy Larue, Chang Chi Kwong, and David Wilkowski. Laser-induced thermal source for cold atoms. *Scientific Reports*, 12(1), January 2022. doi:10.1038/s41598-021-04697-4. URL https://doi.org/10.1038/s41598-021-04697-4.

[101] D. Banahene-Sabulsky. *Constraining theories of modified gravity with atom interferometry*. PhD thesis, Imperial College London, 2018.

[102] M. Schioppo. *Development of a Transportable Strontium Optical Clock*. PhD thesis, UNIVERSITÀ DEGLI STUDI DI FIRENZE, 2010.

[103] rp photonics. External-cavity diode lasers. URL https://www.rp-photonics.com/external_cavity_diode_lasers.html.

[104] G. C. Bjorklund, M. D. Levenson, W. Lenth, and C. Ortiz. Frequency modulation (FM) spectroscopy. *Applied Physics B Photophysics and Laser Chemistry*, 32(3):145–152, November 1983. doi:10.1007/bf00688820. URL https://doi.org/10.1007/bf00688820.

[105] Pi200 user guide. available at https://www.koheron.com/support/user-guides/pi200/.

[106] C. L. Tang and H. Statz. Phase-locking of laser oscillators by injected signal. *Journal of Applied Physics*, 38(1):323–324, January 1967. doi:10.1063/1.1708974. URL https://doi.org/10.1063/1.1708974.

[107] L. Winkelmann, O. Puncken, R. Kluzik, C. Veltkamp, P. Kwee, J. Poeld, C. Bogan, B. Willke, M. Frede, J. Neumann, P. Wessels, and D. Kracht. Injection-locked single-frequency laser with an output power of 220 w. *Applied Physics B*, 102(3):529–538,

February 2011. doi:10.1007/s00340-011-4411-9. URL https://doi.org/10.1007/s00340-011-4411-9.

[108] R. D. Niederriter, I. Marques Van Der Put, and P. Hamilton. Polarization purity for active stabilization of diode laser injection lock. *Review of Scientific Instruments*, 92 (8):083004, August 2021. doi:10.1063/5.0059824. URL https://doi.org/10.1063/5.0059824.

[109] C.-H. Feng, S. Vidal, P. Robert, P. Bouyer, B. Desruelle, M. Prevedelli, J. Boullet, G. Santarelli, and A. Bertoldi. High power continuous laser at 461 nm based on a compact and high-efficiency frequency-doubling linear cavity. *Optics Express*, 29(17): 27760, August 2021. doi:10.1364/oe.433179. URL https://doi.org/10.1364/oe.433179.

[110] Bruce G. Klappauf, Yannick Bidel, David Wilkowski, Thierry Chanelière, and Robin Kaiser. Detailed study of an efficient blue laser source by second-harmonic generation in a semimonolithic cavity for the cooling of strontium atoms. *Applied Optics*, 43(12): 2510, April 2004. doi:10.1364/ao.43.002510. URL https://doi.org/10.1364/ao.43.002510.

[111] J.M. Boon-Engering, W.E. van der Veer, E.A.J.M. Bente, and W. Hogervorst. Stabilization of an optical cavity containing a birefringent element. *Optics Communications*, 140(4-6):285–288, August 1997. doi:10.1016/s0030-4018(97)00196-x. URL https://doi.org/10.1016/s0030-4018(97)00196-x.

[112] C. J. Dedman, K. G. H. Baldwin, and M. Colla. Fast switching of magnetic fields in a magneto-optic trap. *Review of Scientific Instruments*, 72(11):4055–4058, November 2001. doi:10.1063/1.1408935. URL https://doi.org/10.1063/1.1408935.

[113] Richard W. Fox, Chris W. Oates, and Leo W. Hollberg. 1. stabilizing diode lasers to high-finesse cavities. In *Cavity-Enhanced Spectroscopies*, pages 1–46. Elsevier, 2003. doi:10.1016/s1079-4042(03)80017-6. URL https://doi.org/10.1016/s1079-4042(03)80017-6.

[114] N.V. Vitanov, B.W. Shore, L. Yatsenko, K. Böhmer, T. Halfmann, T. Rickes, and K. Bergmann. Power broadening revisited: theory and experiment. *Optics Communications*, 199(1-4):117–126, November 2001. doi:10.1016/s0030-4018(01)01495-x. URL https://doi.org/10.1016/s0030-4018(01)01495-x.

[115] J M Farr and W R Hindmarsh. Collision broadening in the strontium resonance line, lambda 4607 AA. *Journal of Physics B: Atomic and Molecular Physics*, 4(4):568–573, April 1971. doi:10.1088/0022-3700/4/4/019. URL https://doi.org/10.1088/0022-3700/4/4/019.

[116] W. Demtröder. *Laser spectroscopy: basic concepts and instrumentation*. Springer Science & Business Media, 2013.

[117] W.T. Silfvast. *Laser Fundamentals*. Cambridge University Press, 1996. ISBN 9780521556170. URL https://books.google.fr/books?id=PcLEQgAACAAJ.

[118] Steven T. Cundiff and Jun Ye. icolloquium/i: Femtosecond optical frequency combs. *Reviews of Modern Physics*, 75(1):325–342, March 2003. doi:10.1103/revmodphys.75.325. URL https://doi.org/10.1103/revmodphys.75.325.

[119] M.J. Thorpe and J. Ye. Cavity-enhanced direct frequency comb spectroscopy. *Applied Physics B*, 91(3-4):397–414, May 2008. doi:10.1007/s00340-008-3019-1. URL https://doi.org/10.1007/s00340-008-3019-1.

[120] Steven T Cundiff. Phase stabilization of ultrashort optical pulses. *Journal of Physics D: Applied Physics*, 35(8):R43–R59, April 2002. doi:10.1088/0022-3727/35/8/201. URL https://doi.org/10.1088/0022-3727/35/8/201.

[121] Anne Amy-Klein, Olivier Lopez, Christian Chardonnet, Émilie Camisard, Giorgio Santarelli, and Paul-Éric Pottie. La lumière des meilleures horloges accessible par les fibres du réseau internet. *Reflets de la physique*, (47-48):91–94, March 2016. doi:10.1051/refdp/20164748091. URL https://doi.org/10.1051/refdp/20164748091.

[122] G. Santarelli, Ph. Laurent, P. Lemonde, A. Clairon, A. G. Mann, S. Chang, A. N. Luiten, and C. Salomon. Quantum projection noise in an atomic fountain: A high stability cesium frequency standard. *Physical Review Letters*, 82(23):4619–4622, June 1999. doi:10.1103/physrevlett.82.4619. URL https://doi.org/10.1103/physrevlett.82.4619.

[123] URL https://courses.physics.ucsd.edu/2016/Spring/physics4e/zeeman.pdf.

[124] URL https://en.wikipedia.org/wiki/Zeeman_effect.

[125] Warren Leywon. Zeeman effect. URL https://commons.wikimedia.org/w/index.php?curid=65502984. available at http://www.nist.gov/pml/data.

[126] Michael A. Joffe, Wolfgang Ketterle, Alex Martin, and David E. Pritchard. Transverse cooling and deflection of an atomic beam inside a zeeman slower. *Journal of the Optical Society of America B*, 10(12):2257, December 1993. doi:10.1364/josab.10.002257. URL https://doi.org/10.1364/josab.10.002257.

[127] T. G. Tiecke, S. D. Gensemer, A. Ludewig, and J. T. M. Walraven. High-flux two-dimensional magneto-optical-trap source for cold lithium atoms. *Physical Review A*, 80 (1), July 2009. doi:10.1103/physreva.80.013409. URL https://doi.org/10.1103/physreva.80.013409.

[128] M. S. Safronova, M. G. Kozlov, and C. W. Clark. Blackbody radiation shifts in optical atomic clocks. *IEEE Transactions on Ultrasonics, Ferroelectrics and Frequency Control*, 59(3):439–447, March 2012. doi:10.1109/tuffc.2012.2213. URL https://doi.org/10.1109/tuffc.2012.2213.

[129] Sergey G. Porsev and Andrei Derevianko. Multipolar theory of blackbody radiation shift of atomic energy levels and its implications for optical lattice clocks. *Physical Review A*, 74(2), August 2006. doi:10.1103/physreva.74.020502. URL https://doi.org/10.1103/physreva.74.020502.

[130] H. J. W. Muller-Kirsten. *Basics of statistical physics*. World Scientific Publishing Company, 2013.

[131] P. G. S. Dias, M. A. F. Biscassi, P. H. N. Magnani, R. F. Shiozaki, Ph. W. Courteille, and R. Celistrino Teixeira. Characterization of the collimation of an atomic beam with a monochromatic quasi-resonant laser. *Brazilian Journal of Physics*, 51(3):329–338, January 2021. doi:10.1007/s13538-020-00837-9. URL https://doi.org/10.1007/s13538-020-00837-9.

[132] Jianing Li, Kelvin Lim, Swarup Das, Thomas Zanon-Willette, Chen-Hao Feng, Paul Robert, Andrea Bertoldi, Philippe Bouyer, Chang Chi Kwong, Shau-Yu Lan, and David Wilkowski. Bi-color atomic beam slower and magnetic field compensation for ultracold gases. *AVS Quantum Science*, 4(4):046801, December 2022. doi:10.1116/5.0126745. URL https://doi.org/10.1116/5.0126745.

[133] D. M. S. Johnson, J. M. Hogan, S. w. Chiow, and M. A. Kasevich. Broadband optical serrodyne frequency shifting. *Optics Letters*, 35(5):745, February 2010. doi:10.1364/ol.35.000745. URL https://doi.org/10.1364/ol.35.000745.

[134] Ralf Kohlhaas, Thomas Vanderbruggen, Simon Bernon, Andrea Bertoldi, Arnaud Landragin, and Philippe Bouyer. Robust laser frequency stabilization by serrodyne modulation. *Optics Letters*, 37(6):1005, March 2012. doi:10.1364/ol.37.001005. URL https://doi.org/10.1364/ol.37.001005.

[135] J. Samland. *Pumping the Zeeman slower*. PhD thesis, University of Amsterdam, 2019.

[136] Alan O. Jamison, Benjamin Plotkin-Swing, and Subhadeep Gupta. Advances in precision contrast interferometry with yb bose-einstein condensates. *Physical Review A*, 90 (6), December 2014. doi:10.1103/physreva.90.063606. URL https://doi.org/10.1103/physreva.90.063606.

[137] Marianna S. Safronova, Sergey G. Porsev, Christian Sanner, and Jun Ye. Two clock transitions in neutral yb for the highest sensitivity to variations of the fine-structure constant. *Physical Review Letters*, 120(17), April 2018. doi:10.1103/physrevlett.120.173001. URL https://doi.org/10.1103/physrevlett.120.173001.

[138] A. Taichenachev, V. Yudin, C. Oates, C. Hoyt, Z. Barber, and L. Hollberg. Magnetic field-induced spectroscopy of forbidden optical transitions with application to lattice-based optical atomic clocks. *Physical Review Letters*, 96(8), March 2006. doi:10.1103/physrevlett.96.083001. URL https://doi.org/10.1103/physrevlett.96.083001.

[139] Z. Barber, C. Hoyt, C. Oates, L. Hollberg, A. Taichenachev, and V. Yudin. Direct excitation of the forbidden clock transition in neutral 174yb atoms confined to an optical lattice. *Physical Review Letters*, 96(8), March 2006. doi:10.1103/physrevlett.96.083002. URL https://doi.org/10.1103/physrevlett.96.083002.

[140] Xavier Baillard, Mathilde Fouché, Rodolphe Le Targat, Philip G. Westergaard, Arnaud Lecallier, Yann Le Coq, Giovanni D. Rovera, Sebastien Bize, and Pierre Lemonde. Accuracy evaluation of an optical lattice clock with bosonic atoms. *Optics Letters*, 32 (13):1812, June 2007. doi:10.1364/ol.32.001812. URL https://doi.org/10.1364/ol.32.001812.

[141] Tomoya Akatsuka, Masao Takamoto, and Hidetoshi Katori. Three-dimensional optical lattice clock with bosonic 88sr atoms. *Physical Review A*, 81(2), February 2010. doi:10.1103/physreva.81.023402. URL https://doi.org/10.1103/physreva.81.023402.

[142] Aaron W. Young, William J. Eckner, William R. Milner, Dhruv Kedar, Matthew A. Norcia, Eric Oelker, Nathan Schine, Jun Ye, and Adam M. Kaufman. Half-minute-scale atomic coherence and high relative stability in a tweezer clock. *Nature*, 588 (7838):408–413, December 2020. doi:10.1038/s41586-020-3009-y. URL https://doi.org/10.1038/s41586-020-3009-y.

[143] Hidetoshi Katori, Masao Takamoto, V. G. Pal'chikov, and V. D. Ovsiannikov. Ultrastable optical clock with neutral atoms in an engineered light shift trap. *Physical Review Letters*, 91(17), October 2003. doi:10.1103/physrevlett.91.173005. URL https://doi.org/10.1103/physrevlett.91.173005.

[144] Karl-Peter Marzlin and Jürgen Audretsch. "freely" falling two-level atom in a running laser wave. *Physical Review A*, 53(2):1004–1013, February 1996. doi:10.1103/physreva.53.1004. URL https://doi.org/10.1103/physreva.53.1004.

[145] A. Bertoldi, F. Minardi, and M. Prevedelli. Phase shift in atom interferometers: Corrections for nonquadratic potentials and finite-duration laser pulses. *Physical Review A*, 99(3), March 2019. doi:10.1103/physreva.99.033619. URL https://doi.org/10.1103/physreva.99.033619.

[146] Cheng Chin, Rudolf Grimm, Paul Julienne, and Eite Tiesinga. Feshbach resonances in ultracold gases. *Reviews of Modern Physics*, 82(2):1225–1286, April 2010. doi:10.1103/revmodphys.82.1225. URL https://doi.org/10.1103/revmodphys.82.1225.

[147] Philipp Haslinger, Matt Jaffe, Victoria Xu, Osip Schwartz, Matthias Sonnleitner, Monika Ritsch-Marte, Helmut Ritsch, and Holger Müller. Attractive force on atoms due to blackbody radiation. *Nature Physics*, 14(3):257–260, December 2017. doi:10.1038/s41567-017-0004-9. URL https://doi.org/10.1038/s41567-017-0004-9.

[148] Simon Bernon, Helge Hattermann, Daniel Bothner, Martin Knufinke, Patrizia Weiss, Florian Jessen, Daniel Cano, Matthias Kemmler, Reinhold Kleiner, Dieter Koelle, and József Fortágh. Manipulation and coherence of ultra-cold atoms on a superconducting atom chip. *Nature Communications*, 4(1), August 2013. doi:10.1038/ncomms3380. URL https://doi.org/10.1038/ncomms3380.

[149] Tetsuya Ido, Yoshitomo Isoya, and Hidetoshi Katori. Optical-dipole trapping of sr atoms at a high phase-space density. *Physical Review A*, 61(6), May 2000. doi:10.1103/physreva.61.061403. URL https://doi.org/10.1103/physreva.61.061403.

[150] N. Poli, R. E. Drullinger, G. Ferrari, J. Léonard, F. Sorrentino, and G. M. Tino. Cooling and trapping of ultracold strontium isotopic mixtures. *Physical Review A*, 71(6), June

2005. doi:10.1103/physreva.71.061403. URL https://doi.org/10.1103/physreva.71.061403.

[151] Y. N. Martinez de Escobar, P. G. Mickelson, P. Pellegrini, S. B. Nagel, A. Traverso, M. Yan, R. Côté, and T. C. Killian. Two-photon photoassociative spectroscopy of ultracold 88sr. *Physical Review A*, 78(6), December 2008. doi:10.1103/physreva.78.062708. URL https://doi.org/10.1103/physreva.78.062708.

[152] A. Stein, H. Knöckel, and E. Tiemann. Fourier-transform spectroscopy of sr2 and revised ground-state potential. *Physical Review A*, 78(4), October 2008. doi:10.1103/physreva.78.042508. URL https://doi.org/10.1103/physreva.78.042508.

[153] Liang Hu, Enlong Wang, Leonardo Salvi, Jonathan N Tinsley, Guglielmo M Tino, and Nicola Poli. Sr atom interferometry with the optical clock transition as a gravimeter and a gravity gradiometer. *Classical and Quantum Gravity*, 37(1):014001, November 2019. doi:10.1088/1361-6382/ab4d18. URL https://doi.org/10.1088/1361-6382/ab4d18.

[154] Liang Hu, Nicola Poli, Leonardo Salvi, and Guglielmo M. Tino. Atom interferometry with the sr optical clock transition. *Physical Review Letters*, 119(26), December 2017. doi:10.1103/physrevlett.119.263601. URL https://doi.org/10.1103/physrevlett.119.263601.

[155] Robin Santra, Ennio Arimondo, Tetsuya Ido, Chris H. Greene, and Jun Ye. High-accuracy optical clock via three-level coherence in neutral bosonic 88sr. *Physical Review Letters*, 94(17), May 2005. doi:10.1103/physrevlett.94.173002. URL https://doi.org/10.1103/physrevlett.94.173002.

[156] Vitaly D. Ovsiannikov, Vitaly G. Pal'chikov, Alexey V. Taichenachev, Valeriy I. Yudin, Hidetoshi Katori, and Masao Takamoto. Magic-wave-induced 1s03p0 transition in even isotopes of alkaline-earth-metal-like atoms. *Physical Review A*, 75(2), February

2007. doi:10.1103/physreva.75.020501. URL https://doi.org/10.1103/physreva.75.020501.

[157] C. Langer, R. Ozeri, J. Jost, J. Chiaverini, B. DeMarco, A. Ben-Kish, R. Blakestad, J. Britton, D. Hume, W. Itano, D. Leibfried, R. Reichle, T. Rosenband, T. Schaetz, P. Schmidt, and D. Wineland. Long-lived qubit memory using atomic ions. *Physical Review Letters*, 95(6), August 2005. doi:10.1103/physrevlett.95.060502. URL https://doi.org/10.1103/physrevlett.95.060502.

[158] D. O. Sabulsky, J. Junca, X. Zou, A. Bertoldi, M. Prevedelli, Q. Beaufils, R. Geiger, A. Landragin, P. Bouyer, and B. Canuel. Multi-photon atom interferometry via cavity-enhanced bragg diffraction, 2022. URL https://arxiv.org/abs/2201.11693.

[159] M. Dovale-Álvarez, D. D. Brown, A. W. Jones, C. M. Mow-Lowry, H. Miao, and A. Freise. Fundamental limitations of cavity-assisted atom interferometry. *Physical Review A*, 96(5), November 2017. doi:10.1103/physreva.96.053820. URL https://doi.org/10.1103/physreva.96.053820.

[160] Sheng wey Chiow, Tim Kovachy, Hui-Chun Chien, and Mark A. Kasevich. 102k large area atom interferometers. *Physical Review Letters*, 107(13), September 2011. doi:10.1103/physrevlett.107.130403. URL https://doi.org/10.1103/physrevlett.107.130403.

[161] Paul Hamilton, Matt Jaffe, Justin M. Brown, Lothar Maisenbacher, Brian Estey, and Holger Müller. Atom interferometry in an optical cavity. *Physical Review Letters*, 114 (10), March 2015. doi:10.1103/physrevlett.114.100405. URL https://doi.org/10.1103/physrevlett.114.100405.

[162] Graham P. Greve, Chengyi Luo, Baochen Wu, and James K. Thompson. Entanglement-enhanced matter-wave interferometry in a high-finesse cavity. *Nature*, 610(7932): 472–477, October 2022. doi:10.1038/s41586-022-05197-9. URL https://doi.org/10.1038/s41586-022-05197-9.

[163] I Riou, N Mielec, G Lefèvre, M Prevedelli, A Landragin, P Bouyer, A Bertoldi, R Geiger, and B Canuel. A marginally stable optical resonator for enhanced atom interferometry. *Journal of Physics B: Atomic, Molecular and Optical Physics*, 50(15):155002, July 2017. doi:10.1088/1361-6455/aa7592. URL https://doi.org/10.1088/1361-6455/aa7592.

[164] Pierre Cladé, Saïda Guellati-Khélifa, François Nez, and François Biraben. Large momentum beam splitter using bloch oscillations. *Physical Review Letters*, 102(24), June 2009. doi:10.1103/physrevlett.102.240402. URL https://doi.org/10.1103/physrevlett.102.240402.

[165] Holger Müller, Sheng wey Chiow, Quan Long, Sven Herrmann, and Steven Chu. Atom interferometry with up to 24-photon-momentum-transfer beam splitters. *Physical Review Letters*, 100(18), May 2008. doi:10.1103/physrevlett.100.180405. URL https://doi.org/10.1103/physrevlett.100.180405.

[166] Sheng wey Chiow, Tim Kovachy, Jason M. Hogan, and Mark A. Kasevich. Generation of 43 w of quasi-continuous 780 nm laser light via high-efficiency, single-pass frequency doubling in periodically poled lithium niobate crystals. *Optics Letters*, 37(18):3861, September 2012. doi:10.1364/ol.37.003861. URL https://doi.org/10.1364/ol.37.003861.

[167] B. Canuel, A. Bertoldi, L. Amand, E. Pozzo di Borgo, T. Chantrait, C. Danquigny, M. Dovale Álvarez, B. Fang, A. Freise, R. Geiger, J. Gillot, S. Henry, J. Hinderer, D. Holleville, J. Junca, G. Lefèvre, M. Merzougui, N. Mielec, T. Monfret, S. Pelisson, M. Prevedelli, S. Reynaud, I. Riou, Y. Rogister, S. Rosat, E. Cormier, A. Landragin, W. Chaibi, S. Gaffet, and P. Bouyer. Exploring gravity with the MIGA large scale atom interferometer. *Scientific Reports*, 8(1), September 2018. doi:10.1038/s41598-018-32165-z. URL https://doi.org/10.1038/s41598-018-32165-z.

[168] Jan Harms, Bram J. J. Slagmolen, Rana X. Adhikari, M. Coleman Miller, Matthew Evans, Yanbei Chen, Holger Müller, and Masaki Ando. Low-frequency terrestrial gravitational-wave detectors. *Physical Review D*, 88(12), December 2013.

doi:10.1103/physrevd.88.122003. URL https://doi.org/10.1103/physrevd.88.122003.

[169] R. Geiger, L. Amand, A. Bertoldi, B. Canuel, W. Chaibi, C. Danquigny, I. Dutta, B. Fang, S. Gaffet, J. Gillot, D. Holleville, A. Landragin, M. Merzougui, I. Riou, D. Savoie, and P. Bouyer. Matter-wave laser interferometric gravitation antenna (miga): New perspectives for fundamental physics and geosciences, 2015. URL https://arxiv.org/abs/1505.07137.

[170] Laura Antoni-Micollier, Daniele Carbone, Vincent Ménoret, Jean Lautier-Gaud, Thomas King, Filippo Greco, Alfio Messina, Danilo Contrafatto, and Bruno Desruelle. Detecting volcano-related underground mass changes with a quantum gravimeter. *Geophysical Research Letters*, 49(13), June 2022. doi:10.1029/2022gl097814. URL https://doi.org/10.1029/2022gl097814.

[171] A. Bertoldi, C.-H. Feng, D. S. Naik, B. Canuel, P. Bouyer, and M. Prevedelli. Fast control of atom-light interaction in a narrow linewidth cavity. *Physical Review Letters*, 127(1), June 2021. doi:10.1103/physrevlett.127.013202. URL https://doi.org/10.1103/physrevlett.127.013202.

[172] Rustin Nourshargh, Samuel Lellouch, Sam Hedges, Mehdi Langlois, Kai Bongs, and Michael Holynski. Circulating pulse cavity enhancement as a method for extreme momentum transfer atom interferometry. *Communications Physics*, 4(1), December 2021. doi:10.1038/s42005-021-00754-6. URL https://doi.org/10.1038/s42005-021-00754-6.

[173] Tao Hong, Claire Cramer, Warren Nagourney, and E. N. Fortson. Optical clocks based on ultranarrow three-photon resonances in alkaline earth atoms. *Physical Review Letters*, 94(5), February 2005. doi:10.1103/physrevlett.94.050801. URL https://doi.org/10.1103/physrevlett.94.050801.

[174] C. H. Feng, P. Robert, P. Bouyer, B. Canuel, J. Li, S. Das, C. C. Kwong, D. Wilkowski, M. Prevedelli, and A. Bertoldi. Compact and high flux strontium atom source, 2023. URL https://arxiv.org/abs/2310.00657.